Impact of the Wisconsinian Glaciation on Canadian Continental Groundwater Flow

by

Jean-Michel Lemieux

A thesis
presented to the University of Waterloo
in fulfillment of the
thesis requirement for the degree of
Doctor of Philosophy
in
Earth Sciences

Waterloo, Ontario, Canada, 2006

I hereby declare that I am the sole author of this thesis. This is a true copy of the thesis, including any required final revisions, as accepted by my examiners.

I understand that my thesis may be made electronically available to the public.

Abstract

During the Quaternary period, cyclic glaciations have occurred over a global scale as the result of a climatic variability that affected the Earth's atmospheric, oceanic and glacial systems. Quaternary glaciations and their associated dramatic climatic conditions, such as kilometers-thick ice sheet formation and permafrost migration, are suspected to have had a large impact on the groundwater flow system over the entire North American continent. Because of the myriad of complex flow-related processes involved during a glaciation period, numerical models have become powerful tools to examine groundwater flow system evolution in this context.

In this study, a series of key processes pertaining to coupled groundwater flow and glaciation modelling, such as density-dependent (*i.e.*, brine) flow, hydromechanical loading, subglacial infiltration, isostasy, sea-level change and permafrost development, are included in the numerical model **HydroGeoSphere** to simulate groundwater flow over the Canadian landscape during the Wisconsinian glaciation ($\sim$ -120 kyr to present). The primary objective is to demonstrate the immense impact caused by glacial advances and retreats during the Wisconsinian glaciation on the dynamical evolution of groundwater flow systems over the Canadian landscape, including surface/subsurface water exchanges (i.e., recharge and discharge fluxes) both in the subglacial and the periglacial environments.

The major findings of this study are that subglacial meltwater infiltration into the subsurface dominates when the ice sheet is growing and, conversely, groundwater exfiltrates during ice sheet regression. This conclusion, which seems to be opposite to the classical hydromechanical loading theory, is a consequence of the interaction between the subglacial boundary conditions and the elastic properties of the rocks. Subglacial infiltration rates during ice sheet progression can reach up to three orders of magnitude higher than the infiltration rate into the periglacial environment and

the current recharge rate into the Canadian Shield.

The impact of the ice sheet on groundwater flow and the brine distribution was dramatic. Hydraulic heads below the ice sheet increase by up to three thousand meters at land surface and up to 1.5 km into the ground. At present time, large over-pressurized zones occur at depth because there has been insufficient time to enable dissipation to their original values. Based on the hydraulic head and solute concentration distribution after the last glacial cycle, it can be shown that the system did not recover to its initial conditions, and that it is still recovering from the last glacial perturbation.

The permafrost has the effect of restraining large areas of the subglacial and periglacial environment from surface/subsurface water interaction; the subglacial permafrost appears along with a cold-based ice sheet, which prevents subglacial meltwater production. The occurrence of a shallow trapped pressure zone below the permafrost after the glacial cycle highlights the critical importance of permafrost on the recovery of the flow system after a glacial cycle.

As a final contribution, the mean groundwater age across the Canadian landscape at the last interglacial (LIG) and throughout the last glacial cycle was computed. Groundwater age is defined as the time elapsed since the water infiltrated in a recharge zone; the mean groundwater age is the mean age of all the particles of water that would be measured in a sample of water. It was found that at LIG, the mean groundwater ages span a large range of values from zero to 42 Myr. Forty-two Myr old groundwater was calculated at depth where there is little groundwater flow and where a mass of stagnant groundwater exists due to high brine concentrations. During the glacial period, old groundwater below the ice sheet mixes with young subglacial meltwater that infiltrates into the ground and the resulting mean groundwater age is younger. The mixing below the ice sheet occurs at great depth, and locations where the mean

groundwater age was older than 1 Myr reaches mean age values between 10 kyr and 100 kyr. At the end of the simulation period, it was found that the mean groundwater age below locations that were affected by the ice sheet advance and retreat is much younger than it was at LIG.

Acknowledgements

A long work always comes with a long list of persons to thank, but because a good work is always one that goes to the essential, I will try to enhance this thesis by keeping the acknowledgments short. First of all, I would like to thank Ed Sudicky who attracted me to Waterloo with a BMW jacket, which I never had, to work on a wonderful project that conjugates all my interest into global climate change, glaciers, groundwater flow and numerical studies. Thanks for taking me to many conferences and supporting me to spend 5 months in Paris. I am also indebted to my co-advisor, Richard Peltier, and to my committee members, Shaun Frape, Jon Sykes and René Therrien who spent their valuable time to share their opinions and suggestions with me. I would also like to thank R.A. Freeze who kindly accepted to act as an external examiner for this thesis.

I would like to thank Ghislain de Marsily who hosted me in the UMR SISYPHE at Uniniversité Pierre et Marie Curie in Paris where I had the opportunity to share knowledge with students and researchers and get a glimpse into the European research community. Field trips in *La vallée de la Durance, Haute Provence* and to the Underground Research Laboratory in Bure were great highlights of my brief visit.

I would like to thank Young-Jin Park and Rob McLaren for their great patience and assistance with numerical problems. Office mates were always there for distraction; it is greatly appreciated. Thanks to my family and friends for their moral support.

Financial aid for the completion of this thesis was provided by the Natural Sciences and Engineering Research Council of Canada (NSERC) and the Ontario Graduate Scholarship (OGS) Program as scholarships to the author and also from NSERC and the Canada Research Chairs program as research funding to E.A. Sudicky. The funding provided by these organisations was critical in the completion of this degree.

Finally, a special thanks to Marie-Claude who accepted to move from Québec City to Waterloo and shared the good and bad moments of this thesis with me.

Contents

List of Tables

List of Figures

Chapter 1

Introduction

"If you can talk brilliantly about a problem,
it can create the consoling illusion that it has been mastered."

Stanley Kubrick

Ice sheets are vast amounts of ice that flowed over the continents over large time scales. During the Quaternary period, cyclic glaciations have occurred over a global scale as the result of a climatic variability that affected the Earth's atmospheric, oceanic and glacial systems. These glaciation periods were characterized by the growth of immense ice sheets covering North America and Europe over a period on the order of $\tilde{1}00$ kyr, followed by fairly rapid deglaciation periods.

It is well documented that severe global-scale environmental perturbations accompanied these glacial periods. For example, during the last glacial maximum (LGM), which occurred between -15 to -23 kyr depending on the source [Peteet, 2006], the Canadian landscape was almost entirely covered with ice. The Laurentide ice sheet, the largest of the three North-American ice-sheet complexes, reached a thickness of about 4.5 km and the force exerted by its weight on the Earth's crust was sufficient to cause a depression of the surface of about 1 km and thus causing a dramatic over-

pressurization of porewater fluids. Extreme atmospheric conditions, accompanying the progression of the ice, caused the freezing of soils and rocks at low latitudes to a depth up to one kilometer into the subsurface. The mean sea level fluctuated by many tens of meters and reached a level of -120 m relative to present at LGM. This was sufficient to completely expose the Bering straight and allowed inhabitants of Eurasia to populate the North-American continent.

Sediments were carried by the glaciers over great distance as they ground the bedrock and eroded the Earth's surface. The sediments were later deposited as different landforms when the ice sheet melted, and some sediments were transported by the meltwater over great distances. Examples of glacial deposits include frontal moraines, which are accumulations of transported sediments of different sizes that mark the maximum advance of the ice sheet. Eskers are produced by subglacial tunnels in which rapidly flowing meltwater was discharging. Large proglacial lakes were formed during ice sheet regression because the Earth's surface below the ice sheet was depressed and required a longer time frame to recover to its original level than the time it took for the ice to melt. For example, the Earth's surface in the Great Lakes region continues to uplift at a rate of approximately a few millimeters per year. Some of the major proglacial lakes such as lake Agassiz were known to be larger than the Great Lakes. The surface drainage network was rapidly evolving, as the proglacial lakes were discharging at different outlets following ice retreat, moraine collapse and surface elevation changes.

Although ice sheets grow during a glaciation period, the friction at the ice-bed interface as well as flow of heat from Earth's interior tends to produce a large amount of subglacial meltwater. This meltwater was, until recently, considered to be drained only as channel and sheet flow at the ice-bed interface, thus being conceptualized as a source of rapid surface-water runoff. Recently, several studies have suggested that

significant subglacial meltwater may infiltrate into the subsurface under the ambient ice sheet pressure and therefore become stored in the groundwater flow system. Because of the small pore spaces within the underlying rocks, a relatively small quantity of recharge into the subsurface can considerably raise pore pressures and therefore modify the groundwater flow field.

Subglacial meltwater is driven into the subsurface at high pressures and mixes with water of different geochemical properties. For example, the subglacial meltwater is fresh and has low total dissolved solids (TDS), but Canadian Shield groundwater has high TDS and a high density that increases with depth. The infiltration of meltwater may have a large impact on the distribution of Shield brines, and the composition of groundwater after the ice retreats is a consequence of mixing. For example, saline springs in the Western Sedimentary Basin are believed to be produced by Pleistocene glacial meltwater that was recharged, which dissolved evaporite units, mixed with deeper basin brines, and now flows out of the basin following the retreat of the ice sheet [Grasby and Chen, 2005]. The understanding of current continental groundwater geochemistry is tied to the understanding of the groundwater history during glacial periods.

Pressurized groundwater below ice sheets may also be an important consideration with regard to issues such as the safe long-term disposal of radioactive wastes [Sheppard *et al.*, 1995b; Talbot, 1999; Heathcote and Michie, 2004]. Because the suitability of deep geologic repositories must be demonstrated over large time scales, flow patterns under an ice sheet must be understood as they may change drastically.

Groundwater also plays a major role in the development of subglacial structures such as sediment deformation and the formation of tunnels and channels. In fact, the ability of subglacial sediments or bedrock to drain meltwater will likely determine the position of tunnels and eskers. It can also play a role in ice sheet dynamics itself,

reducing or raising the effective pressure at the base. Such changes can be reflected by fast- or slow-flowing lobes [Clarke, 2005].

1.1 The Theory of Quaternary Glaciations

It can be stated that the birth of modern glaciation theory dates from July 1837 when Louis Agassiz created a scandal at the *Société Suisse de Sciences Naturelles de Neuchâtel* [Duplessy and Morel, 1990]. In a seminar presented to members of the Society, he suggested that the large erratic blocks of rock spread over the Jura, in Eastern France, were carried over large distances by glaciers in a period during which glaciers would have covered the continental high latitudes. The conclusions of his talk were highly contested and a fierce debate lasted for more than 30 years before the concept of glaciation became accepted, following several years of field work searching for the geological evidence that was eventually found on the northern continents. The concept of large-scale glaciations slowly became accepted, but the field evidence suggested that more than one glaciation occurred and no reliable technique was available to enumerate them precisely. The main reason is because the frontal moraines, that delimit the maximum extent of a glaciation, are erased by subsequent glaciations such that only the last one, or the one that progressed the furthest can be observed. The second reason is because there were no appropriate field techniques to extract sediment cores from the oceans which are believed to record climate variability. It was believed that the oceans would have been much colder during a glaciation period, and thus delineating the cold and warm periods in sediment cores would be a proxy to delineating the timing of the glaciation periods. A coring program was established in 1947 by the Swede Kullenberg who introduced the piston-core sampler that allowed undisturbed cores to be extracted; however, this work did not produce

conclusive results because it neglected other local phenomena affecting the warming and cooling of the ocean other than glacial periods. Another more reliable technique was needed to delineate the glaciation cycles.

Through the work of Harold Urey at the University of Chicago, a Nobel laureate of chemistry in 1934 and the father of isotopic thermodynamics, it was shown that sea water during a glacial period is enriched with the heavy oxygen isotope, ^{18}O, because of preferential evaporation of the lighter isotope, ^{16}O. The ^{16}O is transported as water vapor over large distances and precipitates in the high latitudes over ice sheets, which are subsequently enriched in this light oxygen isotope. In order to estimate the number of glaciations as well as their intensity, one would therefore need to establish a record of the oxygen isotopic composition of the ice and oceans. Cesare Emiliani, a student of Harold Urey at the University of Chicago, recognized that foraminifers, microscopic animals with calcareous shells that form in sea water, should have $^{18}O/^{16}O$ ratios in their shells that are a linear function of the $^{18}O/^{16}O$ ratio of the water in which they lived. This technique was applied to a sediment core extracted from the Caraïbes and one from the equatorial Atlantic Ocean, and results showed that five major glacial periods occurred. These results were highly criticized because the ratio is also known to be a function of temperature in which the foraminifers lived, and thus would also be a proxy for ocean temperature, and not just for sea level change and ice volumes stored on continents. This problem was solved by Nicholas Shackelton, a geochemist at Cambridge University who measured the isotopic ratio in planktonic foraminifers (*i.e.*, those that live in shallow waters and are subject to high temperature variations), and benthic foraminifers that occur in water in which the temperature only varies slightly through time. The signal for both the shallow and the deep foraminifers were found to be the same, thus enabling the conclusion that the variation of the $^{18}O/^{16}O$ ratio was mainly due to glacial ice

volume variations and not temperature. It was shown that about 70% of the variation of the $^{18}O/^{16}O$ ratio was due to ice accumulation on the continents.

Modern analyses of oxygen isotopes in ice cores extracted from ice domes in Greenland and Antarctica, as well as deep sediment cores extracted with the Ocean Drilling Program (ODP) and from old sediments found in the United States now shows that cyclic climatic oscillations have affected the entire continental, oceanic and glacial system for the last 2.6 Ma (Figure 1.1). Of all the glaciations that occurred during this period, the Wisconsinian is the best understood and documented, because it is the most recent one, and the traces left since the last glacial maximum remain on the continent and were not erased by a subsequent glaciation.

Before the glaciation theory was even accepted, scientists were active in establishing theories to explain it and several mechanisms were invoked such as continental drifting, volcanism and orbital insolation variations. The position of continents is a crucial point for the development of continental ice sheets. During the history of Earth, glaciations occurred only when continents were near the poles, and currently, Antarctica is at the south pole and the Eurasian and North American continents are within 1000 km of the North Pole.

In Antarctica, the most important ice advance dates from 35 Ma, when the continent was both on the exact South Pole and circled by the circumpolar cold currents. In the northern hemisphere, the growth of ice is much younger and dates from about 2.6 Ma. The cause for the first Quaternary glaciation is still not well understood but there are two hypotheses that have been postulated and possibly interplayed together. The first is the emergence of Central America that isolated the Pacific Ocean from the Atlantic Ocean. This new configuration would have modified the circulation of the oceanic currents and favored the development of the Gulf Stream. This current carries warm waters and vapor from the equator to the northern latitudes, which

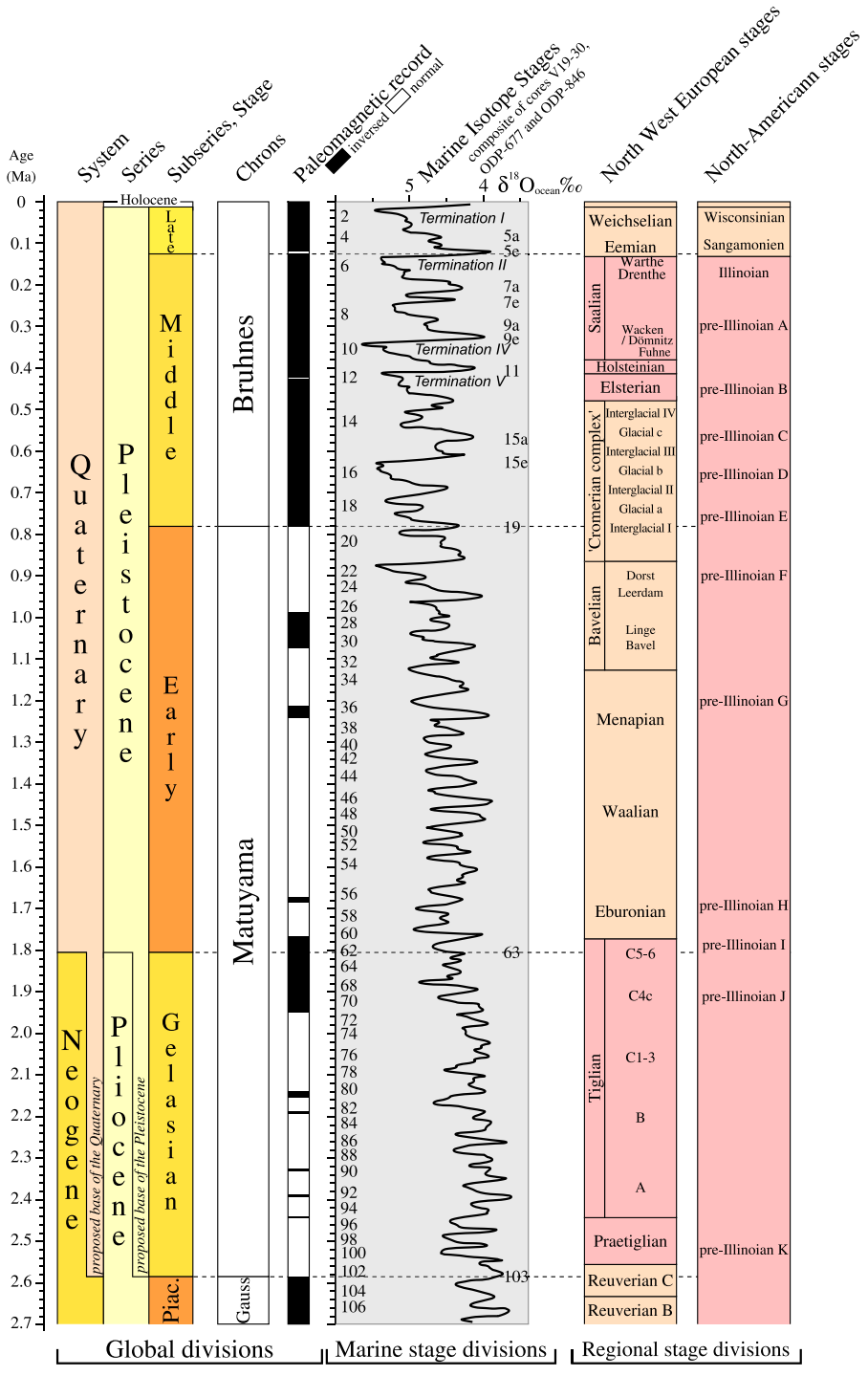

Figure 1.1: Quaternary Stratigraphy. Modified from Gibbard *et al.* [2005].

is necessary in order to generate precipitation and the growth of an ice sheet. The second theory is the uplift of the Tibet and southeastern United States Plateaus that were particularly rapid during the last 10 Ma. Climatic simulations show that this new configuration would perturb atmospheric currents and favor winter conditions and snowstorms in higher latitudes from where ice sheets grow.

The speed of displacement of continental plates is on the order of a few centimeters per year. Thus, except for the two previously-stated exceptions, the configuration of the continents would not have changed much during the last million years. Despite this fact, the climate underwent large oscillations on time frames much too short to be linked to the internal dynamics of the earth. It is therefore necessary to explain this variability by considering the energy budget of the entire Earth, oceanic and atmospheric system, recognizing that the Earth is not intercepting the same fraction of the energy emitted by the sun.

It was a Serbian scientist, Milutin Milankovitch, who suggested in the early 20th century that the climate variability was caused by small variations of solar insolation that occur on Earth due to the changes in the geometry of its orbit around the Sun (Table 1.1). Because of the change in the Earth's orbit around the sun, the equator and the poles would not receive the same amount of energy on the same date each year and this new energy distribution would lead to major climatic changes over long time scales. The theory was tested successfully against field measurements when a spectral analysis performed on the $^{18}O/^{16}O$ ratio measured on sedimentary cores revealed high peaks at frequencies of 19, 23, 41, 100 and 413 ka, which are the same as those predicted by the astronomical theory of Milankovitch [Hays *et al.*, 1976]. It also showed that the Late Pleistocene (0-1 Ma) was dominated by the 100 ka cycle while the Early Pleistocene (1-2 Ma) was dominated by the 41 ka cycle.

We are currently experiencing an interglacial period, and based on the theory of

Table 1.1: Variation cycles of the Earth's orbit around the sun.

Cycle	**Period**	**Description**
Eccentricity	413, 100 ka	The deviation of Earth's orbit from circular to elliptic.
Obliquity	41 ka	The tilt of the Earth's axis of rotation with respect to the perpendicular to the plane of the ecliptic.
Precessional	23, 19 ka	The change of position of solstices and equinoxes at perihelion. Perihelion is the point of the Earth cycle that is nearest to the sun.

Quaternary glaciations, there is no reason to believe that it may not be followed by a glaciation period. The only difference between this interglacial period and the previous is the rapid increase of anthropogenic CO_2 which contributes to global warming through the greenhouse effect. Recent studies tend to predict that the current interglacial will be longer than it would be without human activities [Berger and Loutre, 2004]. This led Paul J. Crutzen, a Nobel laureate of Chemistry in 1995 and his colleague, Eugene F. Stoermer, to propose in 2000 to rename the Holocene to the "Anthropocene" [Crutzen and Stoermer, 2000]!

1.2 Subglacial Processes

During a glacial advance, climatic conditions are very cold in the environs surrounding the ice sheet but, nevertheless, the ice sheet melts. The source of meltwater under an ice sheet is derived from shear heating as well as melting of the base of the ice sheet due to the upward geothermal heat flux [Paterson, 1994]. Boulton *et al.* [1995] hypothesized that the probability that there is meltwater under an ice sheet divide is as low as it is in the extreme marginal zone where permafrost is likely to exist. Hughes [1998], however, recognized that there is a dry-bed zone absent of melting beneath an ice sheet divide although he did not provide a quantitative explanation.

Ice sheets act like blankets and as they progress over the permafrost, the permafrost zone thaws: the permafrost zone is pushed forward in front of the ice sheet as it advances [Hughes, 1998]. The permafrost can, however, extend several kilometers on both sides of ice sheet margin depending on atmospheric conditions.

There are six principal mechanisms to discharge water at the base of glaciers [Boulton *et al.*, 1995, 2001]; 1: flow in a thin layer at the ice/bed interface, 2: flow in subglacial channels (R and N channels), 3: flow through canals, 4: flow through linked cavity systems, 5: flow in tunnel valleys and 6: flow as recharge to groundwater. Flow in a thin layer beneath the ice sheet sole requires that the pressure in the layer equal the ice pressure. Such conditions would lead to an unstable ice flow and unless such evidence is found, this process cannot account for a major draining mechanism. Flow in N-channels [Nye, 1973], such as tunnels carved in the sediments and R-channels [Röthlisberger, 1972], which are carved in the glacier and give birth to eskers, are recognized as major processes controlling subglacial water pressures. Flow through linked cavity systems is due to the accumulation of meltwater in topographic cavities which grow and become linked through a system of stable, interconnecting, topographically-defined conduits [Lliboutry, 1968; Kamb, 1987]. Canals are small conduits that develop in the glacier bed within deforming sediments [Walder and Fowler, 1994]. They are dense, braided, sediment-bearing conduits that often collapse and develop when the subglacial water pressure is close to the ice pressure. Therefore, they will not draw large quantities of water toward them. Tunnel valleys are broad, relatively linear depressions extending upglacier from former ice margins that are eroded into the sediment and weakly indurated sedimentary rock with sizes ranging between 5 to 20 km long, 150 to 500m wide, and 5 to 30m deep [Hooke and Jennings, 2006]. They represent catastrophic releases of meltwater produced by basal melting and stored for decades in subglacial reservoirs at high pressure. Finally, subglacial

recharge and groundwater flow can have a major control over the amount of water available at the ice/bed interface because it represents the quantity of water that the subglacial deposits or basement could not discharge. In this sense, groundwater flow plays a key role in determining the frequency and location of channel flows [Boulton *et al.*, 1995].

1.3 Previous Studies

Because many processes affect the evolution of groundwater flow systems during a glaciation period and these processes are typically strongly coupled, numerical models have become powerful tools to study the impact of glaciation on groundwater flow dynamics over large time frames. In the recent literature, several authors have presented results from numerical modelling studies on the effects of glaciation on groundwater flow. The approaches taken are diverse, but all large-scale studies have ignored important factors known to influence groundwater flow patterns. Moreover, there is a paucity of numerical studies focused on subglacial groundwater flow conducted in North America, and no previous attempts have been made to assess the impact of the last glacial cycle on groundwater flow over the entire Canadian land mass.

In Europe, Boulton conducted a regional 2D steady-state analysis of groundwater flow along a vertical cross section during the Saalian and Weichselian glaciations in Europe that includes the Scandinavian basement and Cenozoic and Mesozoic basins [Boulton *et al.*, 1993, 1995]. As well, he developed a 2D steady-state, vertically-integrated areal model of the European Ice Sheet during the same period [Boulton *et al.*, 1996]. It was found that, in general, meltwater occurring over the Scandinavian Basin could not be drained as groundwater and that subglacial channels formed. On the other hand, it was suggested that all meltwater can be drained by the sedimentary

aquifers [Boulton *et al.*, 1996].

A second European initiative was undertaken by Piotrowski in Northwestern Germany during the Weichselian glacial maximum. A 2D steady-state cross-sectional model of about 30 km in length was used to estimate the quantity of water drained as groundwater in a Tertiary Basin [Piotrowski, 1997a]. Piotrowski [1997b] extended his steady-state model to 3D in order to include the spatial structure of the aquifers. The main conclusion was that subglacial aquifers can drain about 25% of the total meltwater. This conclusion contradicts Boulton's conclusion that all meltwater can be drained by subglacial aquifers. Piotrowski [1997b] explains this difference by the level of detail he used to represent the geologic media. He also suggested that the meltwater excess would discharge in tunnel valleys. This conclusion is supported by the presence of several tunnel valleys observed in this region.

Another study was carried out by van Weert *et al.* [1997] to examine the effect of Pleistocene glaciations on the geohydrological system of northwestern Europe. Using constraints from the Boulton and Payne [1993] ice sheet simulation, they constructed an areal, vertically-integrated model of Northwestern Europe and performed steady-state simulations at different time slices in order to calculate hydraulic head distributions and infiltration rates into subglacial aquifers. Their conclusion was that subglacial meltwater can be completely or partially drained by the underlying aquifers and that the location of tunnels and channels is closely related to excess meltwater locations. They also concluded that groundwater velocities under the ice sheet are relatively large and that the direction of flow is very different under glacial loading conditions.

The only complex and realistic transient study was carried out by Provost *et al.* [1998] in the Fennoscandian Shield. Flow along a 1500-km-long cross section that extended to a depth of about 10-km in southern Sweden was simulated over a 140 ka

period with a variable-density groundwater flow model. It was found that recharging meltwater can reach depths of a few kilometers in a few thousand years and that the meltwater may reside in the subsurface for periods exceeding 10 ka.

In North America, Breemer *et al.* [2002] present results along a 2D steady-state cross section that elucidates the subglacial hydrology of the Lake Michigan Lobe of the Laurentide ice sheet. Their main objective was to investigate the capacity of the subglacial formations to drain glacial meltwater because the lobe was known to be fast-flowing. They concluded that about one third of produced meltwater was drained into the underlying aquifers.

Another North American initiative was undertaken by Chan *et al.* [2005] and Chan and Stanchell [2005] in which the impact of the last glaciation over the Whiteshell Research Area in Manitoba was addressed. The site covers a region of 25.4 km $\times$ 37.3 km $\times$ 4 km in the Canadian Shield. Chan *et al.* [2005] presented results in the context of the Benchmark Test 3 (BMT3) of the international DECOVALEX[1] III project, which has been designed to provide an illustrative example that explores the mechanical and hydraulic response of a fractured crystalline rock mass to a period of glaciation. This study was conducted to investigate the sensitivity of simulation results to several factors, including steady-state versus transient boundary conditions, coupled hydromechanical versus uncoupled analyses and model dimensionality (two-dimensional versus three-dimensional). Chan and Stanchell [2005] extend this study to explore how transient events associated with long-term climate change and a glacial cycle may influence the evolution of a deep-seated crystalline groundwater flow system. The main conclusions from these studies are; 1: transient coupled modelling is necessary to capture the essence of glacial effects on groundwater flow system evolution, 2: fracture-zone network geometry, interconnectivity and hydraulic properties

[1]Acronym for DEvelopment of COupled (THM) models and their VALidation against EXperiments in nuclear waste isolation.

significantly influence the magnitude and rate of flow domain response, and 3: model dimensionality can significantly affect simulation results.

Several studies in North America concerning subglacial flow were conducted using environmental isotopes. In short, the isotopic composition of the water is used to distinguish between groundwater of different origins. Environmental isotopes ^{18}O and ^{2}H as well as total dissolved solids (TDS) are the primary parameters used. Glacial meltwater is characterized by low $\delta^{18}O$, $\delta^{2}H$ and TDS. Clark *et al.* [2000] and Douglas *et al.* [2000] showed that meltwater from the Laurentide ice sheet could have penetrated down to a depth of 1600 m in the Mirimar Con Mine in Yellowstone, a Canadian Shield environment. Grasby *et al.* [2000] studied, using stable isotopes and other physical evidence, the regional flow system of the Williston Basin in southwestern Manitoba for its petroleum-migration pathway implications. They showed that a significant influx of fresh water into the basin occurred during the Pleistocene glaciations and that it caused the reversal of the current flow system. They concluded that assuming the modern day distribution of subsurface pressures may not be a good proxy for ancient petroleum migration pathways. Other studies using groundwater composition that show evidence of glacial meltwater recharge were conducted in the Canadian Shield [Raven *et al.*, 1987], in the North Central United States [Siegel and Mandle, 1983; Siegel, 1989, 1991; McIntosh *et al.*, 2002; McIntosh and Walter, 2005], Western Ontario [Weaver *et al.*, 1995] and in the Western Canada sedimentary Basin [Grasby *et al.*, 2000; Grasby and Chen, 2005].

Although the previous numerical studies provided insights into subglacial processes, one of their main weaknesses is that almost all of them were performed as a series of steady-state time slices. A glaciation is a highly transient event and groundwater pressure evolves slowly. Subsurface pressure distributions are likely to be significantly influenced by historical conditions because of the long time needed

for water to flow in low-permeability rocks, especially at depth.

None of the numerical studies considered fully-transient 3D groundwater flow at a continental scale with brine-derived density effects during a full glacial cycle and very few of them focused on the Laurentide Ice Sheet in Canada. The present work is therefore considered to be highly original and is intended to address important questions concerning 3D transient groundwater flow during a glacial cycle, as well as highlight specific characteristics related to the subglacial history of North America.

1.4 Objectives

The main objective of the study is to understand groundwater flow during a glacial cycle using a numerical model, with a specific focus on the Canadian landscape. In this context, there are three main issues that are not yet well understood and would thus benefit from this research.

The first point concerns the evolution of water pressures underneath the ice sheet. The subglacial melting as well as the ice sheet load will cause a rise in groundwater pressures. The quantification of the pressure evolution in 3D and its relation to permafrost development is a key point to address as it pertains to, for example, the topic of the long-term performance of a spent nuclear-fuel repository.

The second point concerns the rate of infiltration (*i.e.*, groundwater recharge) occurring beneath ice sheets. The infiltration amount, and the timing of subglacial meltwater recharge events as well as the mechanisms that control its spatial patterns, regulates the excess meltwater that can runoff and, therefore, affect the development of subglacial sedimentary structures.

The third important point concerns the flow directions and travel times of subglacial meltwater that entered the subsurface. There are several lines of evidence

from environmental isotope studies indicating that meltwater circulated deep in the subsurface. Understanding subglacial infiltration rates, spatial variability issues and subsurface travel paths could help shed light on the present-day distribution of isotopes and other constituents in groundwater. This understanding of the impacts of past glaciations on Canadian continental-scale groundwater flow will also be critical to the prediction of future-climate change on Canada's groundwater and surface-water resources.

1.5 Thesis Organization

Chapter 2 starts with a brief review of Canadian continental hydrogeology and groundwater geochemistry. The specific aspects of modelling at large spatial and temporal scales will be addressed as well as the hydraulic and climatic conditions existing during a glacial cycle. Chapter 3 deals with the description of the numerical model and new processes included in the model to address the problem at hand. Several examples are also presented in order to verify the numerical implementation. In Chapter 4, the linkage of the groundwater flow model to a model of the Wisconsinian glaciation is presented, along with a description of its boundary and initial conditions. In Chapter 5, calculations of the surface/subsurface water interactions for a base-case scenario are presented. In Chapter 6, the impact of the last glacial period on Canadian continental groundwater flow and brine distributions is examined in detail. The modelling process, the reliability of the model and the results are thoroughly discussed. In Chapter 7, groundwater age theory is presented and applied to the glacial-cycle simulation in order to delineate the evolution of the mean age distribution across the country. Finally, Chapter 8 provides the salient conclusions of this work along with a discussion of the model limitations.

Chapter 2

Continental Hydrogeology

"Les choses sont ce qu'elles sont parce qu'elles étaient ce qu'elles étaient..."

Hubert Reeves, *Patience dans l'azur*

Groundwater flow modelling at large scale calls for prudent simplifications because not all geologic heterogeneities and process details affecting flow over and within the Canadian landscape can be included in the model. Commonly occurring geological materials that exhibit relatively consistent hydrogeological properties over the continent can, nevertheless, be found to enable the simplifications while still allowing the capture of large-scale flow system trends. The large time periods involved in this study also brings the need to take into account a wide range of climatic conditions that are usually not included in hydrogeological studies such as permafrost development, isostasy and ice loading. In this chapter, a review of Canadian continental hydrogeology is performed, focusing on the different geological provinces as hydrogeological units. An overview of the unconsolidated deposits and their relevance at large temporal and spatial scales is also presented. Climatic conditions that prevail at present time and the changes that occur throughout a glacial cycle are discussed, as well as the modelling tools used to generate this set of forcing boundary conditions.

Finally, a discussion of the subsurface hydraulic conditions believed to exist during a glacial cycle will be presented as well as an overview of the current knowledge on the subject.

2.1 Bedrock hydrogeology

The geological architecture of Canada is dominated by the Precambrian Canadian Shield which forms the backbone of the continent (Figure 2.1). The Shield consists of several Archean fragments composed of granitic rocks and gneiss along with volcanic greenstone belts and broader tracts of sedimentary rocks [Wheeler *et al.*, 1997]. The Shield also contains younger orogenic belts between the Archean fragments made of continental, oceanic, and collisional deposits and foreign or exotic fragments.

Few detailed hydrogeological studies have been performed in the Canadian Shield, and much fewer at depth, mainly because the region is sparsely populated and because the surface waters are of good quality [Farvolden *et al.*, 1988; Rouleau *et al.*, 2003]. Most of the detailed studies are related to the geological storage of radioactive nuclear wastes deep within crystalline rocks. These studies were mainly conducted in the Chalk River and Atikokan areas in Ontario and at the underground research laboratory (URL) near Pinawa, Manitoba. The studies conducted at these sites indicate that the rock is fractured extensively at scales ranging from meters to tens of meters or more in terms of fracture spacings and there exist zones which can be broadly categorized as sparsely fractured, moderately fractured and highly fractured rock [e.g. Raven, 1986; Stevenson *et al.*, 1996, among others]. In general, the degree of fracturing decreases with depth from the surface. The virgin rock mass is saturated at depth [Raven and Gale, 1986] with the water table being commonly within a few meters of the surface in the Shield. If the fracture zones are connected in a net-

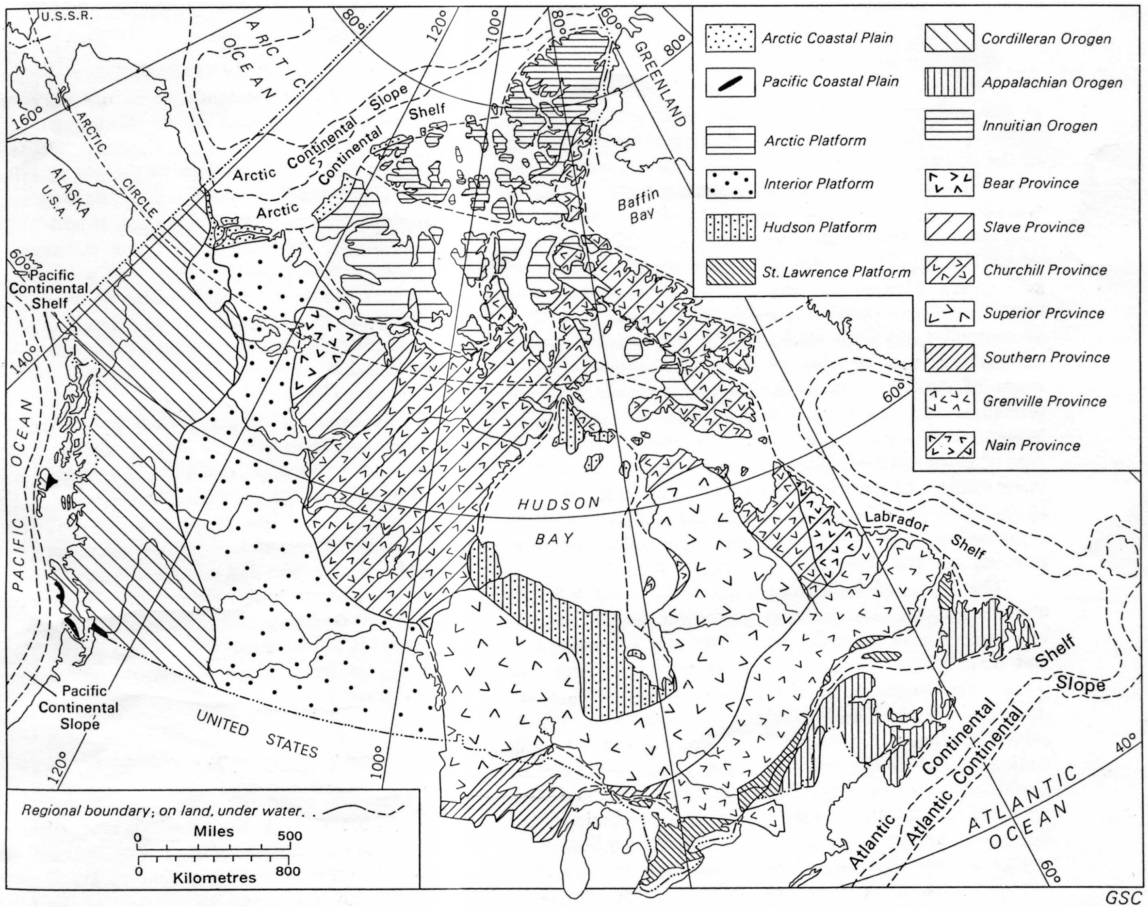

Figure 2.1: Geology of Canada. The Canadian Shield is made of the Bear, Slave, Churchill, Superior, Grenville and Nain provinces. Source: Douglas [1971]

work, then this connectivity will allow groundwater circulation even though the rock matrix has very low permeability. Due to the magmatic and metamorphic history of the rocks, the primary porosity is very low as well as its hydraulic conductivity. Hydraulic conductivity is usually much higher in the upper few tens to hundreds of meters and significantly diminishes with depth, although there is no single relationship between depth and permeability. Farvolden *et al.* [1988] point out that a log-linear decrease can usually be observed in the first 400 m and that the deeper hydraulic conductivity values tend to be variable depending on the fractures or faults intercepted. At great depths, the permeability decreases dramatically and Neuzil

[1995] suggests that minimal permeability should exist at depths greater than about 7 km. The permeability reduction with depth is due to increasing effective stresses and temperature-dependent diagenetic and metamorphic processes [Ingebritsen and Sanford, 1998].

Table 2.1 is a compilation of the hydraulic properties measured in the Canadian Shield and reported in the literature. Most of the values reported were derived from studies related to nuclear-waste disposal. The objective of these studies was to examine the suitability of rocks of low permeability to isolate radionuclides for a sufficiently long time so as to not pose a threat for human health should a release occur from an engineered repository located at depth. Therefore, plutons and batholiths (intrusive bodies) which are less fractured than the other rocks of the Shield were primarily investigated. The values presented in Table 2.1 are thus biased by low hydraulic conductivity values. Mine-site data, which have a long legacy of hydraulic testing, are generally not accessible because of confidentiality reasons. One of the few compilations of mine-related hydraulic measurements found in the literature is from Raven and Gale [1986]. Results presented in Table 2.1 are divided into shallow (< 500 m) and deep (> 500 m) measurements, and for each depth category, values are reported for the matrix, the fractures or the bulk rock mass depending on the nature of the measurements. The matrix measurements reported here are not necessarily representative of the intact rock matrix itself because the matrix can include small pervasive fractures. Nevertheless, it can be seen from Table 2.1 that deeper measurement locations typically exhibit a lower hydraulic conductivity. It is also clear that specific storage measurements are lacking in most published reports.

Stober and Bucher [2005] present the results of a one-year-duration pumping test in a pilot hole of the deep research drillhole (KTB) in the crystalline basement of central Germany in which 23,100 m^3 of saline water was extracted. The results are

Table 2.1: Compilation of hydraulic properties reported in the literature for the Canadian Shield.

Depth	**Medium**	K m/yr	S_s m^{-1}	ϕ -	**Reference**
Shallow (< 500 m)	Matrix	10^{-5}–10^{0}			3,4
	Fracture	10^{-3}–10^{3}	1×10^{-5}	0.001-0.042	2,3,4
	Bulk	10^{-1}–10^{2}		0.027	1,5,6,7,8
Deep (> 500 m)	Matrix	10^{-6}–10^{-4}			4
	Fracture	10^{0}–10^{4}			4
	Bulk	10^{-2}			1

References: 1. Raven *et al.* [1987], 2. Raven [1986], 3. Farvolden *et al.* [1988], 4. Stevenson *et al.* [1996], 5. Frost and Everitt [1997], 6. Kuchling *et al.* [2000], 7. Raven and Gale [1986], 8. Frost [1997],

quite unexpected because the experiment indicated that the pore space of the upper crust is highly fractured and connected and, therefore, the continental upper crust can be considered as an aquifer. The interpretation of the pumping test data yielded a hydraulic conductivity of 4.1×10^{-8} m/s with a storage coefficient (storativity) of about 5×10^{-6} (specific storage, $S_s = 3.3\times10^{-8}$ m^{-1}). The average flowing porosity of the fractured rock was determined to be 0.6-0.7%. Stober and Bucher [2005] concluded that this range can be taken as representative and characteristic of the continental upper crust in general. A simplified cross-section is shown in Figure 2.2 in which the continental crust is divided into an upper brittle permeable crust and a lower ductile aquiclude separated by a transition zone. The upper part of the crust is a saturated and permeable rock mass due to a connected fracture pore space [Stober and Bucher, 2004]. This hydrogeological conceptualization of the upper crust probably holds for the Canadian Shield, at least over the upper 10 km which is the depth range considered in the present study. This is also the depth range over which direct measurements of permeability in the crust have been conducted [Huenges *et al.*,

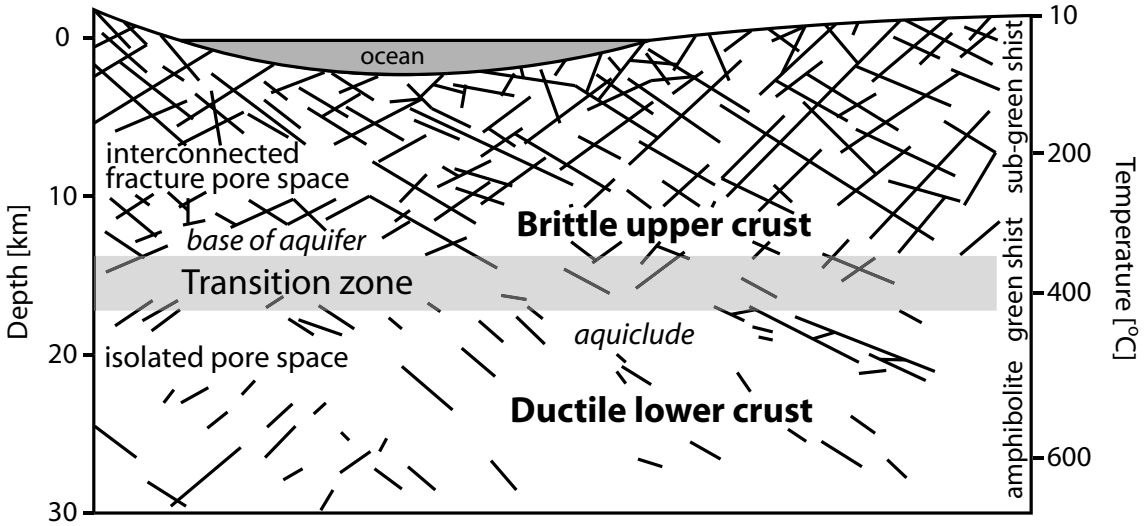

Figure 2.2: Schematic cross section trough the continental crust. Brittle upper crust with an interconnected pore space (aquifer) and lower ductile crust with isolated fractures (aquiclude) are shown. Modified from Stober and Bucher [2004].

1997].

There are three younger deformed orogenic belts across Canada, mainly consisting of Phanerozoic rocks surrounding the Shield (Figure 2.1). The oldest orogenic belt is the Appalachian Belt to the southeast of the Canadian Shield which is comprised of oceanic and continental fragments that date from early- to mid-Paleozoic. The Western Canadian Cordillera is also an accumulation of continental and oceanic fragments that formed during the Mesozoic. The physiography of these orogenic belts is related to their age of formation. The Cordillera is much younger and has a high relief, with Mount Logan reaching an elevation of 5959 m, while the Appalachians are much older with a much more rounded relief. The highest point of the Appalachians is at an elevation of 1917 m at the summit of Mount Washington, NH. The rocks of the Appalachians are mainly comprised of dense igneous and metamorphic rocks, with some sedimentary rocks, while in the younger Rockies, the sedimentary rocks form a large part of the mountains. The remaining mountain belt is the Innuitian

Belt which extends from Ellesmere Island to Melville Island. It is a Siluro-Devonian belt that consists of highly deformed sedimentary, metamorphic and volcanic rocks.

The formation of the mountains was accompanied by volcanic eruptions and metamorphism. The rocks in these belts have also undergone folding, faulting and uplift. The permeability distribution is therefore highly variable. The most dominant feature for groundwater flow is the fractures and faults that formed along with the mountains [*e.g.*, Randall *et al.*, 1988, for the Appalachians] as well as the deformed lithology [*e.g.*, Foxworthy *et al.*, 1988, for the Cordillera]. Water flows mainly through the fractures under gravity drainage from the high elevations to the lower valleys.

The hydraulic properties of the shallow rocks of the Appalachians were compiled by Randall *et al.* [1988]. Hydraulic conductivity values for porous and non-porous bedrock varies between 1.1 $\times 10^{-6}$ m/s [$\approx$ 35 m/yr] to 1.65$\times 10^{-5}$ m/s [$\approx$ 520 m/yr]. Specific storage values are typically near 2×10^{-2} m^{-1}. These data originate from tests conducted in industrial and municipal wells, which put a bias in the data because only the shallow-regime high hydraulic conductivity values are measured in such studies. Much lower permeable rocks, not likely to be explored in such studies, were not tested; thus the values presented above represent the upper range in values.

Large parts of the Canadian Shield are covered by the Interior, Arctic, Hudson and St-Lawrence Platforms and are thin layers of undeformed sedimentary rocks, except for the Western Canada Basin (Interior Platform) east of the Cordillera. These are mainly of early Paleozoic age (Figure 2.1) and rest unconformably over the Canadian Shield. The St-Lawrence Platform is a Cambro-Ordovician sequence of continental to deep marine sediments, starting with sandstones at the bottom, followed upward by a carbonate platform and overlain by thick shale deposits. The beds are sub-horizontal with large-amplitude gentle folds [Globensky, 1987]. Large faults are common across the platforms and they contain a network of extensive small-scale and bed-contained

fractures. Extensive hydraulic testing of the sandstone, dolostone and carbonate rocks near Montréal is reported by Nastev *et al.* [2004]. Hydraulic conductivity values vary from 10^{-8} m/s [$\approx$ 0.3 m/yr] to 10^{-3} m/s [$\approx 3 \times 10^4$ m/yr] with an overall geometric mean of 2.6×10^{-5} m/s [$\approx$ 820 m/yr]. A weak decreasing trend of the transmissivity with depth was observed to a depth of 100 m.

The Interior Platform, also referred to as the Interior Plains or Western Sedimentary Basin, lies between the Cordillera and the Canadian Shield (Figure 2.1). The Western Sedimentary Basin is a westward-thickening wedge of Mesozoic and Cenozoic sediments. The sediments that form the basin are a succession of sandstones, shales and carbonates. The basin thickens westward and can reach a depth of about 6100 m at the thrust front. The basin was uplifted during the Cordilleran Orogeny and the surface is now dipping east with higher elevations occurring at its west end to a much lower elevation in Manitoba, where it ends. The conceptual model of groundwater flow through the basin is that meteoric infiltration on the elevated western segment sustains the basin such that recharge balances groundwater discharge and the water table is a subdued configuration of the surface topography [Garven, 1989]. Groundwater recharge is occurring along the western elevated portion of the basin and descends to great depth where it acquires salinity and heat along the flow path. The water flows regionally along the laterally extensive aquifers and discharge near the eastern edge of the basin where the saline and hot water cools, ascending and mixing with shallow circulating groundwater [Garven, 1989]. Garven and Freeze [1984a,b] also point out that maximum flow rates of about 1 to 10 m yr^{-1} developed in the deep aquifers while much lower flow rates occur in the aquitards.

Garven [1989] provides hydraulic conductivity values for the main units comprising the Western Sedimentary Basin. Horizontal hydraulic conductivity values range from 0.001 to 200 m/yr and vertical values range between 1×10^{-5} and 20 m/yr. Specific

storage coefficients range from 1×10^{-3} to $\times10^{-5}$ m^{-1} and porosity between 0.05 and 0.3 depending on the units. The lower values correspond to a small Devonian evaporite deposit, such that average values are likely much higher.

The Hudson Platform lies in the middle of Hudson Bay (Figure 2.1) and is composed of Paleozoic strata that are near flat-lying to gently dipping. The rocks are represented by a variety of shallow marine facies composed of sandstone, shale, limestone, dolomite and evaporite, which are succeeded by non-marine sediments [Stockwell *et al.*, 1971]. The depth of the sequence can reach up to 2 km in the centre of Hudson Bay. The hydrogeology of this platform is largely unknown because it is mostly submersed by Hudson Bay and therefore unexplored. The types of rocks are believed to be similar to those of the St-Lawrence Platform and therefore identical hydraulic properties will be applied in the model developed here.

The final platform is the Arctic Lowlands which consists of early Paleozoic, flat-lying sedimentary rocks. This platform represents the northern continuation of the Interior Plains of the continental mainland [Thorsteinsson and Tozer, 1971]. There is little hydrogeological information available for this basin and because its origin is similar to that of the Western Sedimentary Basin, the same hydraulic properties will be used.

Finally, the oceanic crust, that extends around the periphery of the North American continent, is of basaltic composition. Because of the difficulties related to hydraulic testing in this environment, there are few studies that address the permeability within the basaltic oceanic crust. Oceanic crust permeability is intimately linked to crustal formation due to vertical layering, depending on the intrusive or effusive origin of the magma, and with lateral variations from the ridge to the continent's margin [Fisher, 1998]. The shallowest oceanic basement is believed to be more permeable due to pillow formation and brecciation. Vertical faults are likely to be the major

conduits between the permeable surface and the deeper basalts, but these vertical faults can close due to mineral precipitation as the rocks move away from the ridge. Fisher [1998] reports a summary of bulk permeability measurements performed using packers as part of the Deep Sea Drilling Project and the Ocean Drilling Program. The estimated permeability values range from 10^{-13} to 10^{-18} m^2 ($\approx 10^{-4}$ to 10^{1} m/yr) with an average of about 10^{-15} m^2 ($\approx 10^{-1}$ m/yr). The measurements are highly variable depending on the measurement technique used and the packer vertical lengths over which the measurements were performed. Larger interval measurements tend to include large-scale features such as fracture zones, faults, or other heterogeneities and these measurements tends to be more homogeneous, while small-scale measurements tend to reflect small-scale features such as individual fractures and are thus much more variable.

There are several forces that are known to cause large-scale fluid migration which include topography-driven flow, free-convection flow cells driven by buoyancy forces associated with temperature and salinity, compaction, tectonic dilation/compression, chemical diagenesis, hydrocarbon generation, etc [Garven, 1995]; however, as Garven [1995] points out, the dominant mechanism for groundwater flow in continental masses, both shallow and deep systems, is the topographic relief [Tóth, 1962, 1963; Freeze and Witherspoon, 1967]. It should be noted, however, that these studies did not include the presence of brines at depth which are believed to strongly influence deep-seated flow systems. The different flow mechanisms described above evolve gradually through time. For example, the Western Sedimentary Basin, in the Late Phanerozoic, was a compaction-driven basin with free convection. During the Late-Cretaceous-Tertiary time, after the Rocky Mountains formed, a large flow system developed from west to east and resulted in the Pb-Zn ore district of Pine Point and the Athabasca tar sands deposits. At present day, Garven [1995] claims that the cur-

rent flow system can be interpreted from potentiometric maps as a topographically driven-flow system even if some abnormal pressures are measured locally. Those abnormal pressures are seen as rapid erosional unloading or as the result of Pleistocene glaciations.

Because the Rocky Mountains are the youngest geological province of the country and because groundwater flow, except for some minor abnormal pressures, have been interpreted as a topographically driven flow system, it is believed that most of the present-day groundwater flow system over the Canadian landscape would be driven by topography and buoyancy forces associated with brines. Garven [1995] provides a list of major continental systems across the world that show chemical evidence of topographically driven flow with residence times of up to 2 Ma. These systems include the central Missouri, discharging waters from the Colorado Front Ranges, the Great Artesian Basin of Australia, the Nubian sandstone of northern Africa, Egypt, the Los Llanos Basin of Columbia and the Paraná Basin, Brazil.

In Chapter 4, the areal and depth distribution of the various rock types and the hydrogeological properties assigned to them will be discussed further. Again, the reader should keep in mind that a high-resolution bedrock description of Canada in unavailable, at least to depths of several kilometers, and that the developed groundwater model can only be expected to capture large-scale trends in flow system evolution.

2.2 Hydrogeology of Unconsolidated Deposits

Overlying the bedrock across Canada exists a sedimentary drift that was deposited when the ice sheet retreated. The thickness of the sediments is highly variable from one region to the other, and its distribution is usually well correlated to the type of source rock lying nearby. A thin till veneer typically covers portions of the Canadian

Shield because of the hardness of the igneous rocks. Thicker sequences can be found over sedimentary basins where the exposed rocks are much more subject to increased glacial abrasion. In the Western Sedimentary Basin, drift thicknesses of up to 50 m are common and thicknesses of more than 300 m can be found locally. In the St-Lawrence Lowlands, the thicknesses of Quaternary deposits can reach values up to 150 m in the vicinity of Montreal [Ross *et al.*, 2005] and thicknesses up to 300 m can be found in the Michigan Basin. Because of their often high permeability values, the unconsolidated sediments represent the most exploited sources of freshwater for human and industrial needs.

During a glacial advance, a significant portion of the unconsolidated sediments are ground by the ice and can be transported over large distances. Along with new material arising from the abrasion of the substratum, these materials are re-deposited during the melting of the ice sheet to form a sequence of unconsolidated sediments as we observe today in the glaciated parts of the continent.

Overall, the unconsolidated sediments are very thin compared to the 10-km thickness of the domain and the thicker unconsolidated sequences found across Canada are commonly composed of clayey materials that have a low hydraulic conductivity not too different from the basement rocks. Because of this, the hydraulic properties of the unconsolidated sediments are not distinguished from the consolidated sedimentary rocks.

2.3 Groundwater Geochemistry

The study of the geochemical properties of groundwater in a continental context is a complex task and several theses could likely be devoted to this aspect alone. Therefore, only a few basic geochemical issues will be addressed in this study. Mainly,

the total dissolved solids (TDS) concentration and its impact on the fluid physical properties will be addressed, as well as its known areal and depth distribution based on published data.

The main geochemical feature of the Canadian Shield groundwaters is the occurrence of brines of a relatively uniform composition over the Shield [Frape and Fritz, 1987]. The major ions composing the brines are Ca-Na-Cl and their compositional load increases with depth (Figure 2.3). Because the brine composition is more-or-less uniform across the Shield, the linear density relationship with TDS appears to be quite consistent across the sampling sites. The linear relationship that relates the density of the fluid, ρ, to its concentration in TDS, c (in grams per litre), is as follows: $\rho = 7.35 \times 10^{-4} c + 1$ [Frape and Fritz, 1987]. There are two main groups of waters existing in the crystalline rocks of the Canadian Shield: shallow groundwater which reflects local climatic regimes and a second group which are the brines which exhibit a similar isotopic signature at all sites. A mixture of both members is also common. Although the brines and saline waters are usually observed at depth, there is some evidence that indicate they are discharging at the land surface at some locations [Gascoyne and Sheppard, 1993; Sheppard *et al.*, 1995a]. The origin of the most concentrated brines located at depth is still in debate. One school of thinking is that the brines were derived from Paleozoic seawater while the other claims that the high salinity is the result of leaching of fluid inclusions or chemical reactions occuring with rock minerals.

In the Western Sedimentary Basin, highly saline brine is believed to originate from the evaporation of sea water during the accumulation of Paleozoic sediments in the basin [Spencer, 1987]. The brine is located at depth in the Devonian formation and is shifted up-dip to the east and north as the result of long-term basin-scale flow. The brine discharging as springs and diffuse zones at the northern and eastern margins of

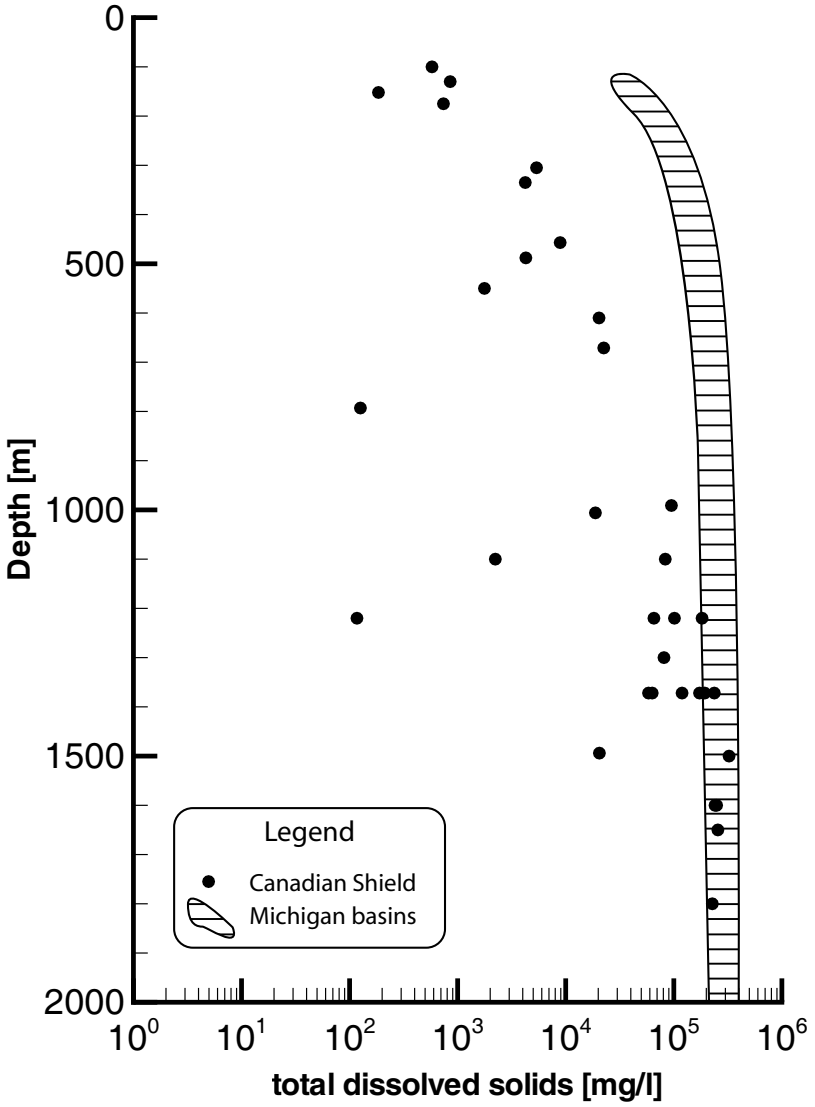

Figure 2.3: The relationship of depth and total dissolved solids for groundwater from the Canadian Shield and the Michigan, Illinois and Appalachian Basins. The latest three basins are grouped together under the name Michigan Basin. Source: Frape and Fritz [1987] for Canadian Shield data and McIntosh and Walter [2005] for the Michigan Basin data.

the basin are less saline compared to an expectation resulting from long-term basin-scale flow towards this belt. Grasby and Chen [2005] argue that these brines are not the result of long-term basin-scale flow, but rather because of Pleistocene glacial meltwater that was driven downward, dissolved evaporite units, mixed with deeper basin brines, and now discharges out of the basin following the retreat of the ice sheet. This later flow system should be younger than the previous one and therefore cannot solely be used to interpret the present-day hydrodynamics of the basin because of the paleo-hydrogeology of the system.

Brine occurrence is also well-documented in the Michigan Basin and in Southern Ontario [Dollar *et al.*, 1991] as well as in the St-Lawrence Lowlands where deep brines are extracted for commercial purposes. Information is scarce regarding the groundwater chemistry of the orogenic belts. For the Appalachians, most of the bedrock is insoluble and the concentration of dissolved solids, even for deep wells, is low and rarely exceed 1,000 mg/L [Randall *et al.*, 1988].

2.4 Climatic Evolution

The inferred climatic conditions during the Wisconsinian glaciation presented here are derived from the University of Toronto Glacial Systems Model (GSM), which is an ice-sheet coupled energy-balance model recently described by Tarasov and Peltier [1999] and Tarasov and Peltier [2004]. The GSM is composed of six components linked together and representing, respectively, surface mass balance, thermomechanically-coupled ice-sheet dynamics, basal dynamics, ice calving, isostasy, and climate forcing. In this model, the atmosphere and ocean are described using an energy balance model, in which neither the atmosphere nor ocean dynamics are directly captured. Instead, a detailed distribution of the continents and oceans along with their respective heat

capacity (low for continents, high for oceans) is used. The surface temperature is then computed using the balance between incoming short wave solar radiation and outgoing long wave radiation, redistributed towards the poles from the equator in order to mimic atmosphere dynamics. The carbon dioxide level is also specified in the atmosphere as it blocks part of the outgoing long wave radiations from the Earth's surface and contributes to the temperature warming through the greenhouse effect.

The temperatures computed with the energy-balance model as well as the present-day observed distribution of precipitation over the North-American continent are used to derive a precipitation field during the glacial cycle. Along with a map of vertical heat flow from the Earth's interior, the precipitation distribution and temperature fields are used to compute accumulation or ablation of ice on the Earth's surface. The ice accumulated on the surface is free to flow and its movement is solved using a three-dimensional thermomechanical ice-sheet model. There is also a basal dynamics component to the model that allows till deformation when the temperature below the ice-sheet is above the pressure melting point.

The last component of the GSM is the isostatic adjustment process. As the ice sheet grows over the surface, its weight causes the Earth's crust to depress due to mantle viscosity. For an ice load of 4 km, Peltier [2002] points out that the depression can reach as much as 1 km. This will have an important impact on ice-sheet dynamics as well as temperature distributions.

The GSM was executed over the past 120 kyr on a 1.0° longitude by 0.5° latitude grid resolution in order to produce a dataset for surface elevation, ice sheet thickness, relative sea-level and subglacial melting rate. Additional components to this model were recently implemented. Among these, Tarasov and Peltier [2005a] solve the surface drainage chronology using a fast and simple routing algorithm. This produces a solution for the lake water-depths across the ice-free surface. Another

recently added component is the permafrost thickness evolution which is computed from a one-dimensional heat-flow model coupled with the ice-sheet model [Tarasov and Peltier, 2005b].

As discussed earlier, permafrost forms in ice-sheet free regions where the surface temperature remains perennially cold. As the ice sheet covers the ground, it acts like a blanket, protecting the subsurface from severe atmospheric temperatures, and the geothermal gradient as well as frictional heating at the base of the flowing glacier ice warms the ground and thaws it. This can be observed in Fig 2.4a for LGM where most of the permafrost below the ice sheet has melted and the permafrost extends beyond the ice sheet margin. During the last interglacial, no ice sheet was present and the climate resembled the present climate with an extensive permafrost zone existing in the northern latitudes (Fig 2.4.b).

Although the term "permafrost" is commonly used in the context of frozen soils and rocks, there are different types of permafrost and each will have a different impact on groundwater flow. Continuous permafrost is usually referred to as a material in which all of the water within the soil is permanently frozen. Discontinuous permafrost represents a large body of permafrost that contains some unfrozen sections. Sporadic permafrost is found in isolated, small patches of permanently frozen ground, and intermittent permafrost refers to soil/rock freezing conditions that can change from year to year. The permeability of soils affected by permafrost is greatly reduced [Burt and Williams, 1976] but there is no consensus on the permeability reduction due to a paucity of data [Boulton and de Marsily, 1997]. The main effect of extensive permafrost is that it prevents surface water from recharging groundwater and conversely from allowing groundwater to discharge to the surficial regime [McEwen and de Marsily, 1991]. In regions of discontinuous and sporadic permafrost, surface water and groundwater can interact through the unfrozen sections. Structures such as

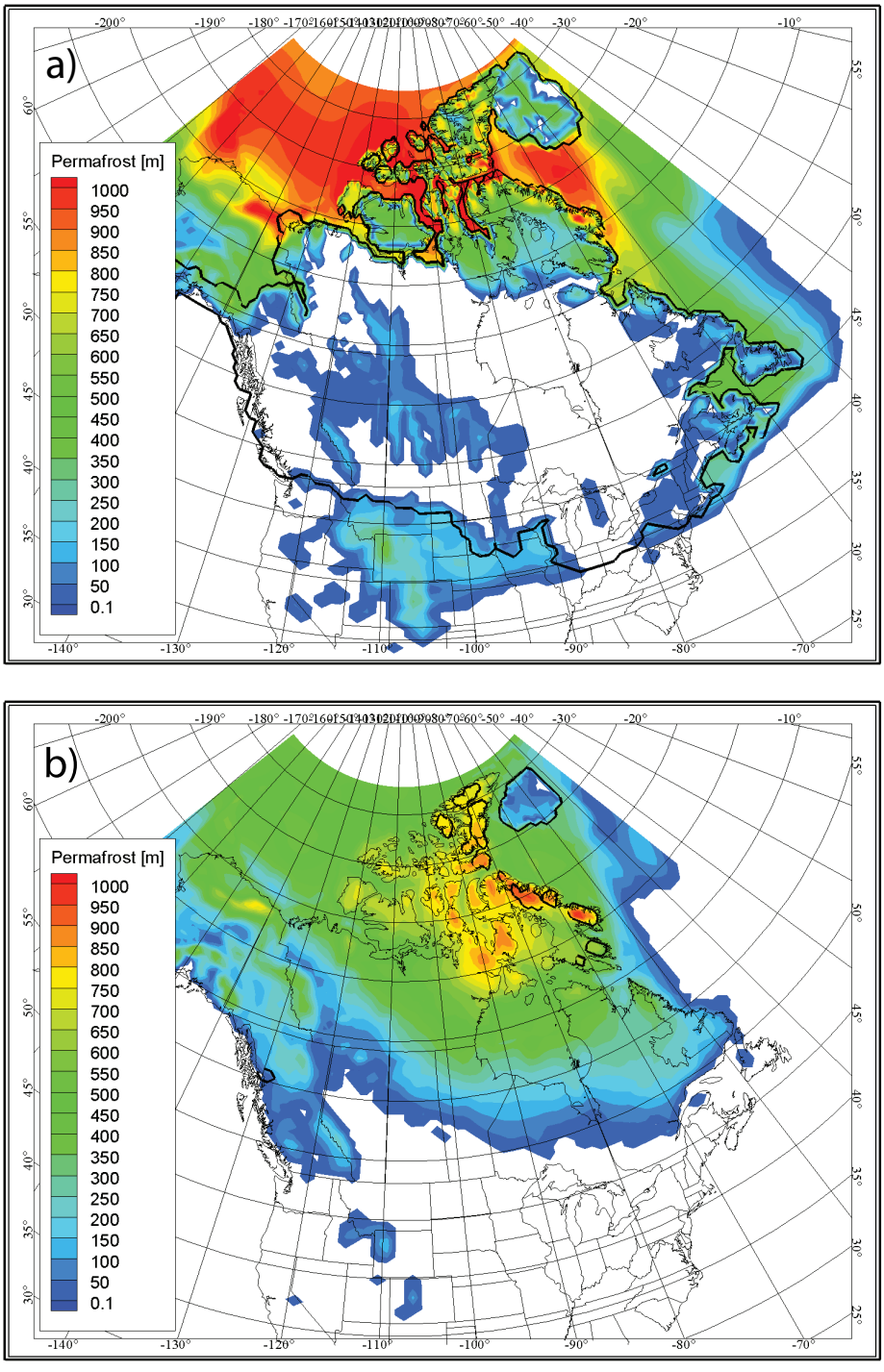

Figure 2.4: a) Permafrost thickness at LGM and b) Last interglacial. Solid black line indicates the limit of ice. Source: Tarasov and Peltier [2005b].

taliks, which are "holes" of unfrozen ground, have been observed below large surface water bodies even in regions where the permafrost is quite deep in the surroundings. These taliks can allow recharge or discharge of deep groundwater [McEwen and de Marsily, 1991]. Figure 2.5 shows the current permafrost distribution across Canada as well as permafrost thicknesses. Clearly, the impact of permafrost zones will have a large effect on regional groundwater flow patterns, and therefore must be included in a continental-scale groundwater flow model intended to capture the effects of the advance and retreat of ice sheets over the last glacial cycle.

During their formation, ice sheets store large amounts of water on the continent and the sea level falls while the opposite happens during ice sheet disintegration. The term eustasy is generally used to refer to the rise and fall of sea level. Figure 2.6 shows the eustatic sea level relative to present during the last 120 kyr along with the continental ice volume. These curves provide an indication of the cyclic ice sheet progression and retreat over the continent, knowing that the last glacial maximum was reached at -21 kyr. Figure 2.6 also shows that there are three glacial maxima occurring at about -110 kyr, -60 kyr and -21 kyr, each followed by ice regressions. Once again, it is clear that such dramatic changes in sea level must be incorporated into the continental-margin boundary conditions of a continental-scale groundwater flow model.

Subglacial meltwater is derived from shear-heat melting as well as melting of the glacier sole due to the upward geothermal heat flux [Paterson, 1994]. Figure 2.7 shows the subglacial melting rate at LGM. Meltrates in terms of water fluxes usually do not exceed a few centimeters per year except locally, near the southern margins where the meltwater rates reach about 60 cm/yr. It can also be noted that the subglacial meltwater rate is quite low, or null below ice-thickness maxima.

Another major impact of the ice sheet is related to the isostatic adjustment of

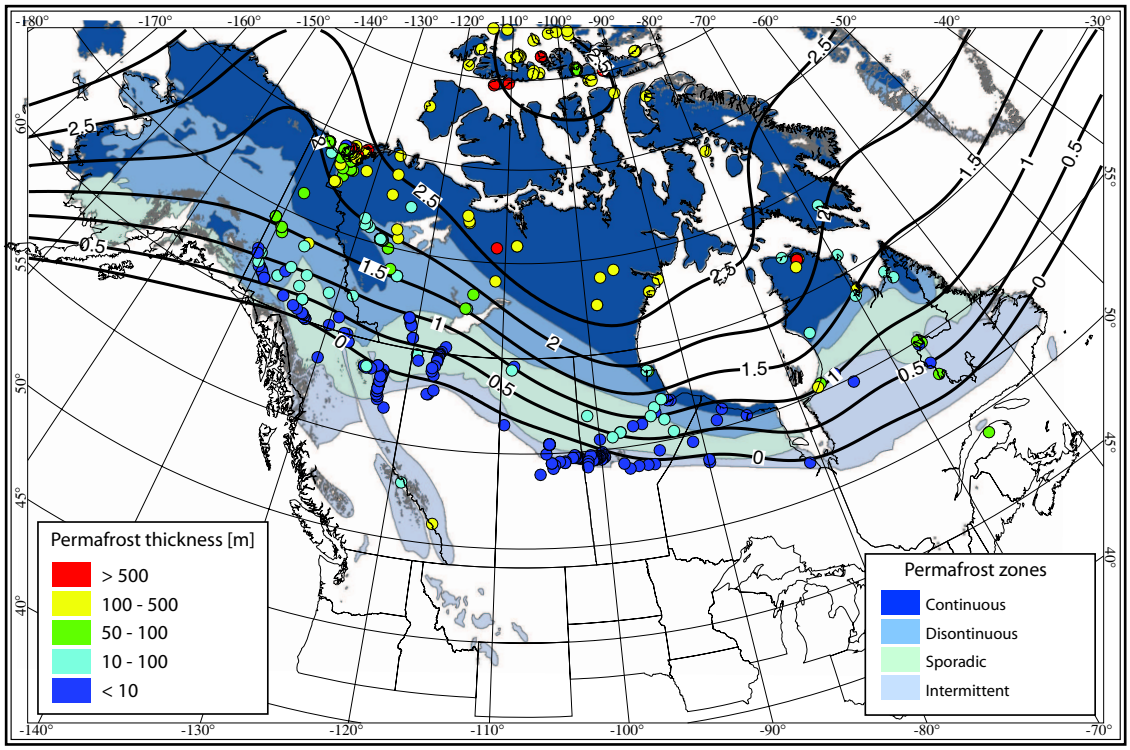

Figure 2.5: Permafrost distribution at present time. Permafrost extent is shown on a contoured blue scale. The permafrost can be continuous, discontinuous, sporadic or intermittent. The depth of the zero degree isotherm, referred as the permafrost thickness, is shown as scatter points with a rainbow color scale. The bold black contours represent the permafrost thickness interpolation of the scatter points displayed on a Log_{10} scale. Source: Smith and Burgess [2002] for the permafrost thickness database and International Permafrost Association Standing Committee on Data Information and Communication, comp. [2003] for the permafrost distribution.

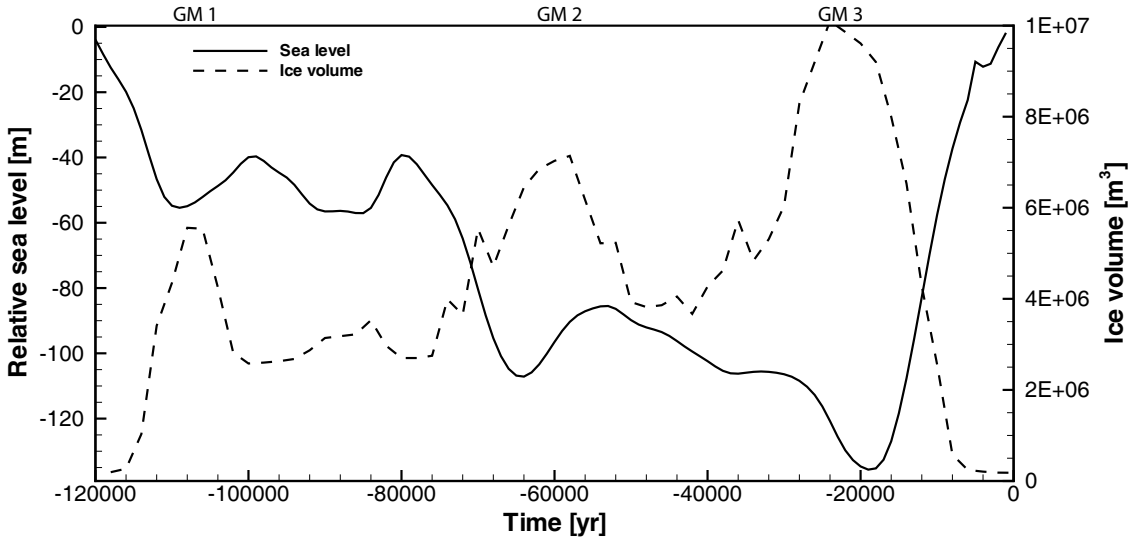

Figure 2.6: Relative sea level and continental ice volume during the last 120 kyr. Glacial maximums are indicated with the label GM1, GM2 and GM3.

the Earth's crust. Isostasy is the state of equilibrium between the Earth's crust and the mantle. The deformation of the crust by the ice sheet is such that the Earth's surface elevation will be depressed below the ice sheet and raised in its peripheral surroundings. The raised portion of the ground surface is usually referred to as the forebulge. For example, Figure 2.8 shows the surface elevation change in Waterloo for the past 120 kyr. Again, because shallow groundwater flow is strongly influenced by topography, it is important to include the temporal and spatial changes in topography in a continental-scale groundwater flow model as driven by ice-sheet dynamics over the glacial cycle.

2.5 Hydraulic Conditions During a Glacial Cycle

During a glacial cycle, the surface boundary conditions are quite different than those existing at present time and they evolve from temperate conditions to polar conditions. Let us explore plausible hydraulic conditions during a glacial cycle as a

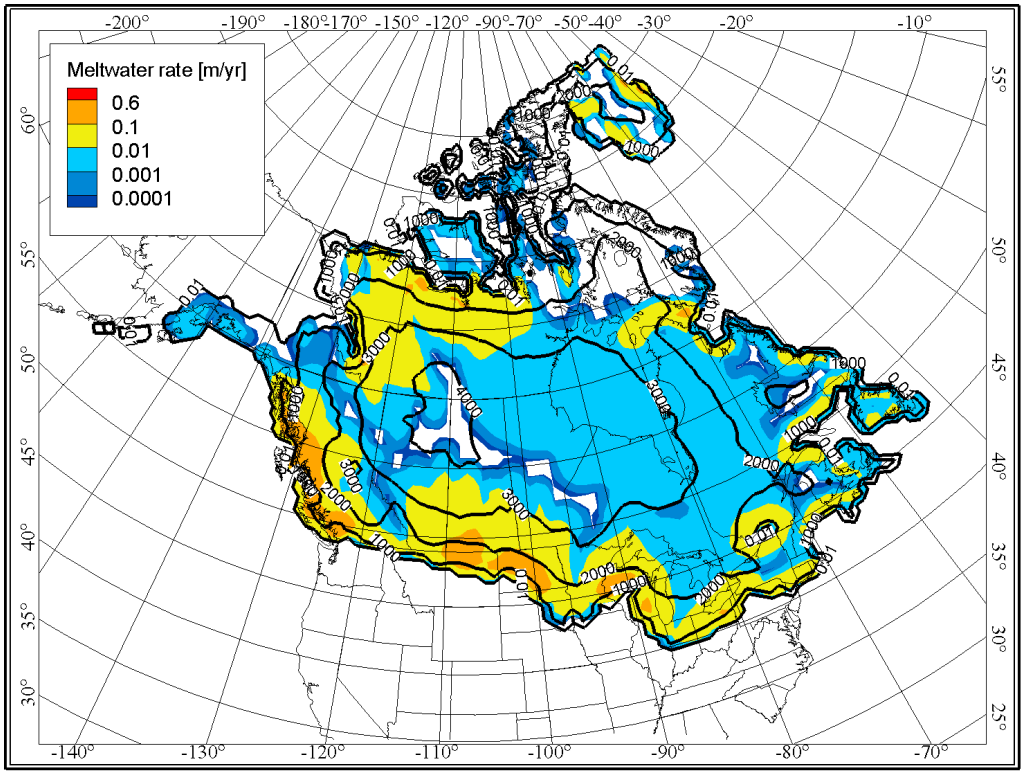

Figure 2.7: Subglacial meltrate [m/yr] at LGM. Black contour lines represent ice sheet thickness. Source: Tarasov and Peltier [2004]

consequence of global climatic changes. During the last interglacial, 120 kyr ago, the climatic conditions are believed to be quite similar to those at present and, therefore, the continental hydrogeology is surmised to be similar to present conditions: permafrost in the higher latitudes largely prevents groundwater circulation in the few first hundred meters and, at lower latitudes, groundwater flows by gravity, except where it is influenced by the presence of brines at depth. When the ice sheet begins to grow and flows from the higher latitudes to the lower latitudes, it concomitantly carries the cold temperatures with it such that the permafrost zone migrates southward with the ice sheet.

When the ice sheet grows to cover the frozen ground beyond its margins, the subglacial temperature below the advancing ice sheet warms (to a maximum of the

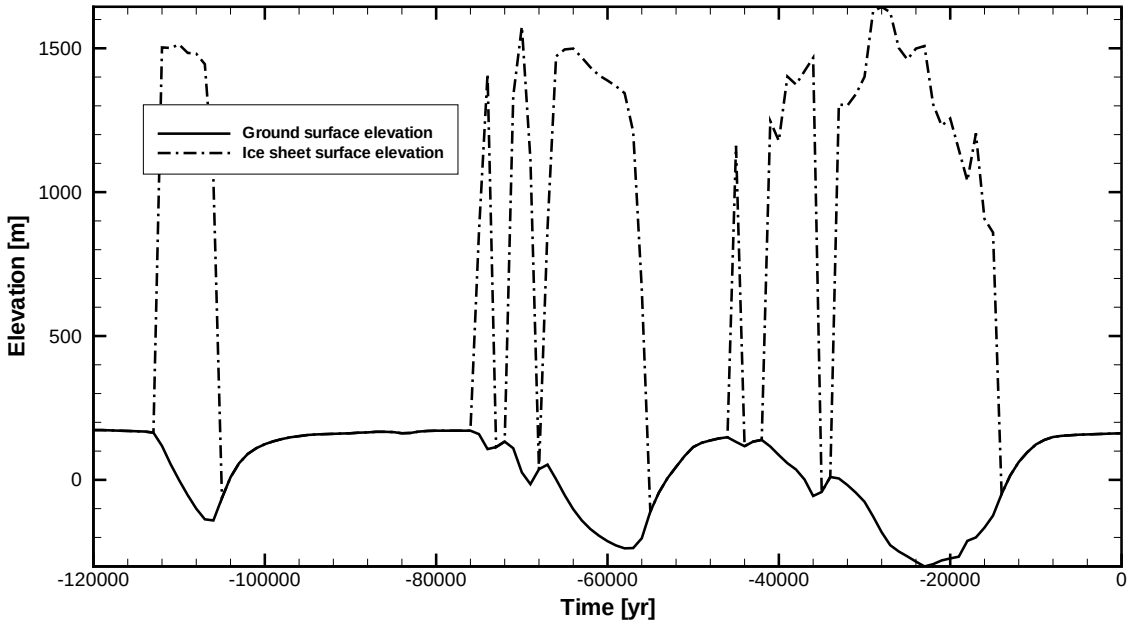

Figure 2.8: Ground surface and ice sheet surface elevations in Waterloo during the last 120 kyr. The ice sheet thickness can be deducted subtracting the surface elevation from the ice sheet surface elevation.

pressure melting point) because the Earth's surface is isolated from the cold atmospheric conditions, because of the upward geothermal gradient and because of the frictional heating at the base of the migrating ice. The pressure of the ice sheet also contributes to the lowering of the melting point of the ice, which is a few degrees lower than zero degrees Celsius. Far from the location of ice divides, the ice flows and shear heating due to friction will contribute to the production of subglacial meltwater (Figure 2.9). This meltwater exists under ice-sheet pressure and, if the permeability of the subglacial sediments or bedrock is sufficient, the meltwater will be driven into the subsurface (Figure 2.9). For the case of unconsolidated sediments, the effective pressure becomes very small, the strength of the sediments is reduced [van Weert *et al.*, 1997] and the erosion and deformation of sediments is favored [Shoemaker, 1986].

The subglacial meltwater that infiltrates into the subsurface will flow vertically

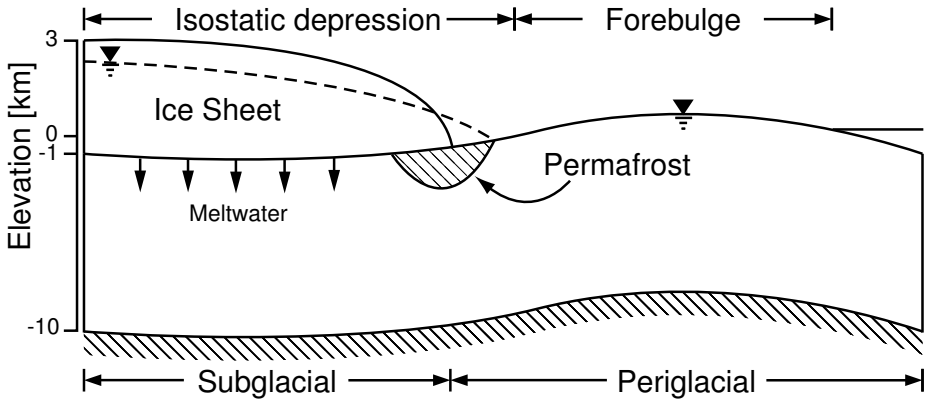

Figure 2.9: Cross section along an ice flow line showing hydraulic conditions during a glacial cycle. Extent of the subglacial and periglacial environments is also shown.

under the influence of the ice-sheet pressure as long as the ice sheet is present, and will flow from high hydraulic-head zones (i.e. under the ice sheet) to lower head zones in the subsurface which can either be subglacial regions where there is no melting or to distal areas beyond the limits of the ice sheet. Groundwater flow lines therefore mimic, in an ancillary way, the nature of ice sheet flow lines. At the tip of the ice sheet, large subsurface hydraulic gradients form over short distances, but the permeability of the subsurface can be greatly reduced by the presence of permafrost. These conditions are likely to lead to hydrofracturing in sediments and rocks at the ice sheet margin [Boulton *et al.*, 1996]. Laterally, beyond the permafrost zone, through local gaps in the discontinuous permafrost, strong upward groundwater flow is likely to occur that will lead to sediment liquefaction, sediment dyke formation and sediment expulsion structures [Boulton *et al.*, 1996].

The subglacial meltwater that does not infiltrate into the subsurface will flow laterally at the base of the ice depending on the nature of the substrate. A system of large subglacial tunnels will develop in rigid, non-deforming substrates and eskers will be the resulting deposits, while sediment deformation is likely to occur on soft-bed substrate [Clark and Walder, 1994]. Subglacial meltwater not infiltrating is believed

to flow laterally through either one of the two mechanisms described above and will ultimately express itself as surface runoff.

The weight of the ice sheet will cause the Earth's crust to deform and a new state of quasi-equilibrium will prevail each time the ice sheet grows or retreats. The deformation of the crust by the ice sheet is such that the Earth's surface elevation will be depressed below the ice sheet (isostatic depression) and raised in its far surroundings. The stress conditions under the ice sheet will be compressive, while horizontal tensile stresses will affect the forebulge [Ates *et al.*, 1997]. This will modify large-scale groundwater flow patterns because hydraulic potentials will be lowered below the ice sheet and increased in the forebulge. Another impact of the ice sheet is the additional weight imposed on the geologic medium. Depending on the elastic properties of the medium, which are a function of the rock type, compaction can reduce both the porosity and the hydraulic conductivity and increase the pore pressure.

After a glacial maximum, the ice sheet begins to melt and retreats northward quite rapidly. On the land surface, large proglacial lakes form at the ice margins in the isostatic depressions. The depth of the depressions evolves as the Earth's crust recovers to its initial state. Several large proglacial lakes formed during the last deglaciation period and their configuration, depth and extent were a result of the interactions between the location of the ice margin, the topography of the newly deglaciated surface, the elevation of the active outlet, and differential isostatic rebound [Teller, 1987].

The regressions of the ice and its weight allows the compacted rock to expand towards its initial state. Groundwater that was under ice-sheet pressure and flowing downward from the surface therefore reverses its flow direction and can now migrate upward towards the land surface. This behavior is well documented in the Michigan basin [McIntosh and Walter, 2005] and the Williston basin [Grasby *et al.*, 2000]. The permafrost regresses to the higher latitudes, progressively retreating to its cur-

rent distribution. Large amounts of sediments that were stored in the ice sheets are deposited in valleys, deltas and proglacial lakes and thus form the current landscape.

Chapter 3

Numerical Model

"Modelling is rather like masturbation–a pleasurable and harmless pastime just so long as you don't mistake it for the real thing."

Unknown French scientist[1]

The model used for this work is **HydroGeoSphere** [Therrien *et al.*, 2006] which is an extended version of the **FRAC3DVS** code [Therrien and Sudicky, 1996]. **HydroGeoSphere** is a three-dimensional control-volume finite-element numerical model describing fully-integrated subsurface and surface flow. It also solves for the advective-dispersive transport of solutes both in the surface and the subsurface and the Picard iteration algorithm is used to solve the density-dependant nonlinear flow equation. In this study, the surface component of the model was not used and therefore will not be described.

In this chapter, a brief overview of the **HydroGeoSphere** governing equations will be presented as well as the description of the additional processes and boundary conditions employed in the course of this study. A series of verification examples will be presented as well as the analytical solutions developed for each of them. Finally, a

[1]Reported by Philip [1991]

pragmatic yet plausible approach to numerically compute the portion of the subglacial meltwater that could infiltrate into the groundwater system will be described, along with the methodology for handling the influence of the presence of permafrost zones on groundwater flow system evolution.

3.1 Governing Equations

3.1.1 Darcy Equation

The Darcy equation describing density-dependant subsurface flow in **HydroGeoSphere** is given by [Frind, 1982; Graf, 2005]:

$$q_i = -K_{ij}\frac{\mu_0}{\mu}\left(\frac{\partial h^*}{\partial x_j} + \rho_r \frac{\partial z}{\partial x_j}\right) \qquad i,j = 1,2,3 \tag{3.1}$$

where q_i is the Darcy flux, K_{ij} is the hydraulic conductivity tensor, μ_0 is the reference viscosity, $\mu(T,c)$ is the actual fluid viscosity as a function of the fluid temperature and fluid composition (*i.e.*, concentration, c) and h^* is the equivalent freshwater head defined by Frind [1982] as:

$$h^* = \frac{p}{\rho_0 g} + z \tag{3.2}$$

where ρ_0 is the reference density, or density of freshwater, p is fluid pressure, g is gravitational acceleration and z is elevation above the datum. In Eq. (3.1), ρ_r is the relative density given by:

$$\rho_r = \frac{\rho}{\rho_0} - 1 \tag{3.3}$$

where ρ is the actual density of the fluid.

The hydraulic conductivity tensor is defined as:

$$K_{ij} = \frac{k_{ij}\rho_0 g}{\mu(T,c)} \qquad i,j = 1,2,3 \tag{3.4}$$

where k_{ij} is the permeability tensor. From Eq. (3.1), it can be seen that the Darcy flux is a function of both the hydraulic gradient and the buoyancy forces due to the relative density ρ_r. It should be noted that the buoyancy term $\rho_r \partial z/\partial x_j$ acts such that dense brines will tend to migrate vertically downward, or maintain their pre-existing distribution at depth, whereas the low TDS, low density water infiltrating as glacial meltwater will be constrained to occur at shallow depths. Dispersive mixing processes will, however, create a transition zone between the fresh- and brine-water regimes. A description of this transition zone requires a solution to the coupled advection-dispersion equation which is described later.

3.1.2 Fluid Continuity Equation

The three-dimensional fluid continuity equation for transient density and viscosity-dependant groundwater flow expressed in terms of an equivalent freshwater head is given by [Frind, 1982; Graf, 2005]:

$$\frac{\partial}{\partial x_i}\left(K_{ij}\frac{\partial h^*}{\partial x_j}\right) = S_s \frac{\partial h^*}{\partial t} \qquad i,j = 1,2,3 \tag{3.5}$$

where S_S is specific storage defined as [Freeze and Cherry, 1979]:

$$S_S = (\beta_{pm} + \phi\beta_f)\rho_0 g \tag{3.6}$$

where β_{pm} and β_f are, respectively, the aquifer and water compressibility and ϕ is the porous medium's porosity. Eq. (3.5) together with Eq. (3.6) is the standard equation

describing groundwater flow in a non-deformable geologic material; however due to isostasy as a consequence of glacial loading and unloading, consideration must be given to the impact of rock deformation on fluid flow. In the next section, the theory of hydromechanical coupling is reviewed and assumptions are introduced that are believed appropriate for continental-scale modelling. As will be seen, the assumption of purely vertical strain leads to a modification to Eq. (3.5).

3.1.3 One-dimensional Hydromechanical Coupling

When Theis [1935] introduced the concept of groundwater storage for the first time in hydrogeology, he was essentially extending Terzaghi's one-dimensional theory of soil consolidation to account for groundwater storage releases during aquifer depressurization due to pumpage. It is now understood that a change in pressure will lead to a deformation, and the "deformability" or compressibility of the porous medium (and fluid) will affect the degree to which the porous medium is deformed under a unit pressure change. The corollary is that a deformation produced by an external stress will result in a fluid pressure change of a magnitude related to the compressibility of the medium.

Wang [2000] and Neuzil [2003] showed that the assumption of purely vertical strain can be used to describe flow in two- and three-dimensional regimes with small resulting errors provided that only homogeneous and laterally extensive overburden changes occur. The following development demonstrates how to link a geologic strain-stress relationship to the groundwater flow equation with the above mentioned-simplification. This development makes use of the thorough treatment by Wang [2000] and the review of Neuzil [2003]. The coupling between changes in stress and changes in fluid pressure forms the subject of poroelasticity. In the following overview, the convention typically followed in rock mechanics will be used in that strain is positive for

contraction and stress is positive for compression.

Strain is a kinematic variable, defined by a symmetric, second-rank tensor:

$$\begin{aligned}
\varepsilon_{xx} &= \frac{\partial u}{\partial x} \\
\varepsilon_{yy} &= \frac{\partial v}{\partial y} \\
\varepsilon_{zz} &= \frac{\partial w}{\partial z} \\
\varepsilon_{xy} &= \frac{1}{2}\left(\frac{\partial u}{\partial y} + \frac{\partial v}{\partial x}\right) \\
\varepsilon_{xz} &= \frac{1}{2}\left(\frac{\partial u}{\partial z} + \frac{\partial w}{\partial x}\right) \\
\varepsilon_{xz} &= \frac{1}{2}\left(\frac{\partial v}{\partial z} + \frac{\partial w}{\partial y}\right)
\end{aligned} \tag{3.7}$$

where ε is strain and u, v and w are displacements in the x, y and z directions, respectively. Repeated indices indicate expansion or extension and mixed indices indicate shear. Eq. (3.7) can be written in indicial notation as:

$$\varepsilon_{ij} = \frac{1}{2}\left(\frac{\partial u_i}{\partial x_j} + \frac{\partial u_j}{\partial x_i}\right) \tag{3.8}$$

where u_i is the displacement in the i-direction and each of the subscripts i and j represent the Cartesian coordinate axes x, y, and z, respectively. Strain is a kinematic variable because it is calculated from the spatial derivative of the displacement.

The causal forces that produce motion are the dynamic variables stress and pore pressure. As for the kinematic variables, stress is a second-rank tensor while pore pressure is a scalar. The forces, when there is no transient elastic wave propagation

in the porous medium, balance as follows:

$$\begin{aligned}\frac{\partial \sigma_{xx}}{\partial x}+\frac{\partial \sigma_{yx}}{\partial y}+\frac{\partial \sigma_{zx}}{\partial z}&=0\\ \frac{\partial \sigma_{xy}}{\partial x}+\frac{\partial \sigma_{yy}}{\partial y}+\frac{\partial \sigma_{zy}}{\partial z}&=0\\ \frac{\partial \sigma_{xz}}{\partial x}+\frac{\partial \sigma_{yz}}{\partial y}+\frac{\partial \sigma_{zz}}{\partial z}&=0\end{aligned} \tag{3.9}$$

where σ denotes the stresses on the faces of a control volume of the porous medium. The sum of the three normal stresses, $\sigma_{kk}=\sigma_{xx}+\sigma_{yy}+\sigma_{zz}$ is the *octahedral* stress, or volumetric stress, and it equals three times the mean normal stress $(\sigma_{xx}+\sigma_{yy}+\sigma_{zz})/3$.

An increase in an applied extensional stress expands a rock mass to the same extent as an equal increase in pore pressure. Similarly, a change in the applied compressive stress to a rock mass tends to offset a change in fluid pore pressures. The rock behavior is governed by the relation between total stress and pore pressure under the concept of *effective stress* as elucidated by Terzaghi at the beginning of the 20th Century. Terzaghi defined the principal effective stress, σ', as $\sigma'_i=\sigma_i-p$ where i =1, 2, 3 and p is the fluid pressure. Terzaghi's classic effective stress law has since been generalized as [see, e.g., Wang, 2000]:

$$\frac{\sigma'_{kk}}{3}=\frac{\sigma_{kk}}{3}-\alpha p \tag{3.10}$$

where p is fluid pressure, $\alpha=1-K/K_s$, K is the drained bulk modulus of the porous medium and K_s is the modulus of the solids comprising the porous medium. The bulk modulus, K, of a medium is the ratio of the change in pressure to the fractional volume compression:

$$K=\frac{\Delta P}{\Delta V/V} \tag{3.11}$$

The reciprocal of the bulk modulus is called compressibility. It can be seen that

if the solid grains are considered incompressible, $1/K_s = 0$ and $\alpha = 1$. Eq. (3.10) implies that volumetric strain, $\varepsilon_{kk} = \varepsilon_{xx} + \varepsilon_{yy} + \varepsilon_{zz}$, is related to effective stress rather than normal stress:

$$\varepsilon_{kk} = \frac{1}{K}\left(\frac{\sigma_{kk}}{3} - \alpha p\right) \tag{3.12}$$

The stress and strain tensors each contain six components. However, the shear stress σ_{ij} and shear strains ϵ_{ij} $(i \neq j)$ are zero in principal coordinates. The constitutive equations that relate stress and strain in the principal directions are

$$\begin{aligned}
\varepsilon_{xx} &= \frac{1}{2G}\left[\sigma_{xx} - \frac{\nu}{1+\nu}\sigma_{kk}\right] - \frac{\alpha}{3K}p \\
\varepsilon_{yy} &= \frac{1}{2G}\left[\sigma_{yy} - \frac{\nu}{1+\nu}\sigma_{kk}\right] - \frac{\alpha}{3K}p \\
\varepsilon_{zz} &= \frac{1}{2G}\left[\sigma_{zz} - \frac{\nu}{1+\nu}\sigma_{kk}\right] - \frac{\alpha}{3K}p
\end{aligned} \tag{3.13}$$

and the three additional equations which relate the shear strains to the shear stresses are

$$\begin{aligned}
\varepsilon_{xy} &= \frac{1}{2G}\sigma_{xy} \\
\varepsilon_{yz} &= \frac{1}{2G}\sigma_{yz} \\
\varepsilon_{xz} &= \frac{1}{2G}\sigma_{xz}
\end{aligned} \tag{3.14}$$

where G is the shear modulus and ν is the drained Poisson's ratio.

Eq. (3.14) does not contain a pore pressure term because changes in pore pressure are assumed not to induce shear strain. Eqs. (3.13) and (3.14) can be represented by

a single equation, written in indicial notation:

$$\underbrace{\varepsilon_{ij}}_{\textit{Total strain}} = \underbrace{\frac{1}{2G}\left[\sigma_{ij} - \frac{\nu}{1+\nu}\sigma_{kk}\delta_{ij}\right]}_{\textit{Poroelastic strain}} + \underbrace{\frac{\alpha}{3K}p\delta_{ij}}_{\textit{Free strain}} \tag{3.15}$$

This formulation relating strain to the dependant variable stress is usually called the pure compliance formulation. In the above, the Kronecker delta is defined as:

$$\delta_{ij} = \begin{cases} 1 & \text{if} \quad i = j \\ 0 & \text{if} \quad i \neq j \end{cases} \tag{3.16}$$

The total strain in Eq. (3.15) can be viewed as the sum of a poroelastic strain and a free strain. The total strain is the strain that would be measured by a strain gauge at a point in the body. The free strain is the strain that would be measured if the rock mass about a point was unconstrained. The free normal strains are equal in all directions and no free shear strains are produced. Therefore, an unconstrained body undergoes uniform volumetric dilatation and would appear as a replica of itself when subjected to uniform pore pressure increase. On the other hand, a non-uniform pore pressure distribution or constraints imposed by boundaries induce poroelastic stresses σ_{ij} in the body. Poroelastic strains accommodate the differential free strains in adjacent rock mass.

The constitutive relations shown in Eqs. (3.13) to (3.15) can also be expressed with stress as the dependent variable. In indicial notation, this relationship, which is often called the mixed stiffness formulation, is given by:

$$\sigma_{ij} = 2G\varepsilon_{ij} + 2G\frac{\nu}{1+\nu}\varepsilon_{kk}\delta_{ij} + \alpha p\delta_{ij} \tag{3.17}$$

A description of deformation in a poroelastic rock formation can be cast in terms of displacements, stresses or strain. In order to obtain the strain and stress formulations, a few more derivations are needed because the six components of strain are uniquely described by only three components of displacement u, v and w. The components of stress and strain are therefore not independent. The interrelations between them is known as compatibility conditions. Those conditions can be derived from the definitions of the components of strain given in Eq. (3.7):

$$\begin{aligned}
2\frac{\partial^2\varepsilon_{xy}}{\partial x\partial y} &= \frac{\partial^2\varepsilon_{xy}}{\partial y^2}+\frac{\partial^2\varepsilon_{yy}}{\partial x^2}\\
2\frac{\partial^2\varepsilon_{yz}}{\partial y\partial z} &= \frac{\partial^2\varepsilon_{yy}}{\partial z^2}+\frac{\partial^2\varepsilon_{zz}}{\partial y^2}\\
2\frac{\partial^2\varepsilon_{xy}}{\partial z\partial x} &= \frac{\partial^2\varepsilon_{zz}}{\partial x^2}+\frac{\partial^2\varepsilon_{xx}}{\partial z^2}\\
\frac{\partial^2\varepsilon_{xx}}{\partial y\partial z} &= \frac{\partial}{\partial x}\left(-\frac{\partial\varepsilon_{yz}}{\partial x}+\frac{\partial\varepsilon_{xz}}{\partial y}+\frac{\partial\varepsilon_{xy}}{\partial z}\right)\\
\frac{\partial^2\varepsilon_{yy}}{\partial z\partial x} &= \frac{\partial}{\partial y}\left(\frac{\partial\varepsilon_{yz}}{\partial x}-\frac{\partial\varepsilon_{zx}}{\partial y}+\frac{\partial\varepsilon_{yx}}{\partial z}\right)\\
\frac{\partial^2\varepsilon_{zz}}{\partial x\partial y} &= \frac{\partial}{\partial z}\left(-\frac{\partial\varepsilon_{zy}}{\partial x}+\frac{\partial\varepsilon_{zx}}{\partial y}-\frac{\partial\varepsilon_{xy}}{\partial z}\right)
\end{aligned} \tag{3.18}$$

Substituing the constitutive relations for strain in terms of stress (Eq. (3.15)) and the force equilibrium equations (Eq. (3.9)) into the compatibility relations (Eq. (3.18)) leads to the equation governing deformation written in term of stresses:

$$\nabla^2\sigma_{ij}+\frac{1}{1+\nu}\frac{\partial^2\sigma_{kk}}{\partial x_i\partial x_j}+\frac{1-2\nu}{1-\nu}\left[\frac{1-\nu}{1+\nu}\frac{\partial^2 p}{\partial x_i\partial x_j}+\delta_{ij}\nabla^2 p\right]=0 \tag{3.19}$$

When summing the principal direction components of Eq. (3.19) and rearranging, one obtains a relatively simple relationship between changes in stress and fluid pressure:

$$\nabla^2\sigma_{kk}=\frac{2\,(1-2\nu)}{1-\nu}\alpha\nabla^2 p \tag{3.20}$$

Eq. (3.20) represents the stress in a poroelastic formation as governed by the force equilibrium and compatibility relationships subject to appropriate boundary conditions.

Equations of Fluid Flow

A manifestation of the traditional equation of fluid flow as given by Eq. (3.5) is derived here based on poroelastic theory, which will lead to a relation between mechanical deformation and fluid pressure. In the previous section, it was shown that the equations of deformation are based on force equilibrium. For fluid flow, the equation is based on mass conservation and can be written as follows:

$$\frac{\partial}{\partial t}\left(\rho\phi\right) + \nabla \cdot \left(\rho \mathbf{q}\right) - J = 0 \tag{3.21}$$

where ρ is the fluid density, ϕ is porosity, and $\mathbf{q}$ is the Darcy flux. The first component of Eq. (3.21) describes the change in fluid stored in the representative elementary volume (REV), the second term represents the net fluid flux across the REV faces and J is a fluid source or sink (a pumping well for example). Letting $m = \rho\phi$ denote the mass of the pore fluid per unit volume of porous formation, changes in this quantity can be written as:

$$m - m_0 = \left(\rho - \rho_0\right)\phi_0 + \rho_0\left(\phi - \phi_0\right) \tag{3.22}$$

The description of porosity changes in terms of compression moduli has been described by Rice and Cleary [1976] and the description of porosity change caused by stress and fluid pressure is given by:

$$\phi - \phi_0 = -\left(\frac{1}{K} - \frac{1}{K_s}\right)\frac{\sigma_{kk}}{3} + \left(\frac{1}{K} - \frac{1}{K_s} - \frac{\phi}{K_s}\right)p \tag{3.23}$$

Likewise, fluid density changes due to pressure changes are given by:

$$\rho - \rho_0 = \rho_0 \frac{p}{K_f} \tag{3.24}$$

where K_f is the fluid bulk modulus. Substituing Eqs. (3.23) and (3.24) into Eq. (3.22) yields:

$$m - m_0 = -\rho_0 \left(\frac{1}{K} - \frac{1}{K_s}\right) \frac{\sigma_{kk}}{3} + \rho_0 \left[\left(\frac{1}{K} - \frac{1}{K_s}\right) + \left(\frac{\phi_0}{K_f} - \frac{\phi_0}{K_s}\right)\right] p \tag{3.25}$$

Force equilibrium is applied to the fluid (as for the porous medium) but through a constitutive relationship that relates fluid flux and driving forces for the fluid flux. For geologic applications, Darcy's law is appropriate and is given in pressure terms by:

$$\mathbf{q} = \frac{\mathbf{k}}{\mu} \left(\nabla p + \rho g \nabla z\right) \tag{3.26}$$

where $\mathbf{k}$ is the formation permeability tensor, μ is fluid viscosity, g is gravitational acceleration and z is elevation above an arbitrary datum. Substituting Eqs. (3.25) and (3.26) into the fluid mass conservation equation (Eq. (3.21)) yields:

$$\nabla \cdot \frac{\mathbf{k}}{\mu} \left(\nabla p + \rho g \nabla z\right) = \rho \left[\left(\frac{1}{K} - \frac{1}{K_s}\right) + \left(\frac{\phi_0}{K_f} - \frac{\phi_0}{K_s}\right)\right] \frac{\partial p}{\partial t} - \rho \left(\frac{1}{K} - \frac{1}{K_s}\right) \frac{\partial \sigma_t}{\partial t} - J \tag{3.27}$$

where $\sigma_t = \sigma_{kk}/3$ denotes the mean total stress. The three-dimensional specific storage, S_{s3} and three-dimensional loading efficiency, B, can be defined as:

$$S_{s3} = \rho g \left[\left(\frac{1}{K} - \frac{1}{K_s}\right) + \left(\frac{\phi_0}{K_f} - \frac{\phi_0}{K_s}\right)\right] \tag{3.28}$$

and

$$B = \frac{\left(\frac{1}{K} - \frac{1}{K_s}\right)}{\left(\frac{1}{K} - \frac{1}{K_s}\right) + \left(\frac{\phi_0}{K_f} - \frac{\phi_0}{K_s}\right)} \tag{3.29}$$

B is also known as Skempton's coefficient. Skempton's coefficient represents the ratio of the change in fluid pressure to a change in mean total stress under undrained conditions. For highly compressible media, B approaches unity while in very stiff media it is close to zero. Substituting these definitions in Eq. (3.27) gives

$$\nabla \cdot \frac{\mathbf{k}\rho g}{\mu} \left(\nabla p + \rho g \nabla z\right) = S_{s3} \frac{\partial p}{\partial t} - S_{s3} B \frac{\partial \sigma_t}{\partial t} - gJ \tag{3.30}$$

The terms on the right hand side represent the effects of fluid storage, stress change and fluid sources/sinks, respectively. Eq. (3.30) is the transient three-dimensional flow equation coupled with 3D hydromechanical deformation. Describing fully-coupled fluid flow and deformation requires the solution of the stress equation (Eq. (3.20)) along with the flow equation (Eq. (3.30)) in a coupled fashion. This is computationally burdensome and beyond feasibility for continental-scale modelling over a glacial period. Therefore some simplifications are needed.

The Purely Vertical Strain Assumption

The mechanical deformation and fluid flow equations can be partially de-coupled under certain conditions. Compaction and decompaction due to deposition or erosion, for example, involve load changes that are relatively homogeneous areally, especially over geologic time frames. For the case of a temporally-variable but areally homogeneous load, the lateral strains ϵ_{xx} and ϵ_{yy} in Eq. (3.13) are zero but changes in the vertical stress σ_{zz} are not. Under these conditions, the three components of Eq. (3.13)

can be added to arrive at:

$$\sigma_{kk} = \frac{2\,(1-2\nu)}{1-\nu}\alpha p + \frac{3\,(1+\nu)}{3\,(1+\nu) - 2\alpha B\,(1-2\nu)}\,(1-\lambda B)\,\sigma_{zz} \tag{3.31}$$

If the overburden loading is homogeneous and laterally extensive, the change in vertical stress should also be spatially homogeneous. Therefore, $\nabla^2\sigma_{zz} = 0$ and applying the ∇^2 operator to Eq. (3.31) yields:

$$\nabla^2\sigma_{kk} = \frac{2\,(1-2\nu)}{1-\nu}\alpha\nabla^2 p \tag{3.32}$$

which is exactly the same as Eq. (3.20), which means that force equilibrium and compatibility conditions are automatically satisfied, thus de-coupling the flow and deformation equations. Substituing Eq. (3.31) into Eq. (3.30) and simplifying, the resulting flow equation is:

$$\nabla\cdot\frac{\mathbf{k}\rho g}{\mu}\left(\nabla p + \rho g\nabla z\right) = S_s\frac{\partial p}{\partial t} - S_s\zeta\frac{\partial\sigma_{zz}}{\partial t} - gJ \tag{3.33}$$

where S_s is the one-dimensional specific storage coefficient [van der Kamp and Gale, 1983] given by:

$$S_s = S_{s3}\,(1-\lambda B) = \rho g\left[\left(\frac{1}{K} - \frac{1}{K_s}\right)(1-\lambda) + \left(\frac{\phi}{K_f} - \frac{\phi}{K_s}\right)\right] \tag{3.34}$$

In Eq. (3.33), ζ is the one-dimensional loading efficiency given by

$$\zeta = \frac{B\,(1+\nu)}{3\,(1-\nu) - 2\alpha B\,(1-2\nu)} \tag{3.35}$$

Eq. (3.33) alone provides a complete description of transient flow in the presence of vertical stress changes. To account for the change in overburden load with time,

$\partial\sigma_{zz}/\partial t$ must be specified. Eq. (3.33) can also be written using hydraulic conductivity, K, rather than intrinsic permeability, $\mathbf{k}$, and hydraulic head, h, instead of pressure, p:

$$\nabla \cdot K\nabla h = S_s\frac{\partial h}{\partial t} - S_s\zeta\frac{1}{\rho g}\frac{\partial \sigma_{zz}}{\partial t} - \frac{J}{\rho} \tag{3.36}$$

Finally, by noting that $K' = [3(1-\nu)/(1+\nu)]K$ and by assuming that the grains are incompressible ($K_s = \infty$), Eq. (3.34) reduces to:

$$S_s = \rho g\left(\frac{1}{K'} - \frac{\phi}{K_f}\right) \tag{3.37}$$

which is the specific storage definition commonly used by hydrogeologists. The assumption of incompressible grains simplifies the definition of loading efficiency coefficient and using the definitions of fluid compressibility, β_f, and porous medium compressibility, β_{pm}, the loading efficiency coefficient becomes:

$$\zeta = \frac{\beta_{pm}}{\beta_{pm} + \phi\beta_f}, \tag{3.38}$$

and the one-dimensional specific storage S_s becomes:

$$S_s = \rho g\left(\beta_{pm} + \phi\beta_f\right). \tag{3.39}$$

Although it is possible to compute the loading efficiency coefficient using data for the compressibility of the porous medium and water, and Poisson's ratio, the paucity of representative data introduces considerable uncertainty. A value for loading efficiency is often chosen between zero and one and a sensitivity analysis performed.

It is also important to note that Eq. (3.36) only describes the pressure changes in fluid due to vertical strain but not the deformation itself that would reduce the pore space. As pointed out by Neuzil [2003], the finite vertical deformation can be

accounted for by tracking the effective stress and specifying a porosity-effective stress relationship. In the course of this study, the porosity reduction was neglected because it is believed to be small in hard rocks such as the Canadian Shield.

3.1.4 Solute Continuity Equation

The three-dimensional solute continuity equation for a conservative solute is given by:

$$\frac{\partial}{\partial x_i}\left(\phi D_{ij}\frac{\partial c}{\partial x_j} - q_i c\right) + \Gamma_{1st} = \frac{\partial\left(\phi c\right)}{\partial t} \qquad i,j = 1,2,3 \tag{3.40}$$

where c is the solute concentration and Γ_{1st} is a first-order source term. The hydrodynamic dispersion coefficient, which accounts for mechanical dispersion and molecular diffusion, is given by [Bear, 1972]:

$$\phi D_{ij} = \left(\alpha_l - \alpha_t\right)\frac{q_i q_j}{|q|} + \alpha_t |q|\,\delta_{ij} + \phi\tau D^*\delta_{ij} \tag{3.41}$$

where α_l and α_t are the longitudinal and the transverse dispersivities, $|q|$ is the magnitude of the Darcy flux, τ is the matrix tortuosity, D^* is the solute free diffusion coefficient, and δ_{ij} is the Kronecker delta which is equal to one when $i = j$ and zero when $i \neq j$. The product τD^* represents an effective diffusion coefficient for the matrix. In Eq. (3.40), the assumption of fluid incompressibility is made.

The concentration variable is linked to the fluid density with the following linear relationship:

$$\rho_r = \gamma\frac{c}{c_{\max}}, \tag{3.42}$$

where c_{max} is the maximum fluid concentration and the dimensionless constant γ is

the maximum relative density given by:

$$\gamma = \frac{\rho_{max}}{\rho_0} - 1 \tag{3.43}$$

where the assumption is made that the relative solute concentration of a fluid with the density $\rho = \rho_{max}$ is $c/c_{max} = 1$. Because of the dependence of fluid flow (Eq. (3.36)) and parameters appearing in it on the fluid density and viscosity, it is necessary to couple the flow Eq. (3.36), expressed here in terms of equivalent freshwater heads, and the solute transport Eq. (3.40) because of the interactions involved. In **HydroGeoSphere**, the two nonlinear equations are solved via Picard iteration at each time step.

3.1.5 Brine Formation

It was discussed in Chapter 2 that the origin of brines in the Canadian Shield is still in debate. Also, because the brine distribution both areally and with depth is not known *a priori*, simulations will be performed to obtain the estimated patterns using the available database of Frape and Fritz [1987] as a benchmark. The different approaches for a brine-distribution "startup" in the model will be discussed in the next chapter but because one of the approaches employed involved some code development, this approach is presented next.

In order to represent brine formation, a process that depends in the difference of concentration between TDS in the fluid and a potential maximum concentration generated by rock weathering, leaching of saline fluid inclusions or other processes is used. A first-order source term, Γ_{1st}, is defined as [Provost *et al.*, 1998]

$$\Gamma_{1st} = k_{mt} \left(c_{\max} - c \right) \tag{3.44}$$

where k_{mt} is a mass transfer coefficient rate describing rock-water mass interactions and c_{max} is the maximum allowable fluid concentration. The maximum allowable fluid concentration, c_{max}, could represent the saturation concentration of TDS in the case of rock weathering or the concentration of TDS in fluid inclusion, in the case of leaching [Provost *et al.*, 1998].

As Provost *et al.* [1998] point out, this simple expression for the formation of brine captures two basic features of rock-water interactions: the rate at which the solids dissolve diminishes as the concentration of the resident fluid increases, and dissolution ceases when the maximum concentration is reached. This approach has the advantage of its simple formulation and because it is a first-order approximation to Fick's law of diffusion that describes mass transfer between mobile and immobile fluid zones.

Provost *et al.* [1998] demonstrated that the first-order brine generation algorithm, when applied to the Fennoscandian Shield in Sweden, does not require a large quantity of salt to be transferred from the rock to the fluid in order to generate typical brine concentrations in the resident fluid. For a shield environment, they showed that, for a fluid inclusion void fraction of 0.01 and an initial solute mass fraction of 0.3 in the inclusions, less that 1% of the dissolved solids in the inclusions is depleted after 10 million years of continuous leaching.

3.2 Verification Problems

In this section, the implementation of 1D hydromechanical coupling and brine generation in the **HydroGeoSphere** code is verified by comparison to exact analytical solutions. Because previously published solutions are unknown, simple 1D analytical solutions were specifically developed for each case. Along with verifying the code, the analytical solutions provide an efficient basis to grasp the basic impacts of select

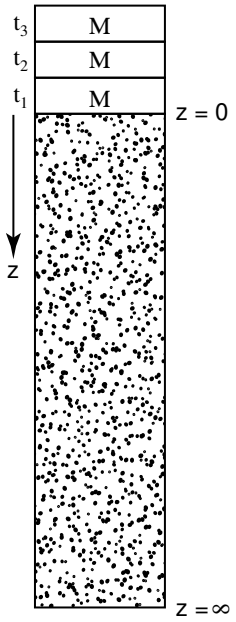

Figure 3.1: 1D soil column.

processes on flow and solute transport.

3.2.1 1D Hydromechanical Coupling

A 1D vertical column of sand is shown in Figure 3.1. The column has a semi-infinite length and is fully saturated. A mass (or load) M is added at the inlet at constant intervals such that dM/dt is a constant. M can be converted to an equivalent water height using the density of water and could represent an ice sheet forming above an aquifer, for example. The top of the column is drained and the bottom is a no-flow boundary condition.

Analytic solution

The governing equation describing flow along the column with mechanical loading is a simplification along the vertical dimension of Eq. (3.36). It is given by:

$$D\frac{\partial^2 h}{\partial z^2} - \frac{\partial h}{\partial t} + \frac{q_{in}}{S_s} = 0 \tag{3.45}$$

where $D = K_{zz}/S_s$ is hydraulic diffusivity and:

$$q_{in} = S_s\zeta\frac{\partial\left(\sigma_{zz}/\rho g\right)}{\partial t} \tag{3.46}$$

is the source term due to external loading.

The initial and boundary conditions are given by:

$$\text{I.C.}: \quad h\left(z, t=0\right) = 0 \tag{3.47}$$

$$\text{B.C.1}: \quad h\left(z=0, t\right) = 0 \tag{3.48}$$

$$\text{B.C.2}: \quad \frac{\partial h\left(z=\infty, t\right)}{\partial z} = 0 \tag{3.49}$$

Eq. (3.45) is a second-order non-homogeneous partial differential equation (PDE) that can be solved with integral transforms. Applying the Laplace transform to Eq. (3.45) yields:

$$\frac{d^2\bar{h}}{dz^2} - \frac{p\bar{h}}{D} + \frac{q_{in}}{DS_s}\frac{1}{p} = 0 \tag{3.50}$$

where $\bar{h}$ is the Laplace transformation of h, defined as:

$$\bar{h}\left(x, p\right) = \int_0^\infty \exp\left(-pt\right)h\left(x, t\right)dt \tag{3.51}$$

Eq. (3.50) is a second-order non-homogeneous ordinary differential equation (ODE) with the following solution:

$$\bar{h} = A\exp\left(z\sqrt{p/D}\right) + B\exp\left(-z\sqrt{p/D}\right) + \frac{q_{in}}{S_s p^2} \tag{3.52}$$

where A and B are constants of integration. The constant A is found to be null when using the second boundary condition (Eq. (3.49)). The first boundary condition (Eq. (3.48)) is used to solve for the constant B:

$$B = -\frac{q_{in}}{S_s p^2} \tag{3.53}$$

The solution for Eq. (3.50) is therefore:

$$\bar{h} = \frac{q_{in}}{S_s p^2} - \frac{q_{in}}{S_s p^2} \exp\left(-z\sqrt{p/D}\right) \tag{3.54}$$

It is possible to invert this solution from Laplace space to real-time space using tables from Carslaw and Jaeger [1959]. The solution for the hydraulic head along the column is :

$$h(z,t) = \frac{\partial \sigma_{zz}}{\partial t} t - \frac{\partial \sigma_{zz}}{\partial t}\left(t + \frac{z^2}{2D}\right) \operatorname{erfc}\left(\frac{z}{2\sqrt{Dt}}\right) - z\sqrt{\frac{t}{\pi D}} \exp\left(-\frac{z^2}{4Dt}\right) \tag{3.55}$$

Numerical solution

The physical system described above is modelled using **HydroGeoSphere**. The analytical solution was developed for a semi-infinite domain and, therefore, to compare the numerical solution with the analytical solution, a domain of 10 000 m length was used. The system represents a 1D vertical column of length 10 000 m on to which an ice sheet is taken to grow in thickness at a rate of 0.32 meters of ice per year, which is equivalent to 0.3 meters of water equivalent loading per year for 10 000 years. The top of the column is drained and as such a specified head of 0.0 m was assigned in the model. The initial head along the length of the column is set to 0 m. The properties of the rock mass are described in Table 3.1. A loading efficiency of unity was used in this "base-case" scenario.

Table 3.1: Material properties.

Properties	Value
K_{zz} [m/yr]	1.0×10^{-3}
S_s [m^{-1}]	1.0×10^{-6}
ζ [-]	1.0

Figure 3.2 shows the hydraulic head versus time at different depths in the column. It can be seen that the numerical solution precisely corresponds to the analytical solution results. It can also be seen that after 10 000 yrs, the head at at a depth of 500 m reaches a value of about 500 m. Figure 3.3 shows vertical profiles of heads along the column at various times. Again, the numerical solution fits the analytical solution very well. It also indicates that the head along the column increases with depth, noting that the low head value near the surface is due to the specified head boundary condition. It is clear that the impact of the ice-sheet loading occurs along the entire vertical length of the column given that the initial head was 0.0 m along its length. The maximum head equals about 925 m at a depth of 1000 m after 10 000 years.

The analytical solution was further explored to capture the sensitivity of the values of the loading efficiency on the solution. Figure 3.4 shows the head solution along the column after 10 000 years using different values of the loading efficiency parameter as input. It can be seen that the load transfer to fluid pressure is maximum when the loading efficiency is maximum. As the loading efficiency diminishes, the maximum head becomes lower since more of the externally-applied load is supported by the matrix.

The primary effect of surface loading is to decrease the porespace, which in turn increases the pore pressure. If the loading occurs on a surface and the water is allowed to drain out of the soil, the consequence of the surface loading will be groundwater

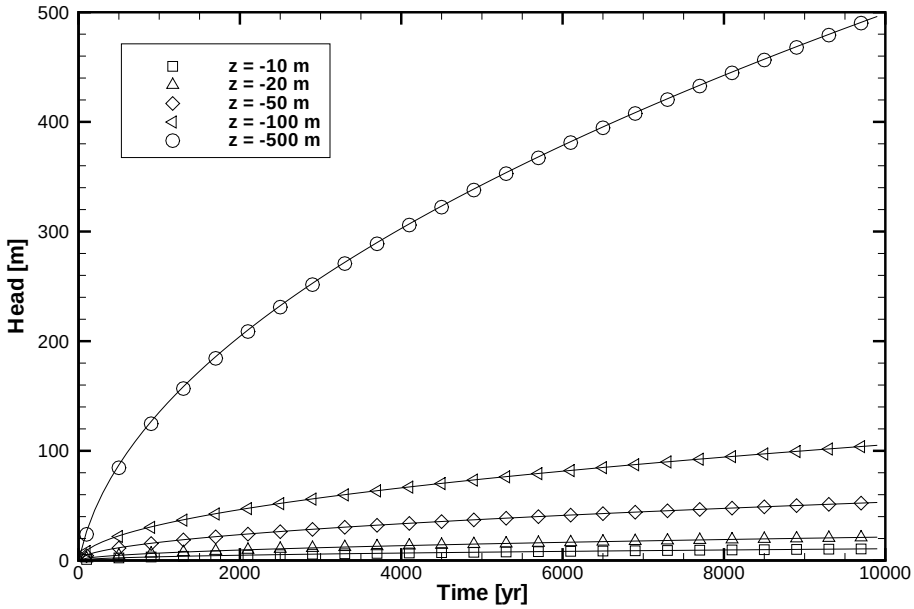

Figure 3.2: Hydraulic head vs. time at different depths along the column. Solid lines represent analytical solution and symbols represent the numerical solution.

exfiltration on the surface because the hydraulic head in the subsurface will become higher than that of the surface. On the other hand, if a specified head is applied on the surface along with surface loading, there will be infiltration into the subsurface as long as the head on the surface is higher than in the subsurface, which would occur for loading efficiency values below 1.0. During unloading, the opposite would happen; if the top of the column is drained, water would infiltrate into the subsurface to fill the porespaces that are inflating due to surface unloading. In the case of a surface specified head, exfiltration would occur during unloading because the head in the subsurface would be higher than that at the surface because large infiltration would have occurred earlier and raised the hydraulic head at depth.

To explore this behavior, the boundary condition at the surface of the column was altered in order to study its impact on the surface/subsurface water interaction at the ice sheet sole. The simulation of the 1D column was extended for 20 kyr over which, during the first 10 kyr, a loading rate identical to the base case was applied.

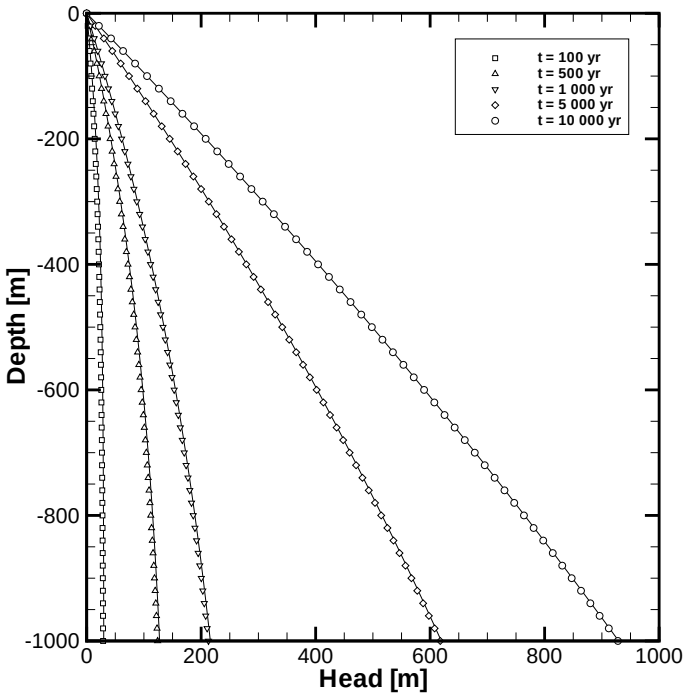

Figure 3.3: Hydraulic head vs. depth at different times. Solid lines represent analytical solution and symbols represent the numerical solution.

During the remaining 10 kyr, the ice sheet was assumed to melt at the same rate. The loading efficiency is set to 0.2 and values will be modified from this value to capture its impact on surface/subsurface water interactions.

Figure 3.5 illustrates the surficial exchange flux for the base-case scenario over the duration of the simulation period. It can be seen that, as expected, if the top of the column is drained, water can exfiltrate from the subsurface to the surface during ice-sheet buildup due to porespace reduction. During the melting period (10 - 20 kyr), water infiltrates into the subsurface to fill the inflating pore space.

The base-case scenario will now be modified using a specified head equal to the ice-sheet equivalent freshwater head applied on the surface. The surface head will vary linearly from 0 m at the beginning of the simulation to 3 000 m at 10 kyr and reverts back to 0 m at the end of the simulation, at 20 kyr. It can be seen from

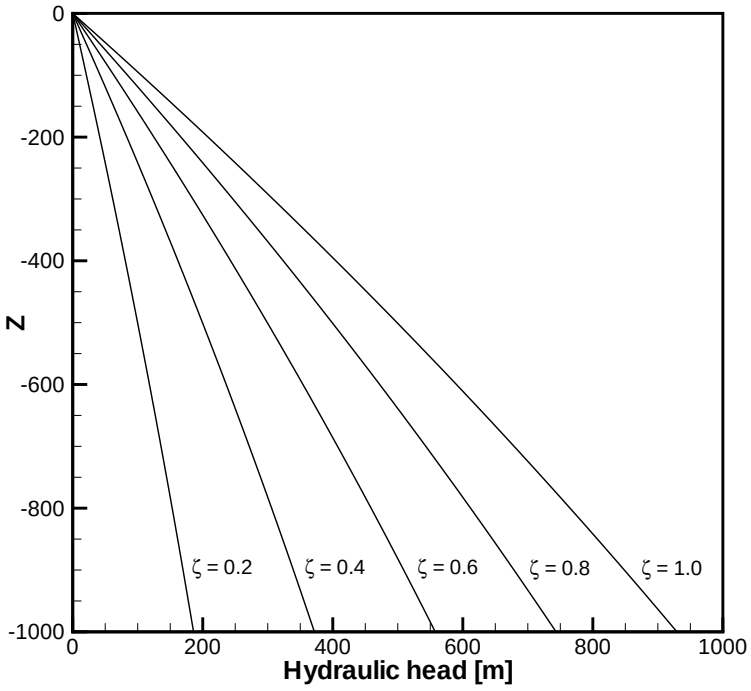

Figure 3.4: Hydraulic head vs. depth for different loading efficiency values.

Figure 3.5 that the exchange flux is reversed from the base case; during the first 10 kyr, water infiltrates into the subsurface because the head at the surface is higher than the values just into the subsurface. During ice-sheet melting, the water exfiltrates on the surface because the hydraulic gradient is reversed. The magnitude of the water exchange flux at the surface is clearly dependent on the value of the loading efficiency as can be seen in Figure 3.5. The loading efficiency parameter was varied from the base-case value and it can be seen that the exchange flux is maximum when $\zeta = 0.0$ and null when $\zeta = 1.0$. The exchange flux is null when $\zeta = 1.0$ because all the weight of the ice sheet is transferred to the fluid so there is no hydraulic gradient between the surface and the subsurface. The surface/subsurface water interaction dynamics are therefore a function of the interaction between the subglacial boundary conditions and the elastic properties of the rocks

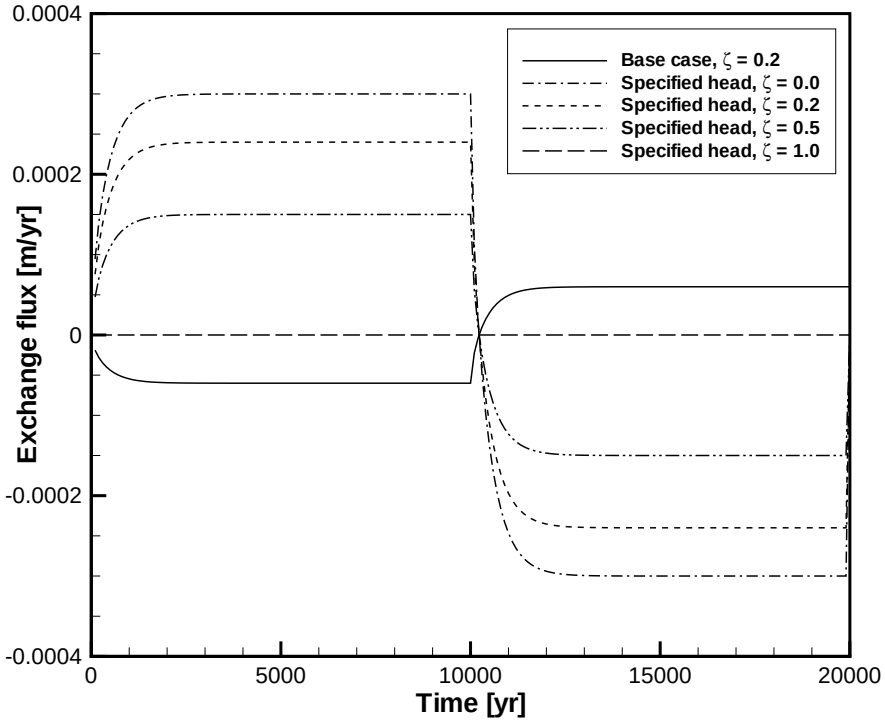

Figure 3.5: Exchange flux at the top of the column for different scenarios.

3.2.2 Brine Formation

In order to verify the implementation of the first-order source term in **HydroGeoSphere**, an analytical solution is derived for the case of steady-state flow along a horizontal column. The 1 m long column is open at both ends and a type-III (*i.e.*, Cauchy) boundary condition is specified at the inlet and a free exit boundary condition at the outlet. Mass is produced inside the column at a first-order rate, k_{mt}, of 86.4 d^{-1}. The porous medium is a well-sorted sand in which a constant average linear groundwater velocity of 1.0 m/d is specified. The longitudinal dispersion coefficient is 0.1 m, the diffusion coefficient of the solute is zero and the porosity of the sand, ϕ, equals 0.3. The initial concentration is zero and the maximum concentration is 0.3.

The one-dimensional governing equation describing the transport of a conservative

solute is:

$$\frac{\partial C}{\partial t} = -v\frac{\partial C}{\partial x} + \alpha_l v\frac{\partial^2 C}{\partial x^2} + \frac{k_{mt}}{\phi}\left(C_{\max} - C\right), \tag{3.56}$$

The boundary conditions for Eq. (3.56) are a third-type Cauchy at the inlet ($x = 0$) and a zero dispersive flux at $x = L$:

$$vc(0,t) - \alpha_L v\frac{\partial c(0,t)}{\partial x} = 0, \tag{3.57}$$

$$\frac{\partial c(L,t)}{\partial x} = 0, \tag{3.58}$$

$$c(x,0) = 0, \tag{3.59}$$

Eq. (3.56) was solved using Laplace transforms in conjunction with the commercial package Maple. The solution in Laplace space is complex and its inversion was performed numerically using the de Hoog *et al.* [1982] algorithm.

The analytical solution results at the outlet are shown in Figure 3.6 along with the numerical solution and it can be seen that the match is very good. The concentration rises quickly at the beginning and rapidly reaches the maximum fluid concentration of 0.3.

3.3 Other Processes

In the previous sections, processes described by differential equations were presented along with their implementation in the numerical model. There are also a series of processes and boundary conditions that were not previously included in **HydroGeoSphere** explicitly. In the following section, the manner in which processes such as subglacial meltwater infiltration, permafrost formation and isostasy are included in the model is described.

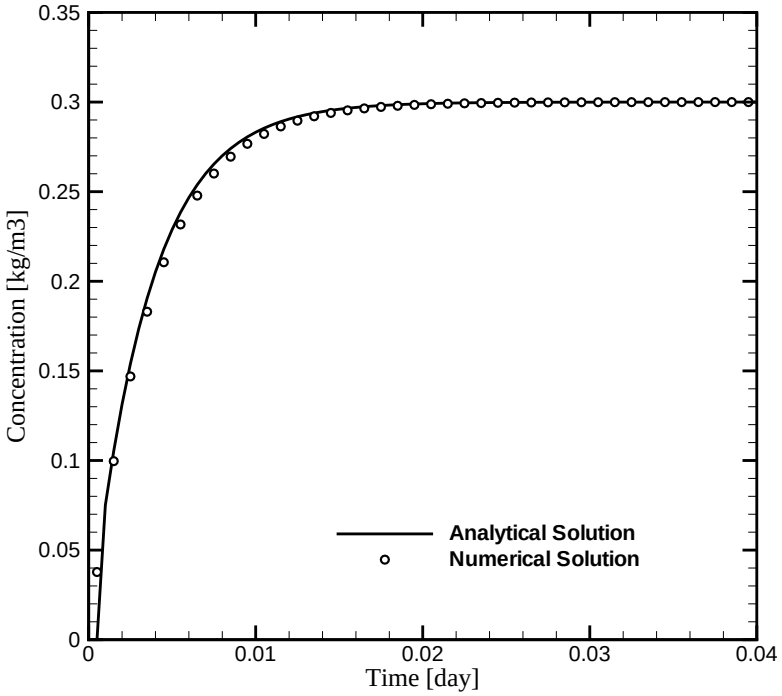

Figure 3.6: Concentration vs. time at the column outlet.

3.3.1 Subglacial Meltwater Infiltration

In some areas below the ice sheet, the basal ice is at the pressure melting point due to geothermal and frictional heating and there is production of meltwater [Paterson, 1994]. As discussed in Chapter 1, meltwater, depending on the subglacial conditions, will either flow as recharge to the groundwater flow system or discharge over the land surface between the ice-sheet sole and the rock surface.

The proportion of subglacial meltwater that can recharge and subsequently be stored in the subsurface is undoubtedly uncertain and is a question of much debate in the literature because of its relevance to many issues regarding current water usage, sustainability and anthropogenic activity. There are several approaches that have been used to calculate recharge rates during glaciation. Breemer *et al.* [2002], for example, specified a constant flux equal to the subglacial meltwater rate, but obtained

unrealistically high subsurface hydraulic heads in their model of the Michigan Lobe. They also examined a case having a high-permeability layer between the bedrock and the ice sheet. Only with the inclusion of a thin highly-permeable layer at the ice/bedrock interface, represented numerically by a highly transmissive fracture-type layer, could realistic subsurface heads be computed by the model. Therefore, the permeability of such a layer, and the spatio-temporal patterns of its permeability, becomes an issue on which little data exits that may be involved for verification. McIntosh *et al.* [2005] and Forsberg [1996] use a prescribed subsurface potentiometric head equal to the ice sheet thickness, expressed in terms of the equivalent freshwater head. This approach implies the assumption that the subglacial pressure never declines below the equivalent ice-sheet weight, which cannot be demonstrated. Piotrowski [1997a] also used a prescribed subsurface potentiometric head in his groundwater model at locations where the ice sheet covers the bedrock, but with the difference that it was inferred from paleo-porewater pressures estimated from the stress characteristics of the fine-grained sediments over-ridden by the ice sheet [Piotrowski and Kraus, 1997]. According to these proxy estimates, the potentiometric surface was on average equal to 72% of the ice thickness. This approach seems to lead to realistic infiltration rates, but is restricted to the relatively small regions under study for which paleo-porewater pressure data are available. Another approach was used by Svensson [1999], Boulton *et al.* [2001], Jaquet and Siegel [2003] and Jaquet and Siegel [2006] in which a specified meltwater rate is applied subglacially with the explicit inclusion of discrete subglacial tunnels (eskers) that will lower the water table due to their prescribed high hydraulic conductivity values. An arbitrary adjustment of the hydraulic conductivity of these tunnels can be made to achieve subglacial pressures slightly lower than the equivalent pressures induced by the ice-sheet thickness to yield realistic infiltration rates. The major drawback of this approach is that the

position, geometry and interconnectivity of the tunnels, and their hydraulic properties, must be known *a priori*; without this knowledge, it is clear that a stochastic, but geologically-constrained, probabilistic approach is needed.

The modelling approaches mentioned above to couple glaciations to groundwater flow are based on a number of assumptions or process-related simplifications, that are especially required if they are to be applied at the scale of the entire Canadian land mass. Here, we use a mix of time-dependant boundary conditions that are more natural and less constrained. For example, the manner in which subglacial meltwater enters the subsurface in the model is prescribed by a groundwater recharge flux that is dynamically constrained by the ice-sheet thickness from one time step to the next. That is, a specified groundwater recharge flux equal to the predicted subglacial meltwater rate is applied to the subsurface only as long as the hydraulic head at the glacier's bed is lower than the ice-equivalent freshwater head; otherwise the equivalent ice-sheet head at any node in the computational grid and its difference with the groundwater head at the same location is used to control the subsurface subglacial infiltration. The remainder of the meltwater is treated as direct overland runoff. The reasoning behind this treatment is that if the subsurface hydraulic head becomes higher than that equivalent to the ice-sheet weight, the ice sheet would float and become unstable. The numerical solution results are analyzed after each time step and if any of the surficial grid nodes exhibit a head higher than the equivalent ice weight, the time step is re-started with a head specified as the ice weight for those nodes. This approach allows the computation of the fraction of the meltwater that can naturally infiltrate into the subsurface, with the remainder assumed to participate in the surface runoff regime.

3.3.2 Permafrost Formation

Permafrost develops where ground temperatures remain below the pressure melting point. In regions where permafrost forms, the relative permeability of the porous medium is greatly reduced. These regions are believed to exist at the ice sheet margins [*e.g.*, Hughes, 1998; Boulton *et al.*, 1996; Boulton and de Marsily, 1997; King-Clayton *et al.*, 1995; Cutler *et al.*, 2000, among others]. Permafrost forms because of very low temperatures and can propagate through the subsurface to a depth of 1000 m. Where the frozen ground is covered by an ice sheet, the temperature of the subsurface will tend to warm because the ice sheet will act as a blanket and isolate the ground from the extreme surface temperatures. The lateral extent of the permafrost zone therefore migrates along the ice sheet margins.

As shown previously, Figure 2.5 illustrates the current extent of the permafrost zones across Canada as well as the permafrost thickness distribution. It can be seen that the continuous permafrost limit corresponds to a permafrost thickness of approximately 50 to 100 m. For this reason, the presence of permafrost is accounted for in the model when its thickness is greater than 70 m. At lesser depths, it is believed that the ice does not form a complete barrier for surface/subsurface water interaction but would decrease the bulk permeability.

Permafrost does not develop instantaneously; the freezing of water in the soil is instead a transient process. As water in the pores freezes, the permeability of the subsurface material to water is reduced and a relative permeability, as for unsaturated flow, can be defined as

$$k_{rw} = \frac{k\left(S_w\right)}{k_0} \tag{3.60}$$

where k_{rw} is the relative permeability to water, k_0 is the permeability of the fully liquid-water saturated materials, and $k\left(S_w\right)$ is the permeability at liquid water satu-

ration, S_w, with the remaining pore space filled with ice [Kleinberg and Griffin, 2005]. It is also the case that, because of capillary forces, water does not freeze completely and a thin film of liquid water covers the rock/soil grains even at low temperatures [Gascoyne, 2000; Vidstrand, 2003]. For this reason, neither S_w nor k_{rw} are allowed to reach zero.

The hydraulic conductivity of permafrost is the product of the fully-saturated hydraulic conductivity and the relative permeability to water: $K = K(S_w = 1)k_{rw}$. The water and ice saturations are not computed explicitly in **HydroGeoSphere**, but frozen or unfrozen states are provided by Tarasov and Peltier [2005b] for the entire glacial cycle across the landscape and with depth. For this reason, rather than specifying a permeability-water saturation relationship, which is not well understood and for which little data are available, the hydraulic conductivity is simply allowed to vary between its frozen and unfrozen states. For the frozen state, a low hydraulic conductivity is specified (*i.e.*, a 6 order of magnitude reduction) and, for the unfrozen state, the medium's default hydraulic conductivity value is used. Between these states, the permeability values are interpolated linearly between time steps so that they are progressively reduced or increased depending on the thermal regime. In order to include this progressive behavior in the model, time slices are selected (*i.e.*, 1000 yr), the affected finite elements are selected and an interpolated low hydraulic conductivity value is assigned. If, for the next specified time slice an element is no longer affected by permafrost, the assigned hydraulic conductivity value corresponds to a linear interpolation between the frost-free hydraulic conductivity value and the frozen value.

Permafrost formation also has a significant impact on the geochemistry of groundwater due to a salt rejection phenomenon. When the water cools, the salt solubility in the water diminishes and two phenomena can occur: chemical precipitation or

cryopeg formation [Vidstrand, 2003]. The cryopeg is a supercooled, saline liquid that forms in advance of the permafrost front as a consequence of salt rejection. This phenomenon is not included in the numerical model and the consequences will be discussed in the following chapters.

3.3.3 Isostasy

Isostasy is the state of equilibrium between the Earth's crust and the mantle. The weight of the ice sheet will cause the Earth's crust to deform and a new state of equilibrium will prevail. The deformation of the crust by the ice sheet is such that the Earth's surface elevation will be depressed below the ice sheet and raised near its margins.

The elevations of all the mesh nodes in each vertical grid column below the ice sheet are adjusted uniformly because the entire crust is depressed. Because the elevation changes from one time step to the next are relatively small compared to that which occurs over the entire glacial cycle, it is believed that this uniform coordinate adjustment of each vertical column of nodes will not produce significant fluid mass balance errors. On the other hand, the temporally and areally changing elevation component of the hydraulic head will have a significant transient impact on groundwater flow patterns.

Chapter 4

A Coupled Glacial and Groundwater Flow Model of the Canadian Landscape

"Do not fear mistakes. There are none."

Miles Davis

In this chapter, the numerical model described in Chapter 3 is used to simulate groundwater flow and solute transport during the Wisconsinian glaciation over the Canadian landscape. First, the details concerning the spatial and temporal discretization are presented followed by a description of the input data. The initial and boundary conditions are then discussed and the simulation results are presented in the next three chapters.

Table 4.1: Projection variables

Projection	Albers equal-area
Central parallel, ϕ_0	60° N
Central meridian, λ_0	107.5° W
Standard parallel 1, ϕ_1	40° N
Standard parallel 2, ϕ_2	70° N
Datum	Sphere
Earth's radius [km], R	6378.137

4.1 Discretization

The modelled region covers a large region of the Earth's surface (Figure 4.1) and because **HydroGeoSphere** does not support spherical coordinates, a Cartesian coordinate system was used. Map projection was used to transform geographical coordinate datasets into the Cartesian coordinate system. The Albers equal-area conical projection was used because it minimizes distortion and preserves area, which means that the land masses will appear exactly the same on a terrestrial globe and on a planar surface (see Appendix B for details about the projection). In the Albers equal-area conical projection, meridians are represented as straight lines radiating from the pole and parallels are concentric lines whose spacings are adjusted to maintain a constant areal scale. The distortion of the projected region is minimized using two standard parallels. The projected map has a Cartesian coordinate system with units of meters and centered on the projection origin. Table 4.1 shows the parameters used for the projection. As an example of the projection transformation, Figure 4.2 shows the map of the Canadian political boundaries in geographical coordinates followed by the same map projected using the Albers equal-area projection. The Cartesian coordinates shown in Figure 4.2b are those used in the model.

The limits of the model were chosen to capture the region affected by the last glaciation but are large enough such that the ice-sheet impact is negligible at the

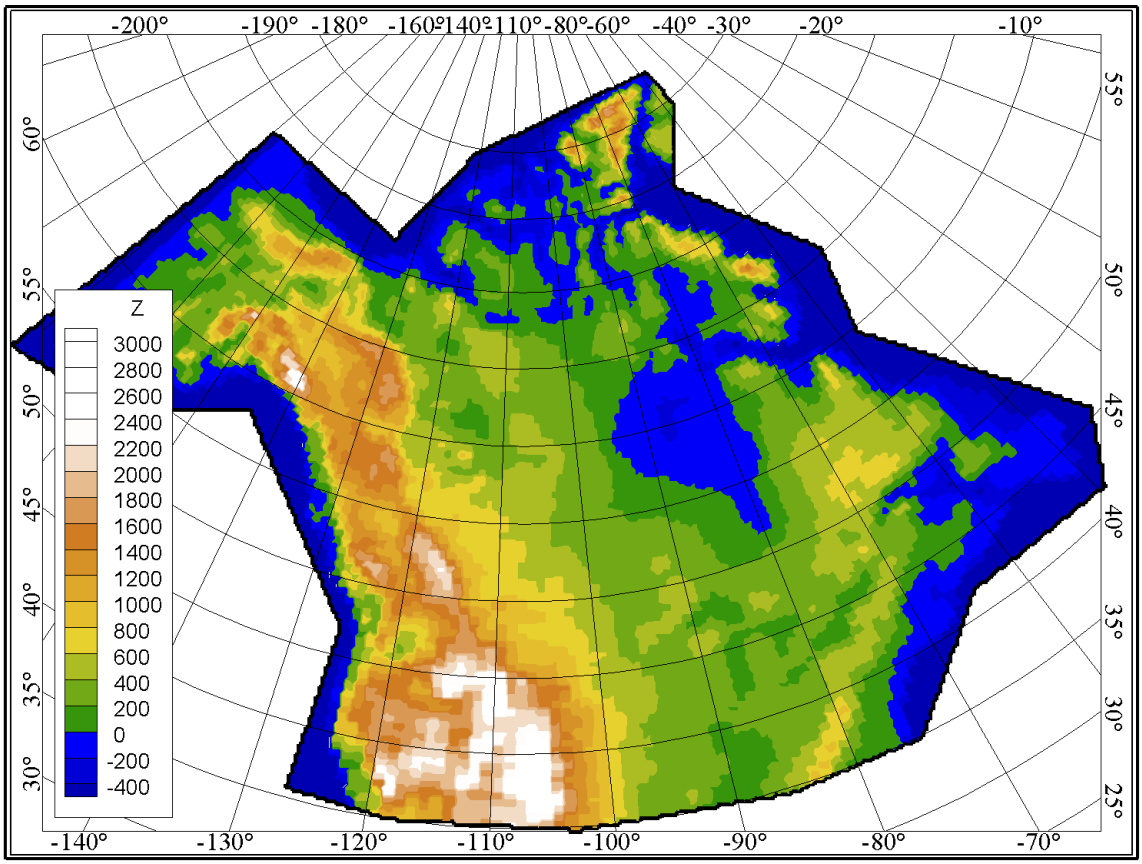

Figure 4.1: Limits of the numerical model. The geographic limits of the model are 172.5° W and 42.5° W on the western and eastern boundaries and 34.75° N and 84.75° N on the southern and northern boundaries. The color scale is the present-day surface elevation in meters.

margins of the model (Figure 4.1). Brick elements are used to discretize the model and are distributed along the principal Cartesian coordinate directions as shown in Figure 4.3. The areal cell sizes are uniform and have a dimension of 25 km × 25 km (625 km^2), which yields 40 496 elements and 41 094 nodes on a 2D horizontal slice. The extent of the model covers about 10 000 km × 6 000 km (Figure 4.3) with a total 2D area of 2.5 $\times 10^7$ km^2.

Along the z-axis, 10 layers cover the depth range between the surface elevation and an elevation of -10 km below present-day mean sea level. The elevations of the surfaces between the layers are located at constant depths for the first 1500 m; they

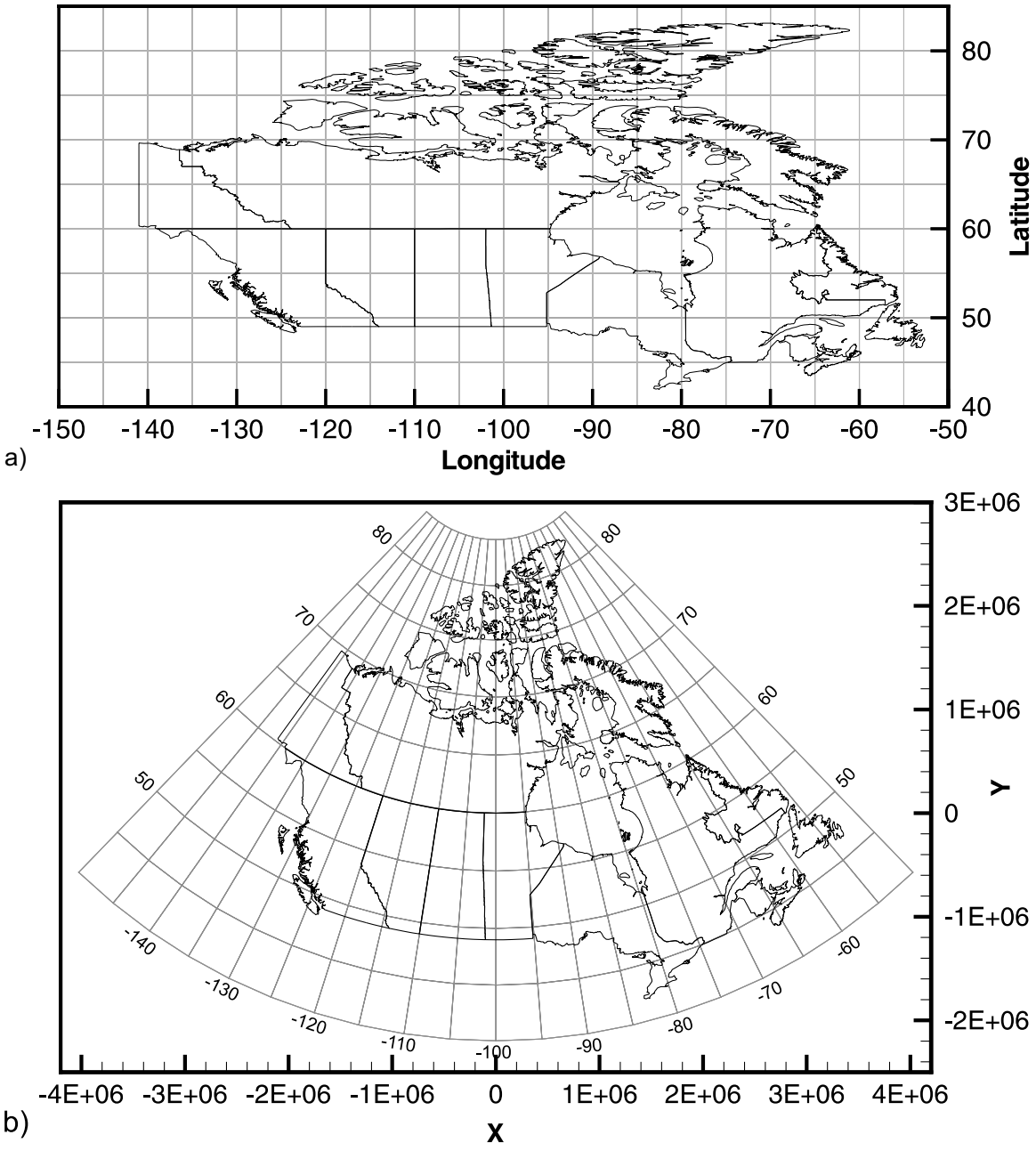

Figure 4.2: Map of Canada showing political boundaries in a) Geographical coordinates and b) Albers equal-area projection. The grid lines in geographical coordinates (a) are shown in the projected map (b) to show the transformation. Cartesian coordinates in meters are also shown in (b).

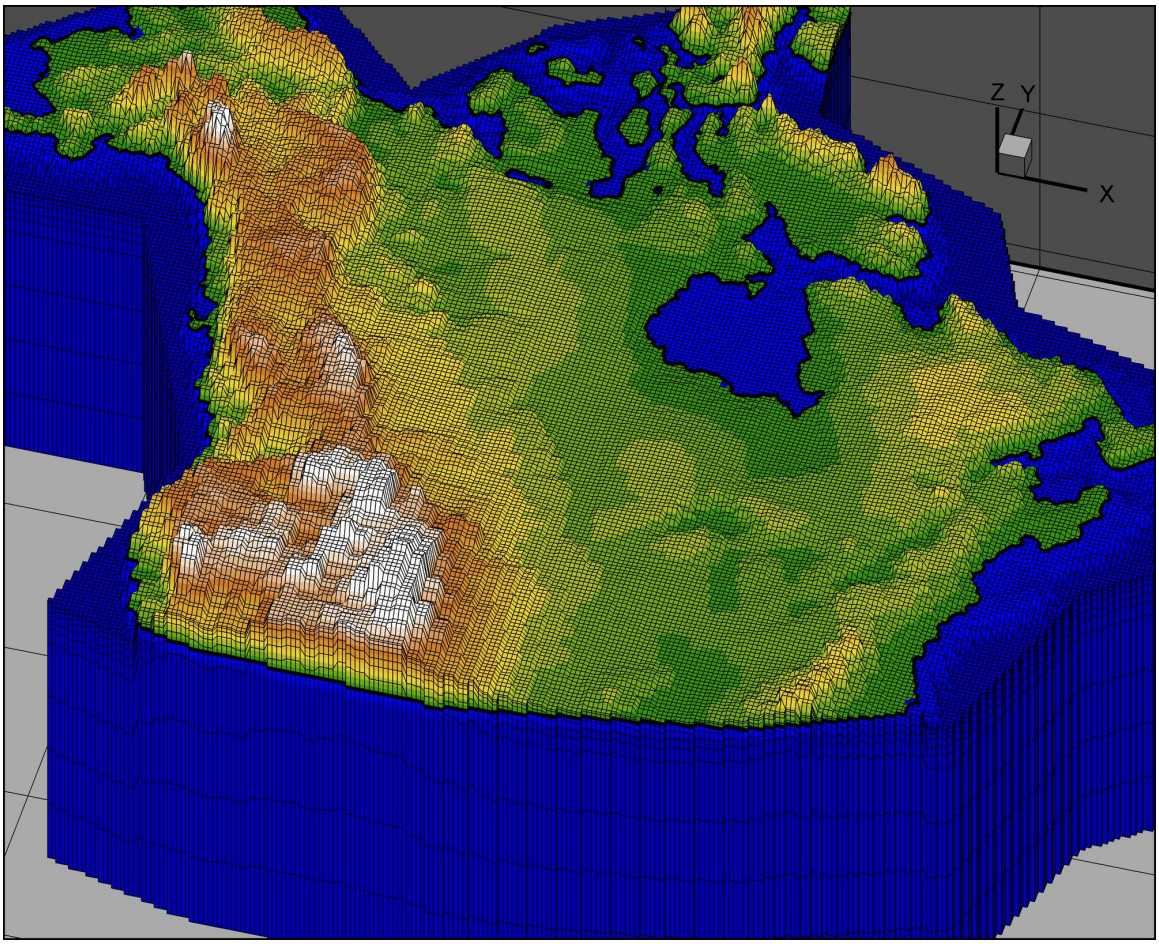

Figure 4.3: 3D mesh used for the simulation of the Wisconsinian glaciation. Elevation is displayed for the last interglacial period at -120 ka. Vertical exaggeration: 200×.

are located at -70, -200, -400, -700, -1000 and -1500 m below the surface elevation. Below 1500 m, the elevations of the remaining four layer surfaces are distributed uniformly to an elevation of -10 km. The total number of elements in the 3D mesh is 404 960 and the total number of nodes is 452 034.

The bedrock geology is simplified in the model into four major facies (Figure 4.4). Although this simplification is dramatic, computational constraints and the lack of systematic hydraulic measurements over the Canadian landscape limit the use of a highly-detailed geological model. The first facies is the Canadian Shield and the second includes the sedimentary basins. Average hydrogeological properties based on

a review of the hydrogeology of continental sedimentary basins are used. Most of the sedimentary basins are composed of similar types of rocks, which justifies the use of a single facies for all the sedimentary basins. The thickness of the sedimentary basins was obtained from Bassin *et al.* [2000] at a $2^\circ \times 2^\circ$ resolution which is an extension of the work by Mooney *et al.* [1998] at a $5^\circ \times 5^\circ$ resolution. Figure 4.5 gives an overview of the thicknesses of sedimentary basins over the globe, but does not distinguish between consolidated rocks or unconsolidated deposits. The third facies is referred to as the orogen and represents the Appalachian, Rockies, and Innuitian orogenic belts. The final facies is the oceanic crust which surrounds the North American continent. The simulations performed in this thesis span over the last 120 kyr, with a maximum time discretization of 100 yr.

4.2 Input Data

The surficial hydraulic properties of the four facies are provided in Table 4.2. The hydraulic conductivity and specific storage values are assigned based on the literature review presented in Section 2.1. Obtaining a representative value for hydraulic properties for such large regions is a daunting task for several reasons. The first is because most of the studies were performed in the context of water supply and that, generally, relatively shallow high-permeability aquifers are the focus by these studies. The reported hydraulic properties are therefore biased but the level of bias remains unknown. The second reason is because most of the hydrogeological studies are concentrated in populated regions, which is a very small portion of Canada. The last is because the hydraulic properties of the various regions are known to be highly heterogeneous, but data are lacking to describe the spatial patterns of the heterogeneity. The values used in the model are large-scale values and implicitly incorporate large

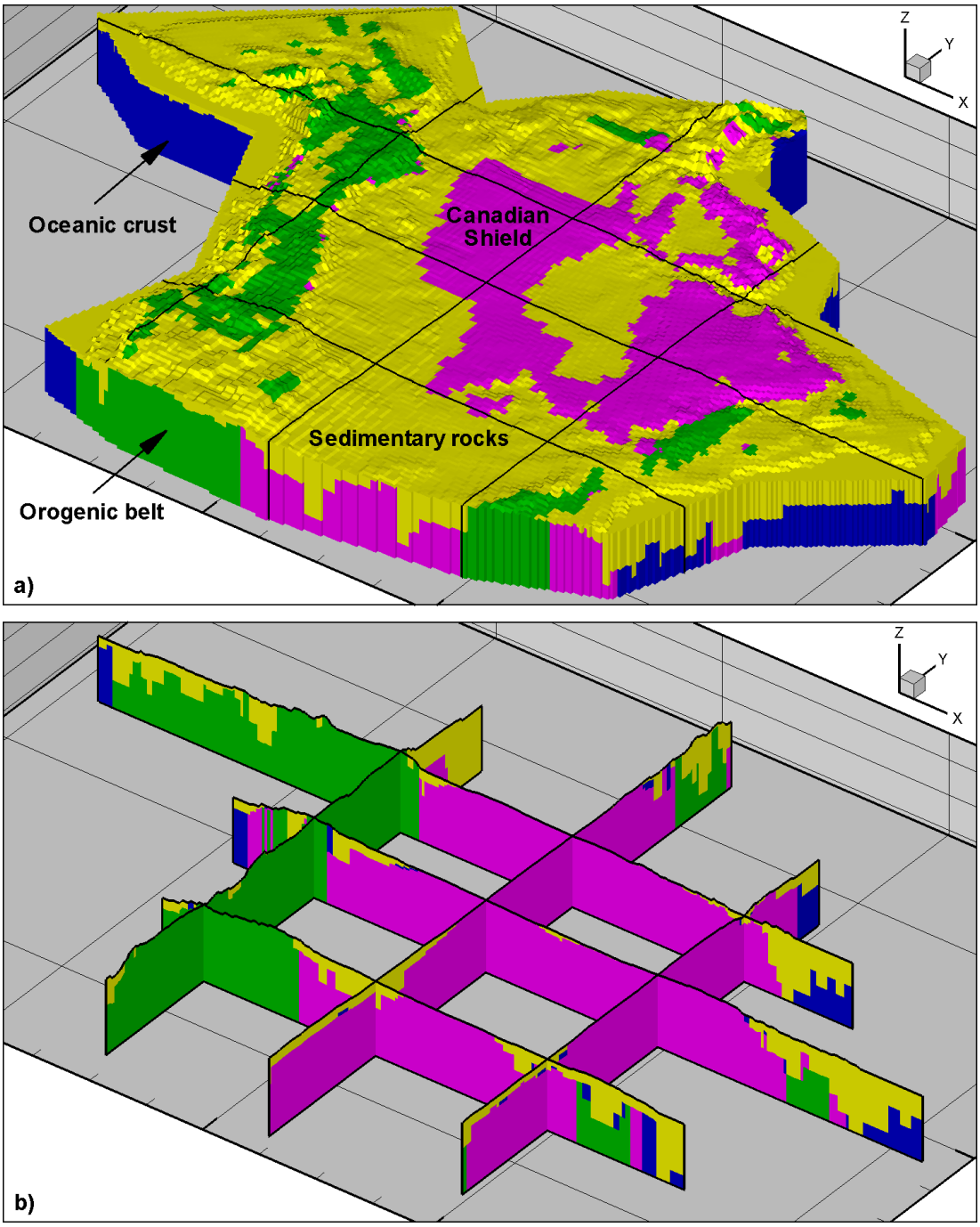

Figure 4.4: Simplified bedrock geology facies used in the numerical model shown a) for the entire simulation domain and b) in selected cross sections. Pink: Canadian Shield, dark green: Orogenic belts, dark blue: Oceanic crust and yellow: sedimentary rocks. Note that the blue spots of oceanic crust that appear in (b) and that are not on the margins of the model are software artefacts and don't appear in the numerical model. They are the result of the plotting software slice-extracting algorithm.

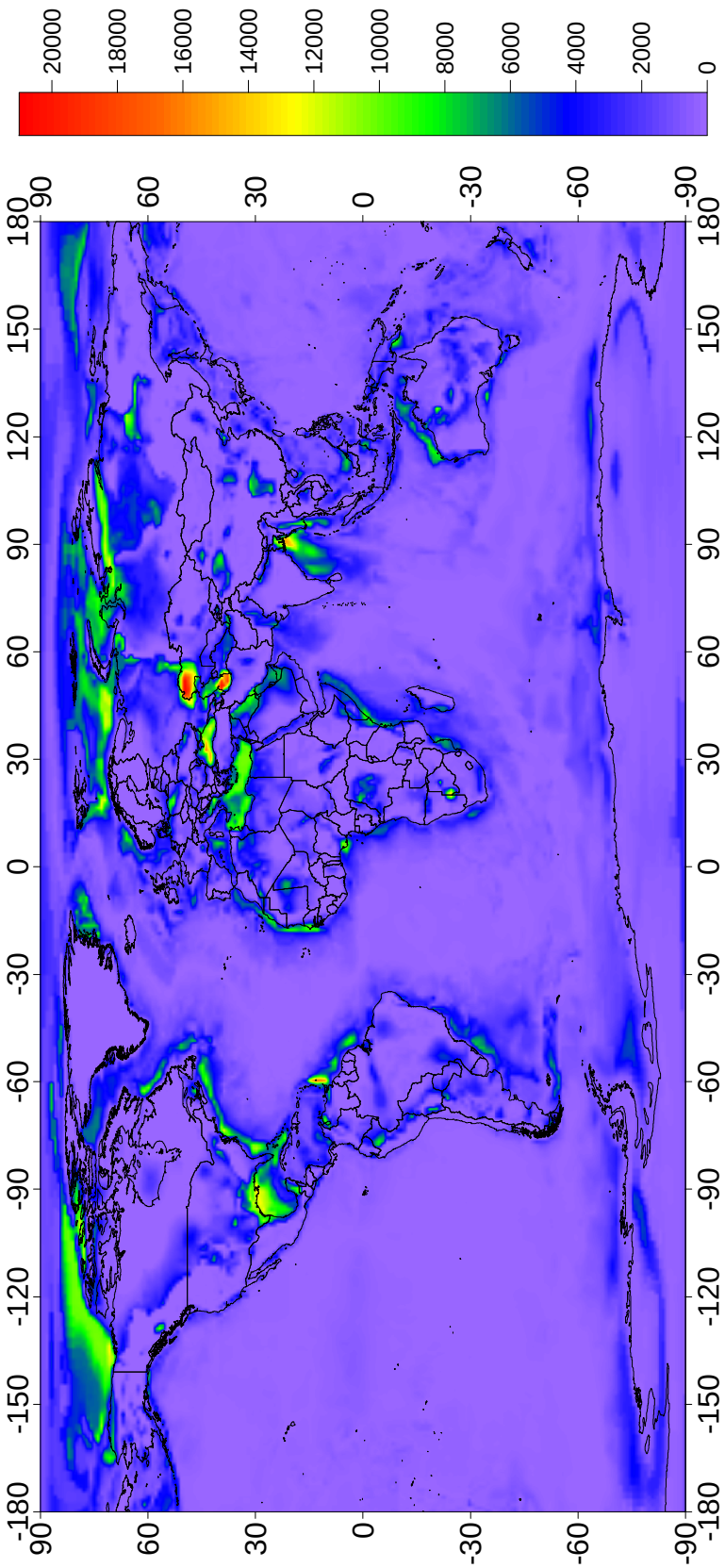

Figure 4.5: World sediment thickness map, in meters, on a $2° \times 2°$ geographic grid. Source: Bassin *et al.* [2000].

discontinuities such as fractures and faults that are likely more permeable than the host rock matrix.

Because hydraulic conductivity is expected to decrease with depth due to increasing effective stresses and temperature-dependent diagenetic and metamorphic processes [Ingebritsen and Sanford, 1998], surface hydraulic conductivity values decline with depth. As Farvolden *et al.* [1988] point out, the permeability reduction with depth is clearly notable over the first few hundred meters into the subsurface but deep-hole measurements suggest that, at large depths, local heterogeneities may be responsible for the permeability variations such that an unambiguous permeability reduction with depth is not discernable. Alternatives to direct measurements, such as results derived from models of heat and mass transport constrained by geothermal data and the progress of metamorphic reactions driven by fluid flow, have been used to infer crustal permeability values [Ingebritsen and Manning, 1999]. Values estimated from these modelling studies represent large-scale estimates of a large volume of rock and are less sensitive to the scale dependance of the smaller-scale punctual measurements such as those obtained from cores and borehole measurements [Manning and Ingebritsen, 1999]. Permeability estimates for large and moderate crustal depths ($>$ 5 km) have been defined mainly from studies of prograde metamorphic systems, and are therefore applicable to orogenic belts where the crust is being thickened and/or heated, while lower permeabilities may occur in more stable Shield environments [Ingebritsen and Manning, 1999]. A relationship between depth and permeability, k, is given by $\log k = -14 - 3.2 \log z$, where k is the permeability in meters squared and z is the depth in kilometers [Ingebritsen and Manning, 1999] (Figure 4.6). This relationship is logarithmic, such that the permeability would tend, impractically, to infinity at the surface elevation ($z = 0$, in Figure 4.6). Moreover, the relationship does not incorporate near-surface permeability data. Therefore, for the first few kilo-

Table 4.2: Bedrock hydraulic properties by facies.

	Sedimentary	Shield	Orogen	Oceanic crust
K_{xx} [m/yr]	60.0	30.0	3.0	0.1
K_{yy} [m/yr]	60.0	30.0	3.0	0.1
K_{zz} [m/yr]	60.0	30.0	3.0	0.1
Specific storage, S_s [m^{-1}]	5.0×10^{-5}	3.0×10^{-6}	1.0×10^{-5}	1.0×10^{-5}
Porosity, ϕ [-]	0.2	0.001	0.05	0.01
Loading efficiency, ζ, [-]	0.2	0.2	0.2	0.2
Longitudinal dispersivity, α_L, [m]	50 000	50 000	50 000	50 000
Transverse dispersivity, α_T, [m]	1 000	1 000	1 000	1 000
Transverse vertical dispersivity, α_V, [m]	1 000	1 000	1 000	1 000
Rock-water mass transfer constant, K_{mt}, [yr^{-1}]	2.3×10^{-7}	2.3×10^{-8}	2.3×10^{-8}	2.3×10^{-9}

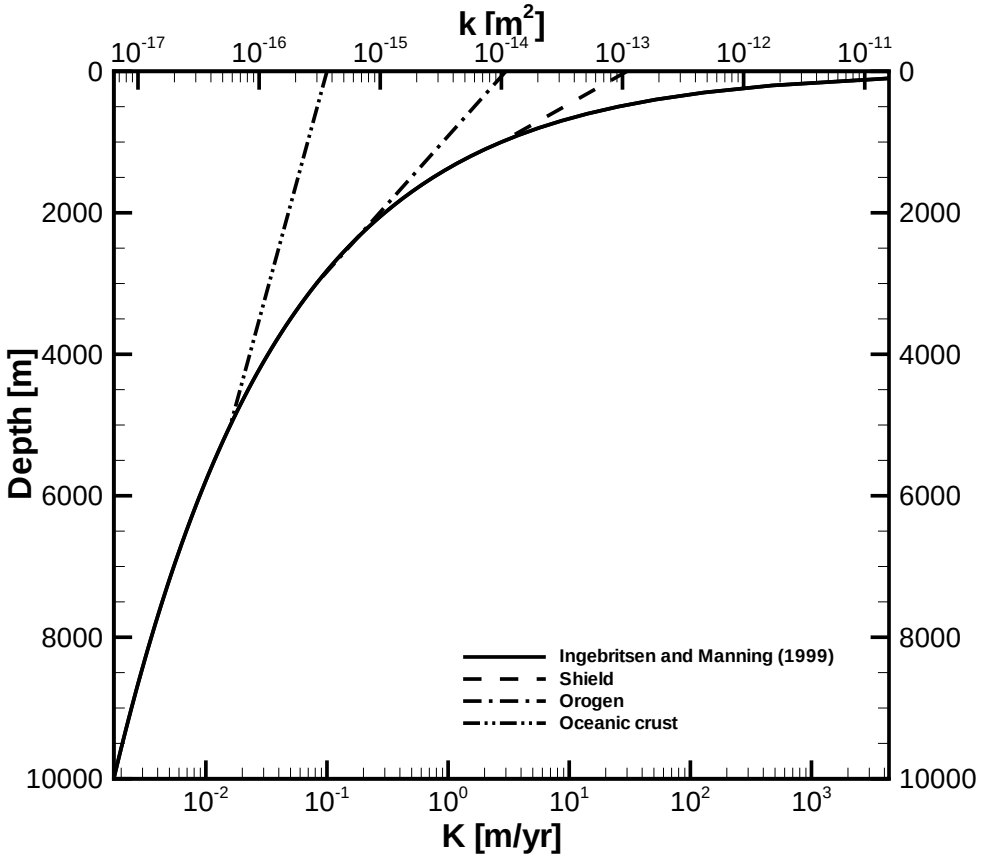

Figure 4.6: Hydraulic conductivity and permeability versus depth from Ingebritsen and Manning [1999] and for each rock facies. For illustrative purposes, permeability, k, and hydraulic conductivity, K, is arbitrarily based for water density and viscosity at values of 15°C.

meters of depth, a logarithmic reduction of the surface permeability is applied here so as to meet the Ingebritsen and Manning [1999] k-z relationship at a tangent angle (Figure 4.6). The hydraulic conductivity versus depth for each rock facies is given in Figure 4.6.

In sedimentary basins, available data suggests that the permeability distribution is more closely related to lithology than to depth. Therefore, no permeability versus depth relationship is applied to the sedimentary basins in the model. On the other hand, because of the coarseness of the model and complexity of the structure of

sedimentary basins, it is not possible to include lithologic details. Instead, an average permeability value is used.

It was indicated in Section 3.1 that the loading efficiency coefficient can be obtained from the elastic properties of rocks. There are no available data in the literature on values of the loading efficiency for each of the facies considered in this study. Furthermore, in low-porosity rocks, such as in the Canadian Shield, the loading efficiency is difficult to estimate because it is very sensitive to the difference between the bulk compressibility of the rock matrix and that of the solid grains, which is another unknown parameter [Provost *et al.*, 1998]. Therefore, the loading efficiency is treated as an independent and uncertain parameter in the model. For the base-case scenario, a loading efficiency of 0.2 is used, but will be varied to capture its influence on the simulation results.

Numerical dispersion is controlled by two factors: the grid spacing and the time step size. In one-dimension, the grid spacing is constrained by the grid Peclet criterion which is given by:

$$Pe = \frac{v\Delta x}{D} \leq 2 \tag{4.1}$$

where $v = q/\phi$ is the average pore-water velocity, D is the dispersion coefficient, and Δx is the grid spacing. The chosen longitudinal dispersivity respects this criterion. The use of large values in the horizontal and transverse dispersivities are also commensurate with the large size of the finite elements and sub-grid-scale heterogeneity that would promote mixing.

The time step is constrained by the grid Courant criterion which is given by:

$$Cr = \frac{v\Delta t}{\Delta x} \leq \frac{Pe}{2} \tag{4.2}$$

With a maximum value of $Pe = 2$, the Courant criterion yields the constraint:

$$\Delta t \leq \frac{\Delta x}{v} \tag{4.3}$$

Considering that the element sizes are on the order of kilometers in length and that the velocity does not exceed a few meters per year, the selected time step of 100 yr is small enough to satisfy the Courant criterion.

A series of spatially distributed time-varying datasets are derived from the glacial model and used as input. These include the surface elevation and sea-level changes, ice sheet thicknesses, subglacial melting rates, lake water depths and the permafrost distribution. Updated surface elevations, ice sheet thicknesses and lake water depths are applied every 1 kyr to the model with a linear interpolation between these periods in order to gradually vary the input and obtain a stable solution. The permafrost distribution, in the form of frozen elements, is also supplied every 1 kyr. In the model, the permafrost is assigned a very low hydraulic conductivity value (1.0×10^{-6} m/yr). Some authors [i.e. Breemer *et al.*, 2002] treat permafrost zones as impermeable while others reduce the permeability by two orders of magnitude [i.e Person *et al.*, 2003]. Boulton and de Marsily [1997] point out that there is no consensus about permafrost permeability values due to a paucity of information. The permafrost hydraulic conductivity is interpolated between the frost-free and the frozen value when the permafrost is forming or thawing as described in Section 3.3.2.

The dissolved solutes in the model consist of a series of anions and cations that are lumped together in the form of total dissolved solids (TDS). The maximum TDS concentration reported for groundwater is 265 000 mg/l and the fluid density at this concentration is 1 262.65 kg/m^3. In the model, the fluid density is allowed to vary linearly with the concentration. The solute and fluid properties are given in Table 4.3.

Table 4.3: Solute and fluid properties.

Effective diffusion coefficient, D^*[m^2/yr]	0.015
Fluid density at C_{max} [kg/m^3]	1 262.65
Viscosity, μ, [cp]	1.12
Maximum concentration, C_{max}, [mg/l]	265 000

4.3 Interglacial Conditions

There is little quantitative information available concerning the groundwater flow system during the last interglacial. It is, however, believed that the climate during this period was similar to the current climate. This implies that the last interglacial flow system would resemble the current one. It was mentioned earlier that the current groundwater flow system can be interpreted as a topographically-driven flow system that also reflects the current boundary (*i.e.*, climatic) conditions. By analogy, the last interglacial groundwater flow system is the result of the topography and climatic boundary conditions prevailing at that time which are provided by the University of Toronto Glacial Systems Model.

A pseudo steady-state simulation (*i.e.*, a transient simulation run until near steady-state) was performed using the climatic conditions of the last interglacial. The simulation was run for 1.2 Myr before a pseudo steady-state condition was achieved using time steps of 1 kyr. This simulation was designed to obtain the LIG flow field as well as the brine distribution. The hydraulic conductivities and the first-order brine-generation source term were adjusted until the simulated TDS profiles in the Canadian Shield reasonably fit the observed profile of Frape and Fritz [1987].

The simulated profiles of TDS are compared to the observed data for the Canadian Shield (Figure 4.7a) and for the Michigan Basin (Michigan, Illinois and Appalachian sedimentary basins) (Figure 4.7b). The list of observation points used to output the

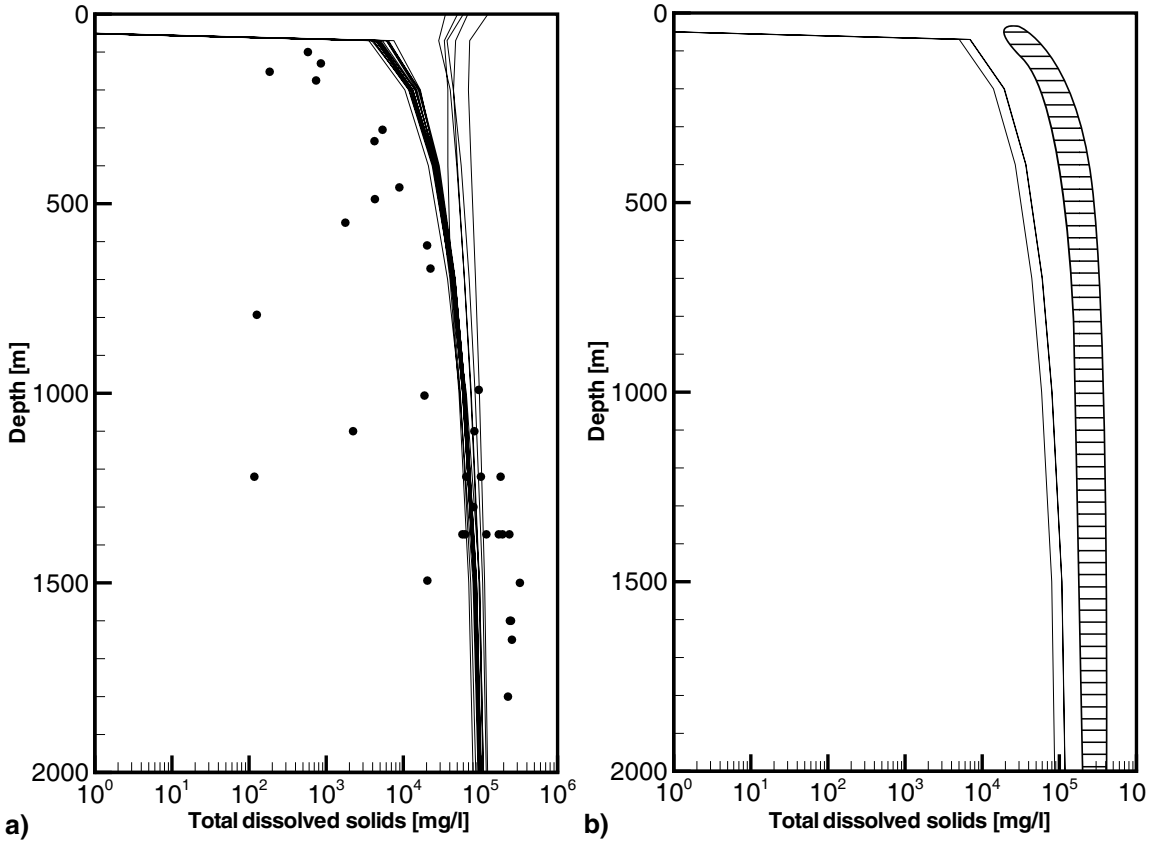

Figure 4.7: Simulated and observed total dissolved solids versus depth in a) the Canadian Shield and b) the Michigan Basin. Simulated TDS profiles are shown as continuous lines in both figures and the observed TDS profiles are shown as points for the Canadian Shield and as a hatched zone for the Michigan Basin.

simulated concentrations are shown in Table 4.4. Although there is some discrepancy in the fit, the trend captures the increase of salinity with depth that is observed across the basins and suggests that the properties of the model are adequate.

4.4 Boundary Conditions

The flow boundary conditions can be described separately for the subglacial and periglacial environments (Figure 4.8). For periglacial conditions, the assumption that the water table position equals the topographic surface elevation is made. In

Table 4.4: Coordinates of observation points in the Canadian Shield and the Michigan Basin.

Location	**Province**	**Longitude**	**Latitude**
Canadian Shield			
Yellowknife	NWT	-114.0	62.5
Great Bear Lake	NWT	-121.0	66.0
Great Slave Lake	NWT	-114.5	61.5
Baker Lake	NU	-96.0	64.3
Dubawnt Lake	NU	-101.5	63.0
Bathurst Inlet	NU	-108.0	66.7
Repulse Bay	NU	-86.0	67.0
Iqaluit	NU	-68.5	64.0
Nettiling Lake	NU	-70.7	66.5
Wollaston Lake	SK	-103.0	58.0
Thompson	MB	-98.8	55.7
URL lab.	MB	-96.0	50.5
Churchill	MB	-94.2	58.6
Lake Winnipeg	MB	-98.0	53.0
Lake Superior	ON	-87.0	47.0
Dryden	ON	-92.8	49.8
Timmins	ON	-81.4	48.4
Ottawa	ON	-75.8	45.5
Mistassini	PQ	-73.5	51.0
Labrador max. LGM	PQ	-72.0	53.0
Quebec	PQ	-71.4	46.8
Saguenay	PQ	-71.2	48.5
Shefferville	PQ	-67.0	54.0
Kuujjuaq	PQ	-68.5	58.0
Lac l'eau Claire	PQ	-74.5	56.0
Sept Iles	PQ	-66.2	50.3
Blanc Sablon	PQ	-57.0	51.5
Goose Bay	NF	-60.0	53.3
Churchill Falls	NF	-64.0	53.5
Grand Falls Windsor	NF	-60.0	53.5
Michigan Basin			
Michigan Basin	MI	-85.0	43.5
Illinois Basin	IL	-88.0	38.5
Appalachian Basin	WV	-82.0	38.0

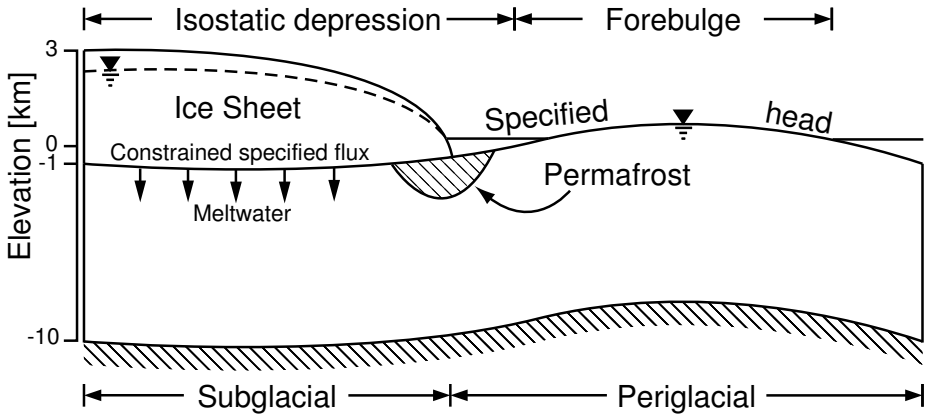

Figure 4.8: Boundary conditions showed in cross section along a ice flow line.

Canada, the water table is rarely deeper than a few meters to a few tens of meters and, given the scale of the model, it is believed that this is a reasonable assumption. The watertable position is therefore specified to equal the surface elevation for all the grid nodes not covered by ice. At some point, during the deglaciation period, the filling of surface depressions by glacial meltwater occurs and pro-glacial lakes such as lake Agassiz (-12 kyr to -8 kyr) form. In such cases, the nodes covered by lakes are assigned heads equal to the surface elevation plus the depth of the surface water bodies. The depths of these surface-water bodies at 100 yr time slices are available from the University of Toronto Glacial Systems Model output [Tarasov and Peltier, 2005a]. In some cases, the paleo-ocean level rose to levels different than a previous shore line such that a portion of the land surface was covered/uncovered by sea water. The nodes covered/uncovered by the ocean are assigned a head equal to the sea level at this time, which is given by the relative sea level curve (Figure 2.6).

The subglacial conditions are different depending on whether the ice sheet is cold or warm-based. For warm-based conditions, a constrained specified flux is applied as described in Section 3.3.1. This allows the infiltration of subglacial meltwater into the subsurface in a natural way and allows the computation of the infiltrated versus runoff part of the subglacial meltwater. This also prevents the building of

unreasonably high subglacial heads which happens if the total subglacial meltwater flux is applied as infiltration without any constraint. The constraint on the subglacial meltwater flux is equal to the equivalent freshwater head of the ice, which is given by $h_s + \rho_{ice} \cdot (h_{ice} - h_s)$, where $\rho_{ice} = 0.92$, is the relative density of ice, h_{ice} is the ice surface elevation and h_s is the elevation of the land surface. For cold-based conditions, the same constraint is applied, but the subglacial meltwater flux is specified to equal zero. This allows the discharge of groundwater without exceeding the ice sheet equivalent freshwater head.

Around the coastal margins, the equivalent freshwater heads are specified as time variable values, reflecting the change in relative sea level as depicted in Figure 2.6.

The solute boundary conditions on the surface are a specified concentration equal to zero when water is entering the model, either at specified water flux or specified head nodes. A zero concentration gradient is assumed at the outlet nodes such that the solute mass can freely advect out of the domain at the resident groundwater concentration. It is believed that over the last 120 ka, the concentration will not change at depth of 10 km below current mean sea level. Therefore, a first-type boundary condition, c/c_{max} equal to 1.0, is specified at the bottom of the system. Table 4.5 summarizes the surface boundary conditions for flow and transport. Boundary conditions for the groundwater age calculations will be described in the next chapters.

The boundary conditions are updated in the model at every 1 kyr. For the specified head values, linear interpolation between time steps is used to obtain a smooth input function. The constraints on the specified flux are also linearly interpolated between the 1 kyr time slices. Finally, Picard iteration is used to solve the non-linear flow equation due to the variable density of the groundwater.

Simulations were run on a IBM eCluster 1350 on an single 3.6 GHz processor with 8 GB of RAM. The average simulation time for the base case scenario is about 6 days.

Table 4.5: Summary of flow and transport surface boundary conditions during the glacial-cycle simulation. Transport boundary conditions are given for the two variables: Total dissolved solids (TDS) and mean groundwater age. The number in parenthesis indicate the value of the boundary condition.

	Subglacial	**Periglacial**
Flow	Mixed Dirichlet-Neumann	Dirichlet
Transport		
TDS (value)	Dirichlet (0.0)	Dirichlet (0.0)
Age (value)	Dirichlet (0.0)	Dirichlet (0.0)

Chapter 5

Surface/Subsurface Water Interactions During the Wisconsinian Glaciation

"Every scientific truth goes through three states: first, people say it conflicts with the Bible; next, they say it has been discovered before; lastly, they say they always believed it."

Louis Agassiz

As discussed in Section 3.3.1, meltwater interactions with the subsurface on the subglacial environment is complex. Questions addressing the amount of water that infiltrates into the subsurface are critical to explain the current geochemical composition of groundwater, but spatial distribution and the timing of the exchange fluxes in relation to the ice sheet development/dismantling are equally critical. In this chapter, the surface/subsurface water interaction for the base case scenario described in Chapter 4 will be investigated. Then, the permafrost and ice-sheet loading will be deactivated and modified successively to show their respective importance over a

glacial-cycle simulation. A brief summary will follow to present the salient conclusions of this chapter.

5.1 Base-Case Scenario

Figure 5.1 shows the calculated surface/subsurface water exchange fluxes in the subglacial environment during the glaciation period. Along with the total flux crossing the ground surface, the volumetric infiltration and exfiltration fluxes are also shown. The volumetric fluxes shown in Figure 5.1a are large because they are integrated values over the entire subglacial environment. When expressed as a flux (Figure 5.1b), the infiltration ranges between 0 and 6 mm/yr with an average of about 2.5 mm/yr. The exfiltration (*i.e.*, groundwater discharge) flux can reach values up to about 12 mm/yr with an average of 2.0 mm/yr. The exfiltrating fluxes reach higher values than infiltration because the area of the exfiltrating portion of the subglacial environment is much smaller than the infiltration portion.

The GSM-predicted total surface area of the glacial ice is shown in Figure 5.1a and can be used as an indicator of ice sheet progression or regression; an increase in the total surface area indicates ice sheet progression over the land surface and a decrease in surface area indicates that the ice sheet is regressing. It can be seen from Figure 5.1a that there were three major glacial advances/regressions during the Wisconsinian glaciation and that maxima in the ice volumes occured at about -105, -60 and -21 kyr (GM1, GM2 and GM3 in Figure 5.1a). It can be seen that, in the subglacial environment, most of the infiltration of the meltwater into the subsurface occurs when the ice sheet is growing. Conversely, groundwater mainly exfiltrates during ice-sheet regression. Because of the high pressures at the bed of the ice sheet, meltwater is forced downward into the subsurface during ice sheet advance and, when

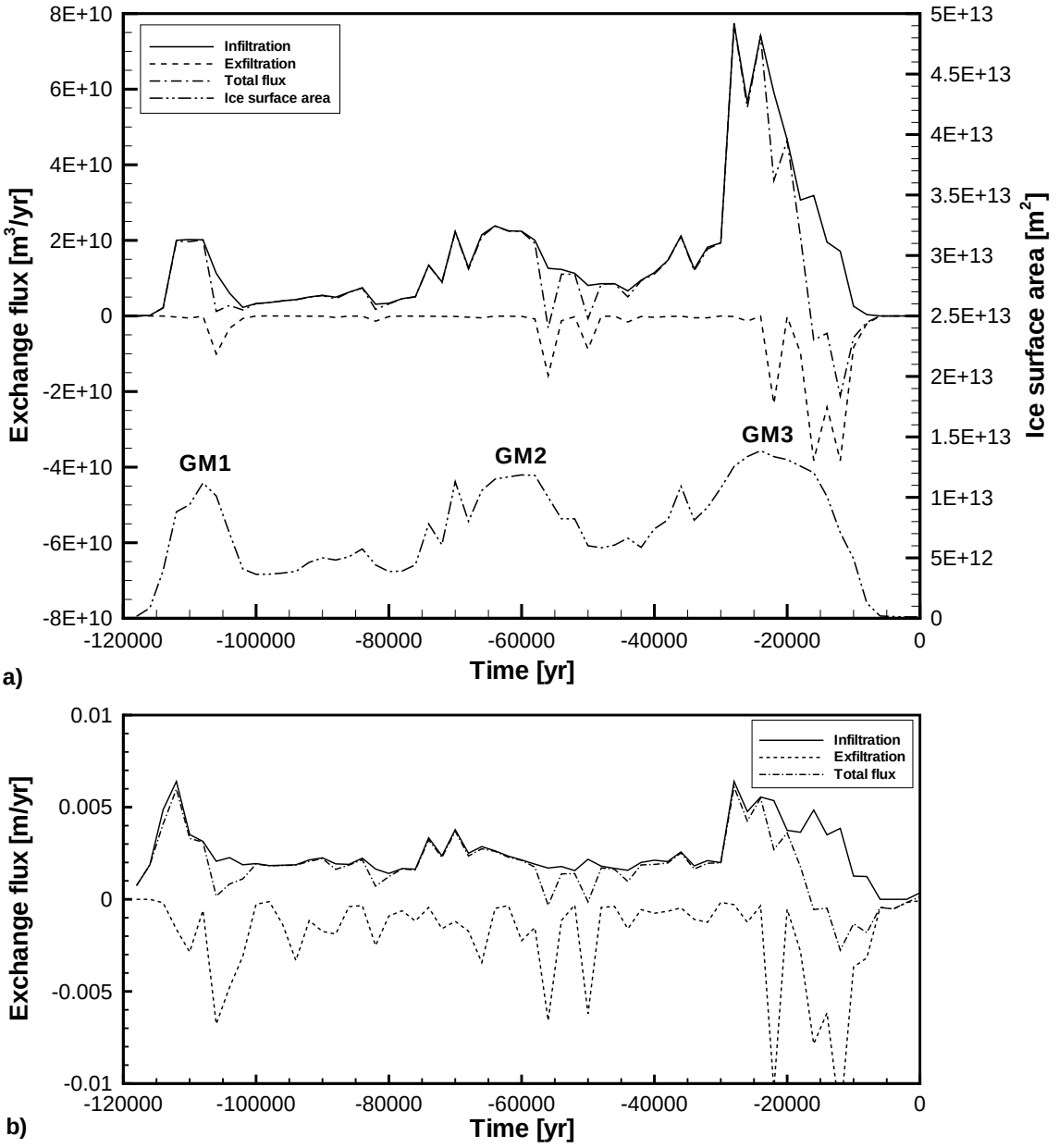

Figure 5.1: Subglacial exchange flux during the glacial cycle. a) Exchange flux in m^3/yr. The curves represent the integration of the flux over the entire subglacial environment. The ice sheet surface area is also shown with the timing of the glacial maxima GM1, GM2 and GM3. b) Exchange flux in m/yr.

the ice-sheet is regressing, the pressure in the subsurface becomes higher than the basal meltwater pressure and groundwater exfiltrates.

The relationship between the exchange flux regime and the ice sheet progression can also be observed in Figure 5.2a, 5.2c and 5.2e where the areal pattern of the surface/subsurface water exchange flux is shown over the entire simulation domain for three time slices. The slices are chosen to capture the portion during ice-sheet during progression (-30 kyr), at the end of the ice-sheet progression (at LGM, -20 kyr) and during ice-sheet regression (-14 kyr). Again, it can be seen that infiltration dominates during ice-sheet progression while exfiltration dominates during ice-sheet regression, although both regimes are always active.

The mixed boundary condition used at the subglacial faces of the upper elements in the mesh allows computation of the ratio of the total meltwater that is infiltrating the subsurface to the total meltwater production. The integration of the infiltration ratio over the entire subglacial environment shows that the infiltration ratio oscillates between 15% and 100%, with an average of about 43%, that was obtained by integrating the infiltration ratio curve (Figure 5.3). This indicates that a large fraction of the meltwater actually enters the subsurface. The infiltration ratio reaches its lowest value, less than 15%, during the last glacial advance, which is also the period that produced the largest amount of meltwater. It can be seen that the infiltration diminishes shortly after the initiation of the three glacial advances GM1, GM2 and GM3.

Throughout the glacial cycle, only a fraction of the subglacial meltwater infiltrates into the subsurface, which means there is an excess of meltwater. Because the rock permeability is not sufficient to drain all of the meltwater, subglacial pressures will buildup until the pressure reaches the ice weight. At this point, pressures will remain at the ice weight pressure until the meltwater production diminishes. During this

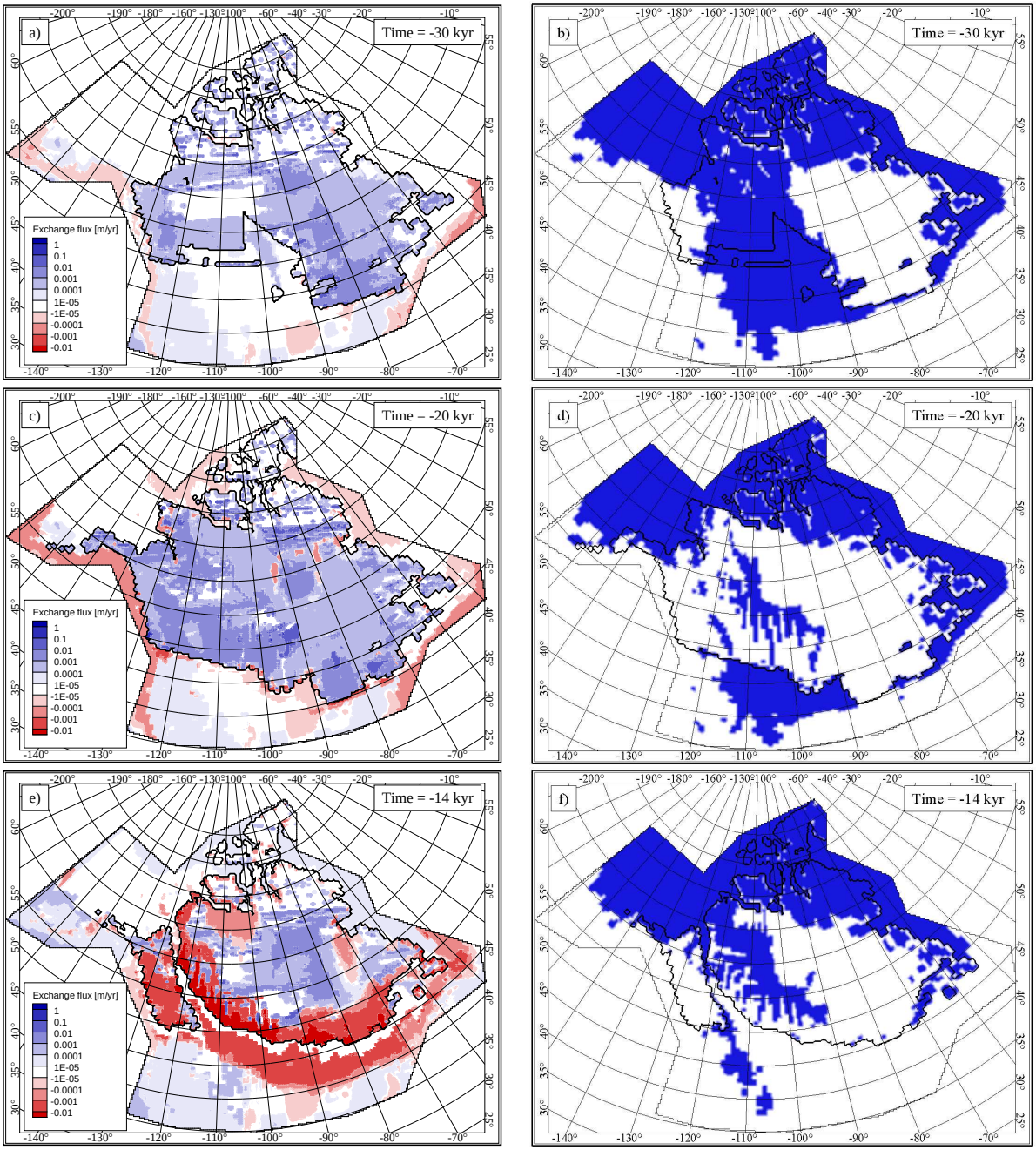

Figure 5.2: Simulated surface/subsurface water exchange flux and surface permafrost distribution at -30 kyr (a, b), -20 kyr (c, d) and -14 kyr (e, f). The surface permafrost distribution is represented in blue indicating the surface finite elements affected by permafrost. The black line indicates the ice-sheet limits.

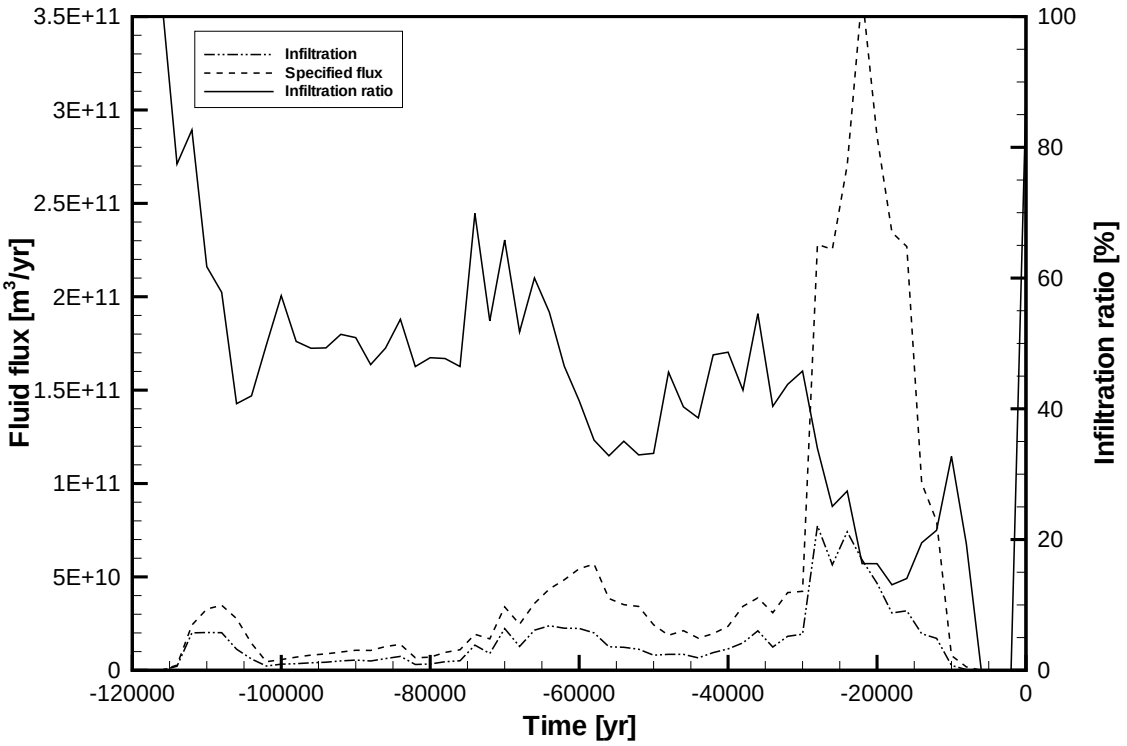

Figure 5.3: Total subglacial specified meltwater flux, subglacial infiltration flux and infiltration ratio versus time throughout the last glacial cycle.

period, the excess meltwater is assumed to drain out of the model through a series of subglacial conduits. The infiltration process at the ice-weight pressure then becomes a function of the ice thickness and is no longer a function of the meltwater production. Therefore, the ice sheet thickness plays a key role in the infiltration process.

The infiltration rate into the subsurface is expected to be different for sedimentary rocks than for Shield rocks because the hydraulic conductivity of the sedimentary rocks is higher. The calculation of the infiltration rate for both type of rocks for the whole glacial cycle is shown in Figure 5.4. It can be seen that the infiltration rates are higher for the sedimentary rocks that for the Shield rocks, and that the difference is even larger during the glacial advances.

The surface/subsurface water interaction in the periglacial environment has some

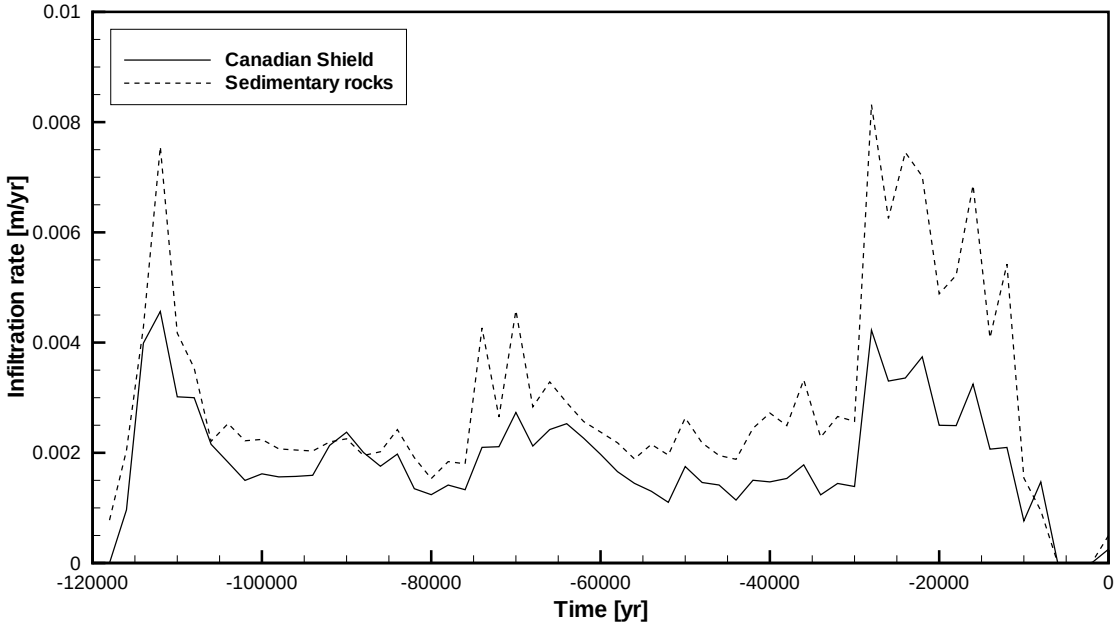

Figure 5.4: Mean subglacial infiltration rates for the sedimentary rocks and Canadian Shield facies.

similarity to that in the subglacial environment; most of the exchange flux is dominated by exfiltration during ice sheet regression, as shown by the volumetric exchange fluxes presented in Figure 5.5a and illustrated in a two-dimensional map of the exchange flux during ice sheet regression (Figure 5.2e). This situation occurs because the retreat of the ice sheet reveals a fringe of subsurface materials that are under ice-sheet pressure and experiencing meltwater infiltration. Similar to the subglacial environment, when the ice sheet is retreating, the hydraulic gradient is reversed and groundwater exfiltrates across land surface or into large proglacial lakes. At the ice margin, a large hydraulic gradient develops between the ice-covered region and the periglacial zone. In absence of permafrost or for a thin frozen depth, this large hydraulic gradient will increase the exfiltration flux at the margin.

The periglacial infiltration flux is quite low over the time span of the simulation (Figure 5.5a) and represents infiltration at ice-free high elevation regions over the

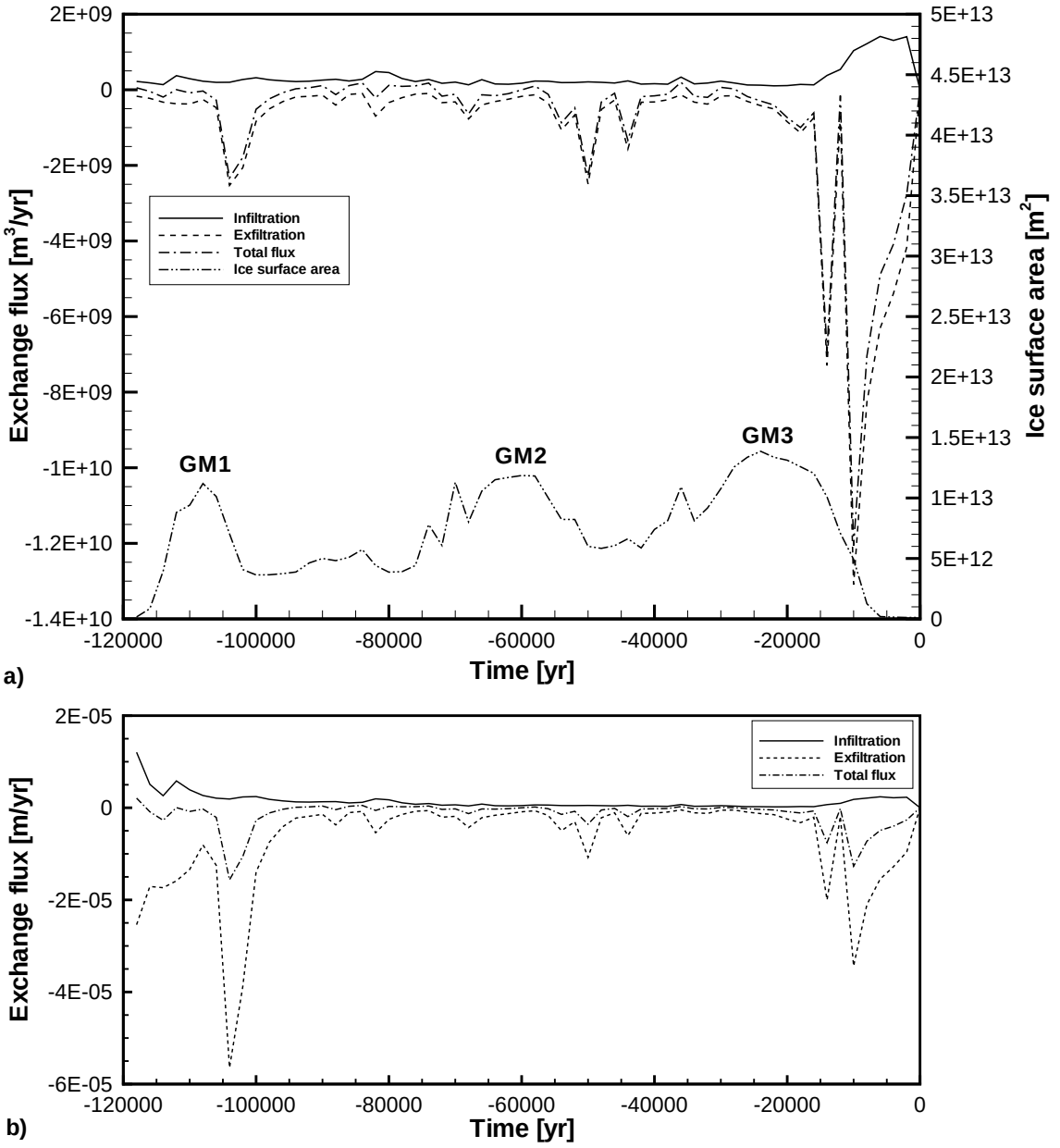

Figure 5.5: Periglacial exchange flux during the glacial cycle. a) Exchange flux in m^3/yr. The curves represent the integration of the flux all over the periglacial environment. The ice sheet surface area is also shown with indications for glacial maximums GM1, GM2 and GM3. b) Exchange flux in m/yr; the volumetric fluxes are divided by their respective surface area.

Canadian landscape. After the last glacial maximum, the infiltration flux in the periglacial environment rises suddenly. Rapid filling of proglacial lakes may explain this infiltration augmentation. Increasing hydraulic heads due to the development of the proglacial lakes in regions of low topographic elevation have a large impact on the hydraulic gradient.

It can be seen from Figure 5.5b that the periglacial exchange flux is much lower than the subglacial exchange flux (Figure 5.1b); its magnitude is about three orders lower than that in the subglacial environment. During an interglacial period, the infiltration flux is about 0.03 mm/yr which is of the same order of magnitude as the infiltration flux in the periglacial environment. Except for the large exfiltration fluxes, the periglacial exchange fluxes during the glacial cycle are similar to those during the interglacial and the values are quite low. The infiltration into the subsurface during a glacial cycle can be three orders of magnitude higher than during interglacial periods, such as the current one.

The rates of groundwater recharge, over the Canadian Shield are not well documented. A compilation from Heath [1988] gives a range between 10-300 mm/yr, which seems quite high. Thorne [2004], based on a detailed water budget in three small catchments located near the Underground Research Laboratory in Manitoba, reports a recharge rate of about 2 mm/yr. This is probably a more representative value for recharge into exposed Shield rocks.

5.2 Exchange Flux Sensitivity to the Loading Efficiency Parameter

During the literature review, it was found that most of the studies that couple glaciations to groundwater flow models do not account for the ice sheet loading. An ice

sheet of a few kilometers thickness has a weight sufficient to depress the earth's crust by about 1 km, and it is unlikely that it would not have an impact on subsurface pore pressures. Therefore, the impact of the ice sheet loading on the surface/subsurface water exchange fluxes will be demonstrated by varying the value of the loading efficiency parameter, ζ, appearing on Eq. 3.36. For this purpose, the value used in the base-case scenario was modified while the other properties and boundary conditions remained the same.

It was shown in Section 3.2 that the primary effect of surface loading is to decrease the porespace, which in turn increases the pore pressure. Using a simple 1D example, it was demonstrated that under subglacial meltwater conditions, the effect of surface loading is to drive subglacial meltwater into the subsurface during ice sheet formation and that the opposite occurs when the ice sheet retreats.

Figure 5.6 demonstrates the effect of varying the loading efficiency parameter on the areally-averaged subglacial infiltration flux. The temporal change in the subglacial infiltration flux, expressed as a volumetric rate, is shown over the glacial period for loading efficiency values of 0.0, 0.2 and 1.0. It can be seen that the subglacial infiltration is maximum when the loading efficiency is zero and it decreases when the loading efficiency increases. This trend is similar to that observed for the 1D verification example provided earlier in Section 3.2 and is a consequence of the interaction between the subglacial boundary conditions and the loading efficiency.

Inspecting Figure 5.6, it can be noted that the change in the subglacial infiltration rate is quite large for $\zeta = 1.0$ compared to that of the base case ($\zeta = 0.2$), especially during LGM when the calculated infiltration is much less with $\zeta = 1.0$. This is because the entire ice load is transferred to the subsurface fluid for $\zeta = 1.0$, thus rapidly increasing pore pressures at all depths which in turn greatly reduces the vertical hydraulic gradient.

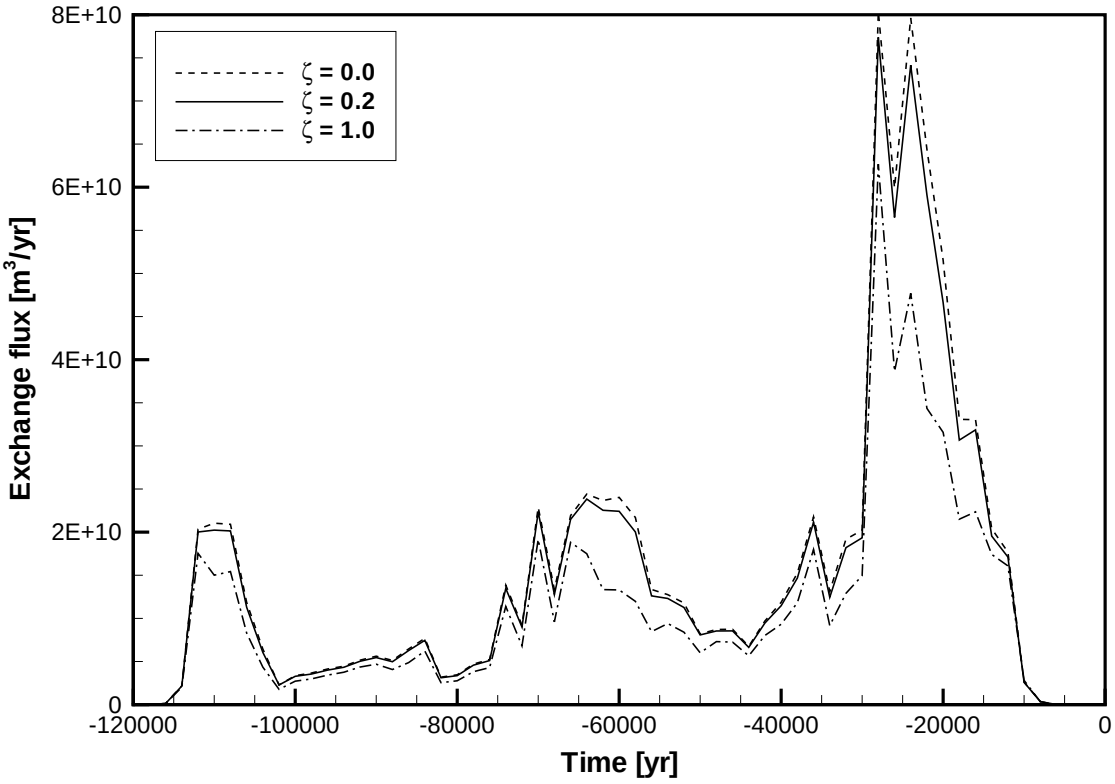

Figure 5.6: Subglacial infiltration flux for the base-case scenario ($\zeta = 0.2$) and for cases where $\zeta = 0.0$ and $\zeta = 1.0$.

5.3 Permafrost Impact on Surface/Subsurface Interaction

Permafrost evolution during a glacial cycle is another phenomena where large uncertainties exist regarding its distribution and timing. The role of permafrost on groundwater flow is not fully understood, although it is generally accepted that it will act as a flow barrier. In order to capture the impact of permafrost on the infiltration of subglacial meltwater, the base-case simulation results are examined and will be compared to a case where the presence of permafrost is ignored.

Figure 5.7 integrates through time the subglacial area that is covered by permafrost, the total subglacial area, as well as the subglacial area where an exchange of surface/subsurface water occurs (*i.e.*, either meltwater infiltration or groundwater discharge). By inspection of Figure 5.7, it is evident that large parts of the subglacial environment are inactive in terms of surface/subsurface water interactions because the exchange flux surface area is smaller than the total subglacial surface area over the entire glacial cycle. This can be explained by examining the surficial permafrost distributions shown in Figures 5.2b, 5.2d and 5.2f. and comparing the patterns with those of the exchange fluxes given in Figures 5.2a, 5.2c and 5.2e. The zones where the exchange flux is low or nonexistent correspond quite well with the permafrost regions. On the other hand, some infiltration/exfiltration does occur at some permafrost locations. This becomes clear upon close inspection of the results given in Figure 5.7. The sum of the areas where surface/subsurface water interaction occurs and the frozen ground areas should match the total subglacial ice area if no water exchange flux occurs in permafrost regions; however it can be seen that the sum of the exchange flux and permafrost areas is larger than the total ice area. This indicates that some regions covered by permafrost are experiencing some infiltration or exfiltration. This

can partly be explained by the presence of regions where the permafrost is thin such that a water exchange flux can occur despite these regions having a low hydraulic conductivity. Also, the effect of the ice loading/unloading on the surface causes the geologic materials, frozen or not, to expand and contract, which in turn forces water into or out of the porous medium (recognizing that the assumed permeability of the permafrost is non-zero, but small). Finally, it should be noted that permeabilities are linearly interpolated between their frozen and unfrozen values through each 1-kyr period because the permafrost distribution is updated at this frequency, yet the flow model use 100 yr time steps.

Nevertheless, there are large parts of the subglacial environment that are prevented from water interaction with the subsurface due to presence of frozen ground. Frozen materials prevent much of the surface/subsurface water interactions from ocurring in both the subglacial and periglacial environments. The distribution and timing of the permafrost are therefore critical to capture the impact on groundwater flow during a glaciation period.

The base-case scenario was therefore modified by removing the influence of permafrost formation in the model by forcing the permeabilities of the rocks to maintain their unfrozen values. In the subglacial environment, it appears that the neglect of permafrost does not significantly affect the computed values of the infiltration and exfiltration fluxes (Figure 5.8a). Subglacial meltwater is produced mainly in warm-based regions below the ice sheet where there is no permafrost and unfrozen-state permeabilities are employed. Rarely is meltwater produced in cold-based regions where permafrost exists below the ice sheet and therefore the assigned permeabilities will have little influence on the overall results in these areas because, even if the permafrost is removed, there is little or no subglacial meltwater available to infiltrate.

On the other hand, the removal of the permafrost from the periglacial environ-

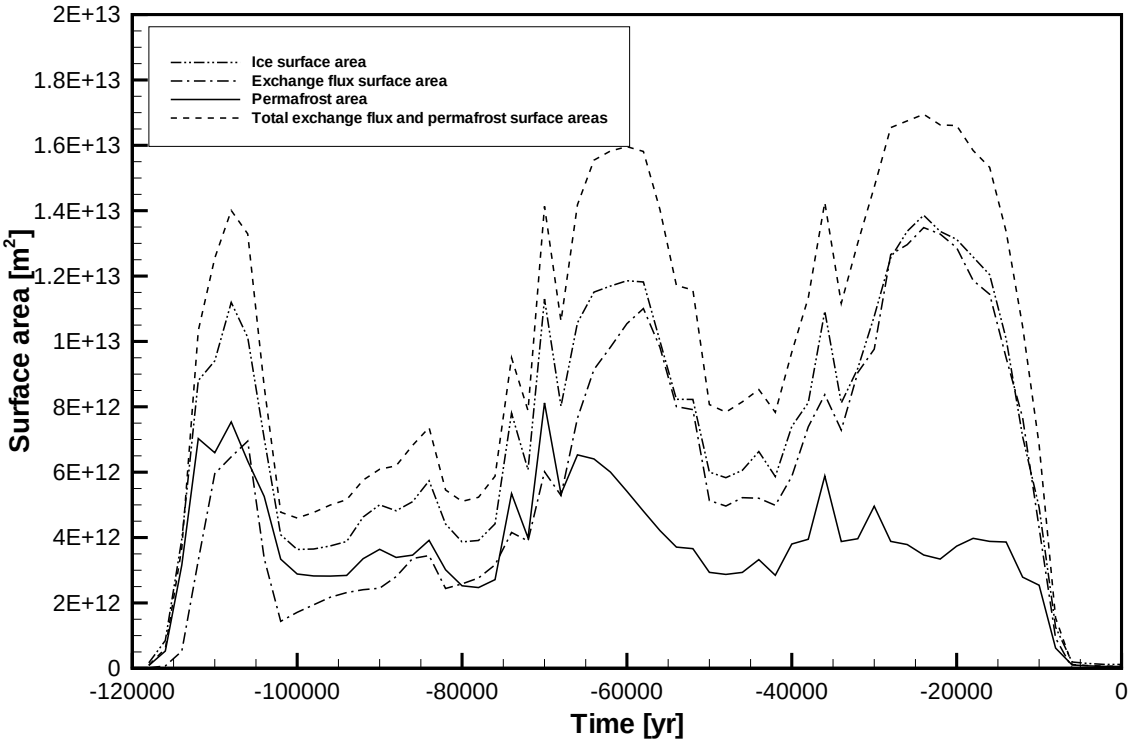

Figure 5.7: Ice surface, permafrost and subglacial water exchange areas over the glacial cycle.

ment has the effect of increasing the water exchange rates between the surface and subsurface (Figure 5.8b). Regions that were otherwise frozen are now open for water exchange with the surface. Infiltration and exfiltration continues to occur in the unfrozen regions as it did for the base-case scenario.

5.4 Summary

The subglacial environment is a complex region in which the subglacial meltwater undergoes infiltration, exfiltration and runoff below ice sheet pressure. Understanding subglacial processes is highly important because they have a major impact on ice-sheet dynamics, the formation of sedimentary structures and on groundwater flow and geochemical patterns. In this chapter, the spatial and temporal evolution of water

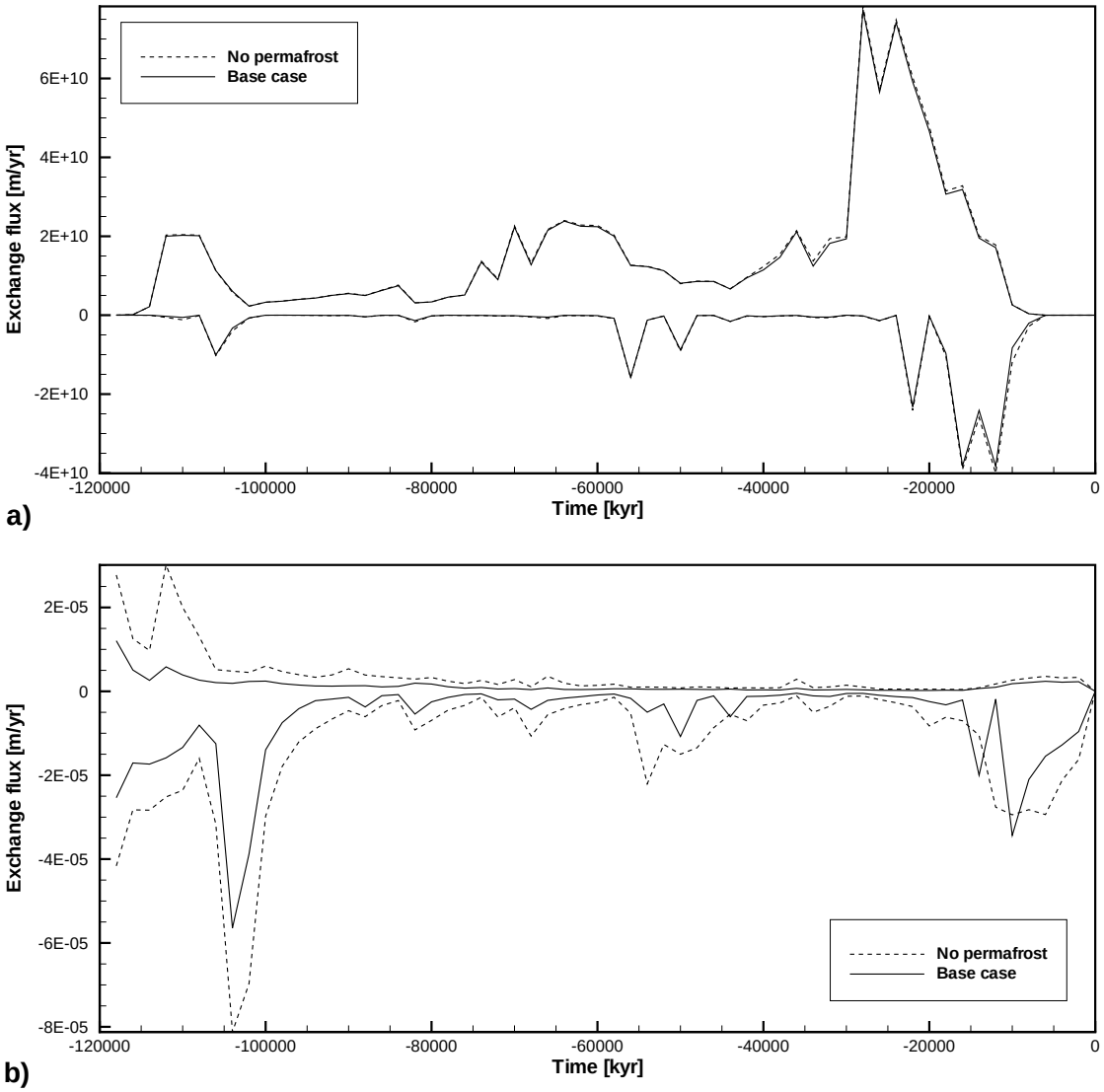

Figure 5.8: Infiltration (positive) and exfiltration (negative) rates for the base-case scenario and the zero-permafrost scenario for the a) subglacial environment; b) periglacial environment.

Table 5.1: Summary of the average infiltration and exfiltration rates for the subglacial and periglacial environments during the glacial cycle and the last interglacial period.

	Infiltration [m/yr]	Exfiltration [m/yr]
Subglacial environment	2.47×10^{-3}	2.03×10^{-3}
Periglacial environment	1.30×10^{-6}	7.08×10^{-6}
Interglacial period	2.87×10^{-5}	3.25×10^{-6}

exchange fluxes were examined in both the subglacial and periglacial environments. The influence of permafrost was addressed, as was the sensitivity of the computed exchange fluxes to the value of the hydromechanical loading efficiency parameter.

During the glacial period, the average subglacial infiltration rate into the subsurface oscillates between 0 and 6 mm/yr with an average of about 2.5 mm/yr, which is at least three orders of magnitudes higher than values in the periglacial environment and two orders of magnitude higher than those occurring during the interglacial period (Table 5.1). The periglacial environment has an infiltration rate that is much lower than the interglacial infiltration value, the later of which is about 0.03 mm/yr. The calculated infiltration during the interglacial is much lower than the 2 mm/yr value Thorne [2004] estimated from a hydrologic water balance of three catchments in the Canadian Shield. The ratio of the subglacial infiltration rate to the rate of subglacial meltwater production varies between 15% and 100%, with an average of 43%, which indicates that a large fraction of the meltwater actually entered the subsurface. The subglacial exfiltration rate can reach up to 12 mm/yr, with an average of 2 mm/yr, but occurs over a much smaller land area. This is about three orders of magnitudes higher than the amount occurring in the periglacial environment and during the interglacial period.

Regarding the timing of the water exchanges, most of the subglacial meltwater

infiltrates into the subsurface when the ice sheet is growing. Conversely, groundwater exfiltrates mainly during ice-sheet regression. Because of the high pressures at the bed of the ice sheet, meltwater is forced downward into the subsurface during ice-sheet advance and, when the ice sheet is regressing, the remnant pressure in the subsurface is higher than the basal meltwater pressure such that groundwater exfiltrates. This behavior was also noted in the 1D numerical experiment presented in Chapter 3 and is a consequence of the interaction between the subglacial boundary conditions and the elastic properties of the rock. A sensitivity analysis of the subglacial infiltration to the loading efficiency parameter was performed and showed that the infiltration rate into the subsurface decreases with an increase of the loading efficiency parameter.

In the periglacial environment, it was shown that the infiltration and exfiltration flux oscillates between 0 and 0.06 mm/yr, with average values in the range of 0.003 and 0.007 mm/yr, respectively. This is much lower than that in the subglacial environment. Most of the exchange flux is dominated by exfiltration during ice sheet regression, as it is the case for the subglacial environment.

The subglacial infiltration rate is also dependent on the rock type, as expected, because of the control exerted by rock permeability. It also appears that the difference in the subglacial infiltration rate between the different rock types increases during glacial advances.

The permafrost has the effect of constraining large areas of the subglacial environment from experiencing surface/subsurface water interactions. The subglacial permafrost mainly exists in cold-based areas below the ice sheet, which are regions that do not produce large quantities of subglacial meltwater. For this reason, when the presence of permafrost is ignored, little change is seen in the surface/subsurface water exchange fluxes in the subglacial environment. On the other hand, the neglect of permafrost in the periglacial environment encourages surface/subsurface water in-

teractions and an increase of the exchange rates.

Chapter 6

Impact of the Wisconsinian Glaciation on the Canadian Continental Groundwater Flow

"The most erroneous stories are those we think we know best - and therefore never scrutinize or question."

Stephen Jay Gould

In this chapter, the impact of the last glacial period on Canadian continental groundwater flow and brine distribution is examined in detail using the model described in Chapter 4. First, the base case scenario will be addressed followed by various other cases that will allow an appreciation of the impact of glacial loading and permafrost evolution on the groundwater flow system and the TDS concentration patterns during a glacial period.

6.1 Base-Case Scenario

Before examining the impact of the glacial cycle on continental groundwater flow, the simulated TDS profile with depth at the end of the glacial cycle will be compared to the observed profile, as was done in Chapter 4 for the last interglacial. The TDS data represent one of the few datasets available to validate the model at this scale. Figure 6.1 shows the simulated and observed TDS profiles in the Shield and in the Michigan basin. In the Canadian Shield as well as in the Michigan basin, the simulated results yield high concentrations at depth, but they fail to fit the observed data over the first 1000 m. In the upper 1000 m of the Shield, the observed TDS increases rapidly from a low concentration on the surface (10^2 mg/l) to about 10^5 mg/l at greater depths. As mentioned in Section 3.3.2, the freezing of water will expel TDS through salt rejection and consequently the ground ice will contain little salt. As a consequence, during a subsequent period of thaw, the TDS values would be low at shallow depths, noting that the permafrost usually forms within the upper 1000 m. Because salt rejection is not included in the model, the discrepancy between the observed and simulated TDS profiles is expected.

Another explanation for the steep and uniform vertical TDS profile can be given by the large longitudinal dispersivities used in the numerical model. Large longitudinal dispersivities were selected to account for the large size of the finite elements and sub-grid-scale heterogeneity that would promote mixing along horizontal flow directions. During subglacial meltwater infiltration, the vertical gradients become more important than the horizontal gradients such that the large longitudinal dispersivities would promote strong and rapid solute mixing along all the vertical direction. This could also explain the fairly uniform concentrations along the vertical direction, recognizing that such a large scale model didn't permit very fine grids and the use of

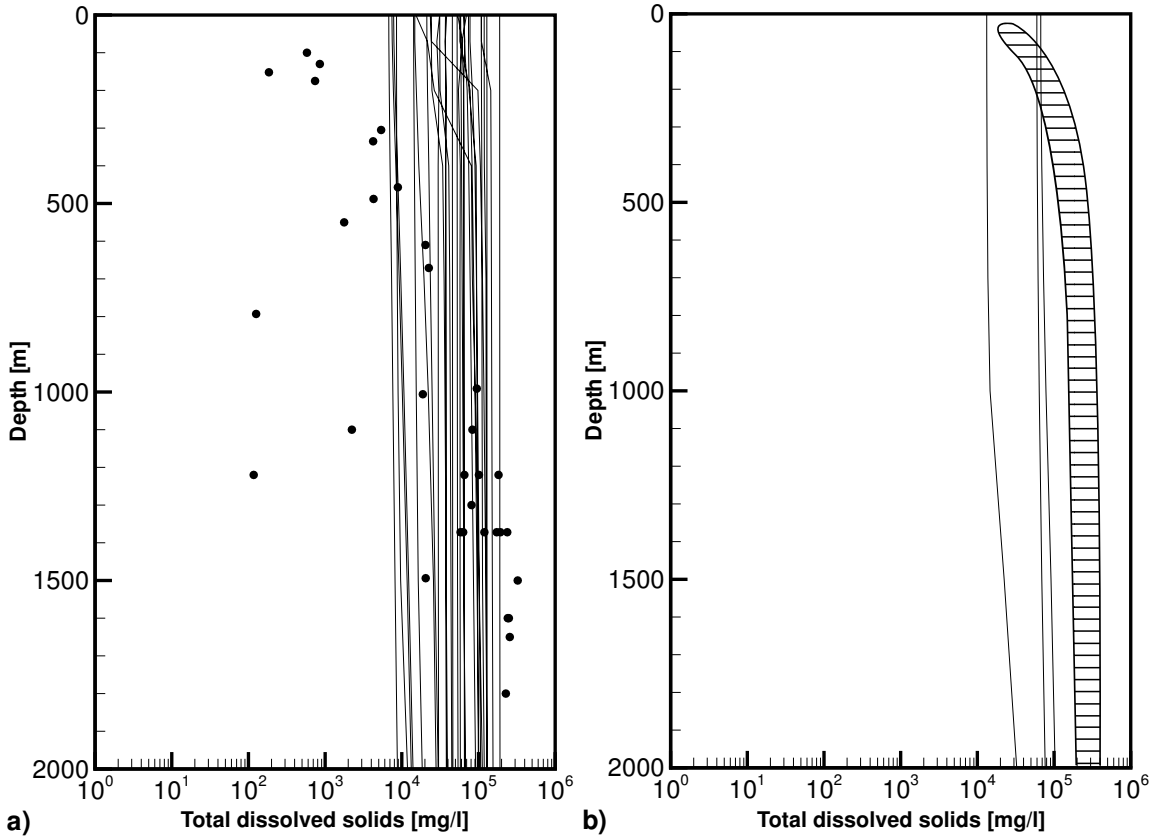

Figure 6.1: Simulated and observed total dissolved solids versus depth after the glacial cycle (0 kyr) in a) the Canadian Shield and b) the Michigan basin. Simulated TDS profiles are shown as continuous lines in both figures and observed TDS profiles are shown as points for the Canadian Shield and with a hatched zone for the Michigan basin.

small dispersivities.

The impact of the ice sheet on continental groundwater flow over the full glacial cycle will first be examined at several specific observation points distributed across the domain. At these locations, the vertical evolution of the groundwater system in response to the surficial conditions can be explored. The locations of the observation points are shown in Figure 6.2. Figures 6.4 to 6.8 show the simulated hydraulic heads and solute concentrations at different depths along with the boundary conditions and climatic conditions applied on the surface over the glacial cycle. Each location was

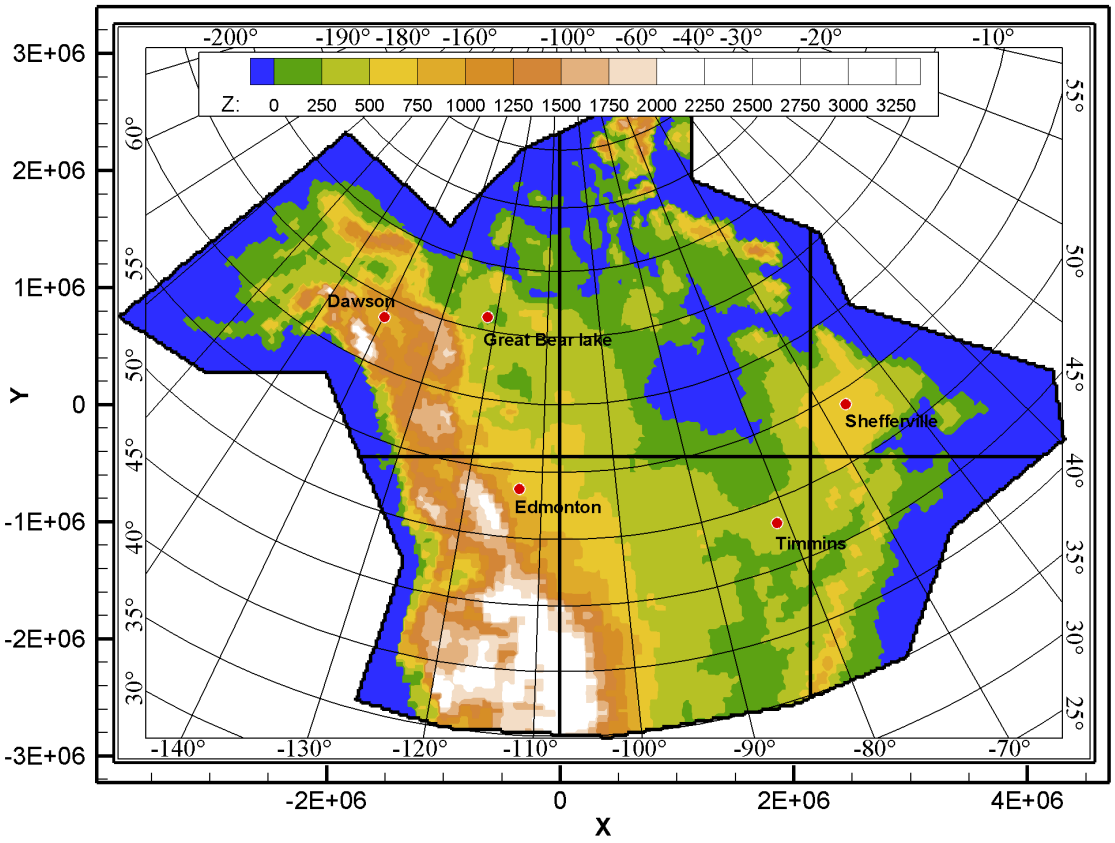

Figure 6.2: Location of the observation points and the three cross sections taken from the numerical model (x = 0.0 m, x = 2.14×10^6 m and y = -4.6×10^5 m). Color contours show surface elevation at -120 kyr. Coordinate system is shown both in longitude/latitude [degree] and $x-y$ Cartesian [m]. Red dots and their labels are the observation points.

chosen in order to highlight a specific behavior such as the impact of permafrost or ice-sheet thickness on the subsurface hydraulic conditions.

In order to visually illustrate the surface climatic conditions, a "climatic condition" graph is displayed on Figures 6.4 to 6.8 along with the applied boundary conditions at the surface of the flow model. Figure 6.3 displays a sample of the climatic condition graph. Above the horizontal line separating subglacial and periglacial conditions, subglacial conditions prevail while periglacial conditions prevail below the line. The black infilled region indicates that the subsurface is frozen and an unfilled

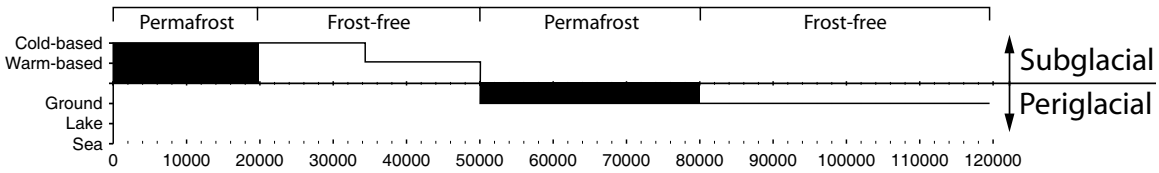

Figure 6.3: An example of climatic conditions. Above the horizontal subglacial/periglacial line, subglacial conditions prevail while periglacial conditions prevail below the line. Black filled boxes indicate permafrost and the open boxes indicates frost-free conditions. Subglacial conditions can be warm- or cold-based and the water table for periglacial conditions can be at the ground surface, at a periglacial lake level or at sea level.

box indicates frost-free conditions. For subglacial conditions, the bottom of the ice sheet can be warm-based, meaning there is subglacial melting, or cold based, meaning there is no subglacial melting. For periglacial conditions, the water table can be at ground surface level, at a periglacial lake level or at sea level.

Along with the climatic conditions graph, part (b) of Figures 6.4 to 6.8 contains a summary of the surface boundary conditions applied at the observation locations. The "elevation" axis on the left is used to designate the value of several variables such as specified hydraulic head and permafrost depth. Other variables displayed are the surface elevation and ice-sheet thickness. The summation of the ice-sheet thickness and the ground surface elevation gives the ice-sheet surface elevation. Permafrost thicknesses are shown as negative values to symbolize that it is progressing downward into the ground. The summation of the surface elevation and the permafrost thickness gives the elevation of the lower limit of the permafrost. Specified heads are designated using discrete symbols when this boundary condition is active in the model. A specified water flux, using values corresponding to the axis on the right, is prescribed when the specified head boundary condition is inactive and subglacial meltwater is being produced.

The first observation point is located at Edmonton, Alberta (Figure 6.4). It was

chosen because it is a location only affected by the third and final glacial advance and because it displays a simple response of groundwater flow to the ice sheet passage. It can be seen in Figure 6.4a that an ice sheet did not affect this location until -31 kyr and that permafrost was present up to this point in time. During the ice-sheet-free period, small hydraulic changes are observed at all depths (Figure 6.4c). Because the hydraulic head incorporates an elevation component and because the elevation of the land surface changes with time, the hydraulic head variation is solely due to these elevation changes. The solute concentration curves (Figure 6.4e) show small variations with time, especially at shallow depths. The fluctuations cannot be explained solely by the applied surface boundary conditions. Rather, they are likely to be the result of lateral groundwater flow. At -28 kyr, the permafrost disappears as the ice sheet covers the land surface. Meltwater production starts and the hydraulic head at shallow depths rises quickly to values near 3000 m (Figure 6.4c). The flux magnitude also rises quickly at shallow depths (Figure 6.4d) and the solute concentration diminishes as fresh meltwater infiltrates into the subsurface (Figure 6.4e). The time gap between the ice sheet arrival (-31 kyr) and its impact on groundwater is due to permafrost which takes about 3 kyr to melt before allowing the subglacial meltwater to infiltrate into the subsurface. It can be seen that solute dilution occurs at great depth, because at an observation depth of 3,798 m, the relative concentration diminishes from a value of about 0.6 to nearly zero (Figure 6.4e). The hydraulic head amplitude diminishes with depth and there is a phase shifting of the peak head with depth due to slow hydraulic diffusion. Near the surface, the hydraulic head responds rapidly after the ice sheet retreats but the over-pressurized water at depth takes much longer to recover (Figure 6.4c). A phase shift in the solute concentration curves occurs with depth because the meltwater that infiltrates into the subsurface takes time to reach great depths (Figure 6.4e). Finally, inspection of the flux magnitude curve (Figure 6.4d)

reveals that infiltration into the subsurface occurs as a succession of pulses, rather than at a steady constant rate.

The second observation point is located near Yellowknife, NWT, in the centre of Great Slave Lake. This location is affected by the three glacial advances as can be seen from the ice thickness curve (Figure 6.5b). Before the first glacial advance which occurred between -112 and -105 kyr (Figure 6.5a), the land surface was located under the freshwater within Great Slave Lake and the subsurface soil was frozen to a depth of 100 to 200 m. During the first glacial advance, the ice sheet reached a thickness of about 2 km and was warm-based for only two short periods during this time (at -110 and -106 kyr). A very small quantity of subglacial meltwater (essentially not visible in Figure 6.5b) infiltrated into the subsurface and produced a small hydraulic head rise (Figure 6.5b). The subglacial infiltration during the first glacial advance is sufficient to produce a small rise in the velocity magnitude (Figure 6.5d) near the surface and to dilute the TDS (Figure 6.5e).

The second glacial advance (-71 to -54 kyr) near Yellowknife affected the groundwater flow system, but only near its end. At the beginning of this glacial advance, the hydraulic head variations mimic the surface elevation changes (Figure 6.5c) and no increase in the Darcy flux is observed (Figure 6.5d). This occurs because the meltwater production only starts at -60 kyr, when the ice sheet becomes warm-based instead of cold-based. Then, hydraulic head values at all depths increase and a meltwater infiltration pulse advanced into the subsurface (Figure 6.5d). The hydraulic head on the surface reaches about 1000 m which is much higher than the value that existed during the previous ice advance. The solute concentration diminishes, especially at shallow depths (Figure 6.5e), but also to a lesser extent at large depths and later times due to dilution.

The third glacial advance spans from -31 to -11 kyr (neglecting the cold-based

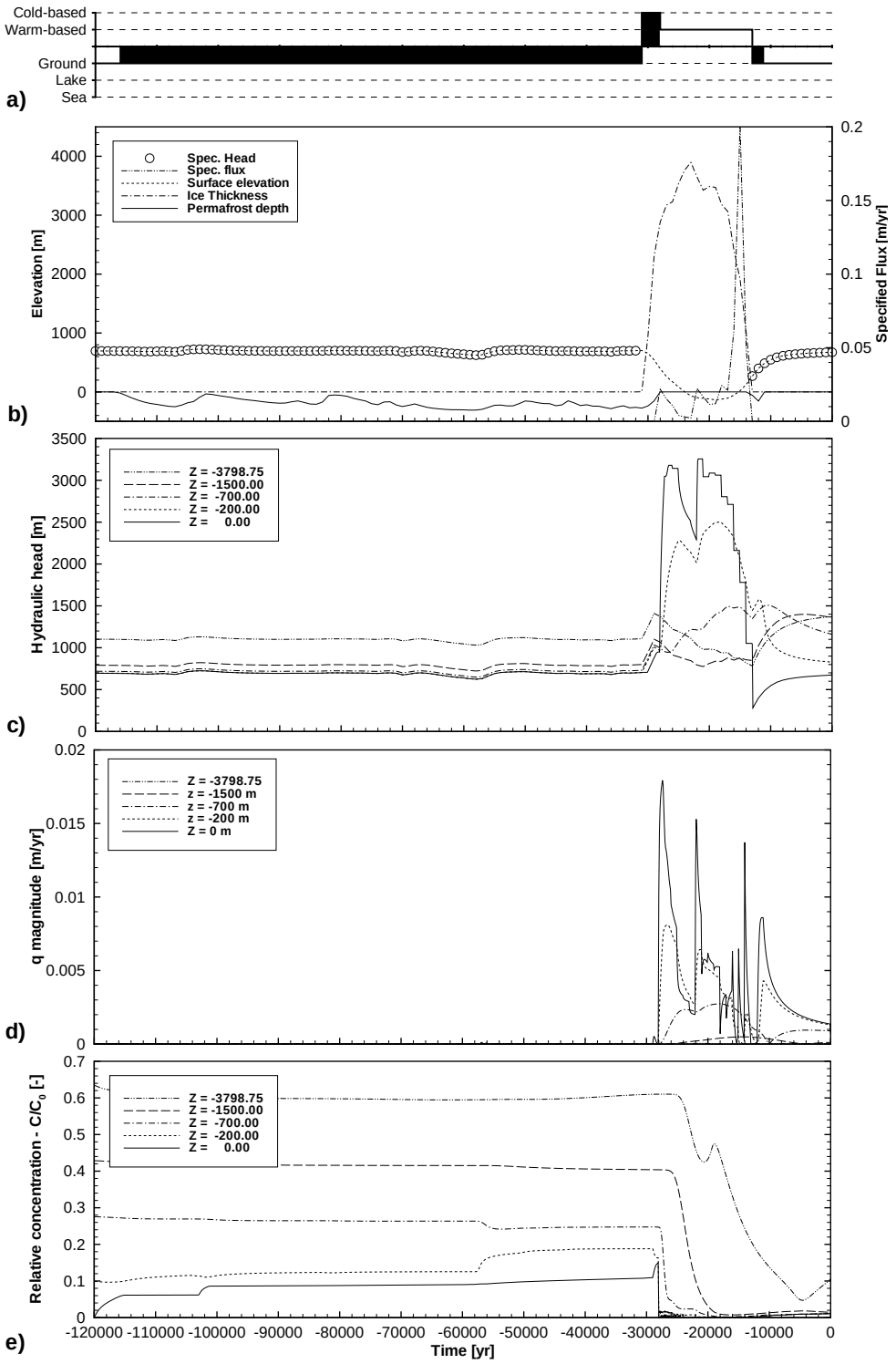

Figure 6.4: Observation point located at Edmonton, AB. a) Surface climatic conditions. b) Surface boundary conditions. c) Simulated hydraulic head. d) Simulated Darcy flux magnitude. e) Simulated relative concentration (C/C_{max}).

ice pulse that occurred between -37 and -34 kyr). This third glacial advance is the most important of the three in terms of duration and intensity because the ice sheet reached a thickness of about 5 km at LGM and the warm-based period spans over 17 kyr. When the ice sheet becomes warm-based around -29 kyr, it produces a subglacial meltrate of about 2 cm/yr which is enough to raise the surface hydraulic head to about 3000 m (Figure 6.5c). This is less than the equivalent freshwater head of the ice sheet weight which suggests that the meltrate does not exceed the draining capacity of the bedrock. The hydraulic head rises at all depths as the pressure pulse diffuses downward into the crust and is sustained for a long period of time by the ongoing meltwater production below the warm-based ice sheet. The effect of the meltwater pulse is also noted at depth by the increase in the magnitude of the Darcy velocity (Figure 6.5d) and decline in the TDS concentration to near zero (Figure 6.5e). Near the end of the glacial advance, at -12 kyr, there was a large subglacial meltwater pulse of about 10 cm/yr which raised the surface hydraulic head to a value equal to the ice-sheet-equivalent freshwater head. The effect of this pulse is again felt at depth where the magnitude of the Darcy flux reaches a value of 1.7 cm/yr, whereas the background value at this location is only 1.0×10^{-3} cm/yr (Figure 6.5e).

The two previous observation points are located in more permeable sedimentary facies and, because of this, relatively high subglacial infiltration rates can occur before the rate becomes limited by the constraint that the hydraulic head at the surface cannot exceed the equivalent head of the ice-sheet thickness. The next two observation points are located in the Canadian Shield, whose rocks have lower hydraulic conductivity.

At the observation point located near Timmins, Ontario (Figure 6.6), the impact of three glacial advances on groundwater flow is clearly discernible. The last glacial advance is divided into two advances separated by a short period of land surface ex-

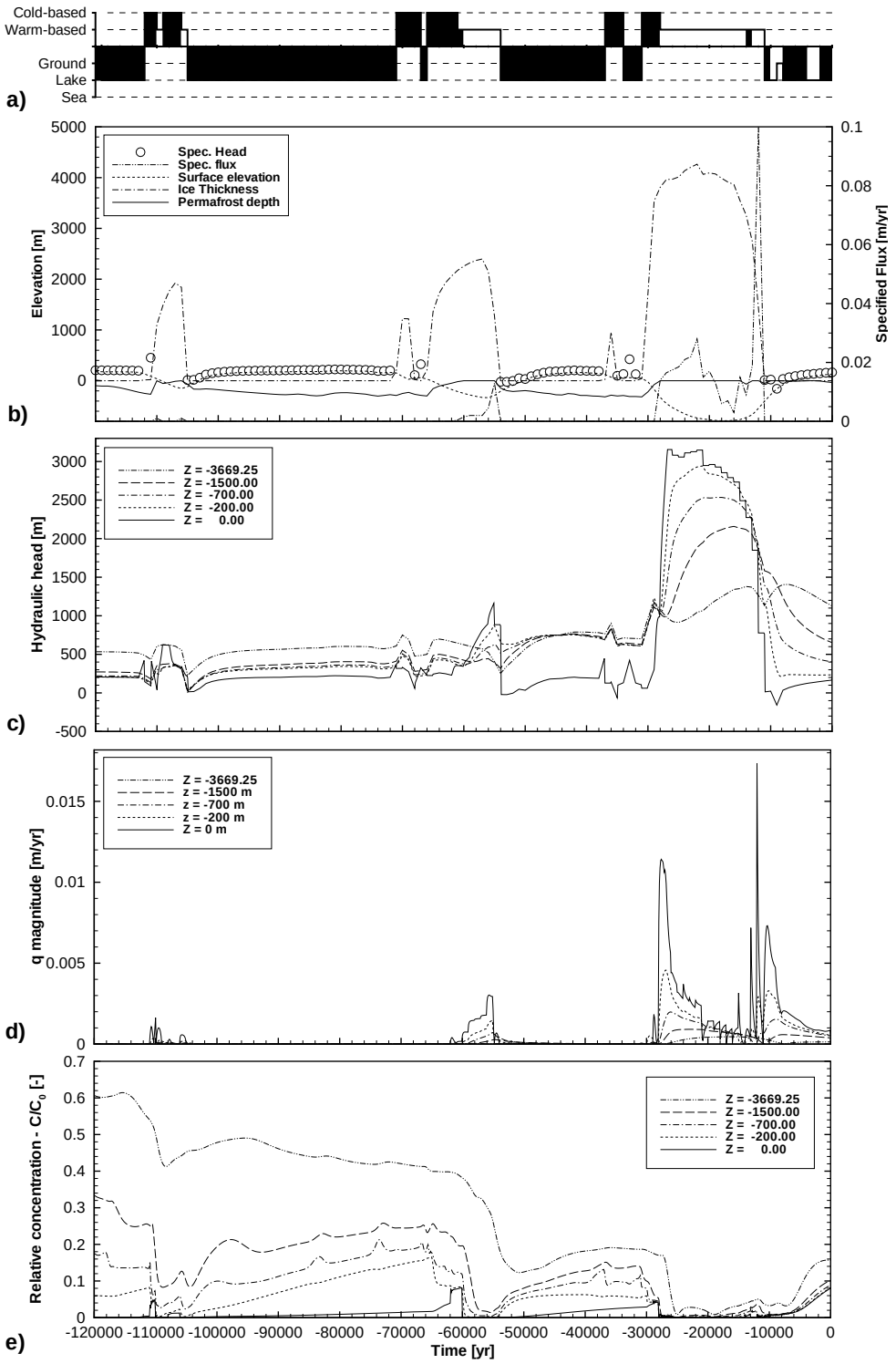

Figure 6.5: Observation point located in Great Bear lake, NWT. a) Surface climatic conditions. b) Surface boundary conditions. c) Simulated hydraulic head. d) Simulated Darcy flux magnitude. e) Simulated relative concentration (C/C_{max}).

posure. The first glacial advance (-112 to -104 kyr) produced a warm-based ice sheet over the period -110 to -105 kyr (Figure 6.6a) during which there was meltwater production (Figure 6.6b). The magnitude of the groundwater velocity increases due to the infiltration of the subglacial meltwater (Figure 6.6d) and as a consequence, the solute concentration diminishes (Figure 6.6e). Note that spurious numerical oscillations occur at the land surface where the velocity is very high but they diminish soon after the sharp meltwater pulse terminates and the groundwater velocity returns to lower values. The hydraulic head increases by more than 1000 m near the surface but becomes constrained by the ice-sheet thickness criterion. At depth, the head increases by a few hundred meters. The direction of the hydraulic gradient also reverses. Initially, the surface hydraulic head becomes higher than the head at depth as meltwater infiltrates into the subsurface but the opposite occurs when the ice retreats. After the retreat of the ice, the head stabilizes, as well as the concentration, and the permafrost returns to the land surface.

At -71 kyr, another glacial advance begins and, at -67 kyr, the ice sheet becomes warm-based and meltwater production starts again. The meltwater dilutes the TDS and solute concentration diminishes while the hydraulic gradient is reversed from upward to downward. At the end of this second advance, the solute concentration (Figure 6.6e) rises slowly but diminishes rapidly shortly after the third glacial advance starts at -41 kyr. The Darcy velocity magnitude peaks at about 4 mm/yr, which is quite low compared to peak values in the sedimentary facies. Again, during most of the second glacial advance, the hydraulic head at the surface is constrained by the ice-sheet thickness criterion because the bedrock cannot drain all of the subglacial meltwater.

After the ice retreat, the head on the surface returns to a value equal to the land-surface elevation while the head is still quite high at depth (Figure 6.6c). The

surface head then rises rapidly at the start of the third glacial advance (-41 kyr), which produces a meltwater pulse that peaks at 4 cm/yr. Then, depending on the rate of meltwater production, the solute concentration diminishes. Similar to the two previous ice advances, the hydraulic head at the surface is constrained by the ice sheet thickness. After the glacial maximum, the hydraulic head at all depths slowly returns to its original values; more rapidly near the surface, but slowly at depth. It can be seen that, at the end of the simulation, the head at depth has still not recovered to its original value. The concentration at the end of the simulation is also much lower at depth than it was originally.

Another observation point located in Shefferville, PQ, provides considerable insight into the impact of glacial cycles on groundwater flow in a Canadian Shield environment (Figure 6.7). It is located near a local ice-thickness maximum of the Laurentide Ice Sheet (Figure 6.2). The first two glacial advances are associated with cold-based conditions which prevent subglacial meltwater production due to the presence of permafrost, which has depths ranging between 200 and 400 m (Figures 6.7a and 6.7b). During this time-frame, the hydraulic head values evolve in accordance with the surface elevation changes and with the ice-sheet thickness that loads the surface (Figure 6.7c).

The third glacial advance starts at -75 kyr with cold-based conditions. At that point in time, the hydraulic head reflects the land elevation and the surface loading. With time, however, it can be seen that the head at all depths changes less than the change in surface elevation due to the hydromechanical effect of the ice loading on subsurface pore pressures. At -52 kyr, the ice sheet becomes warm-based and meltwater production starts. Hydraulic heads respond rapidly to the meltwater infiltration and rise suddenly to reach the ice-sheet-thickness constraint on the surface (Figure 6.7c). A subdued and less intense rise in the hydraulic head is seen at depth

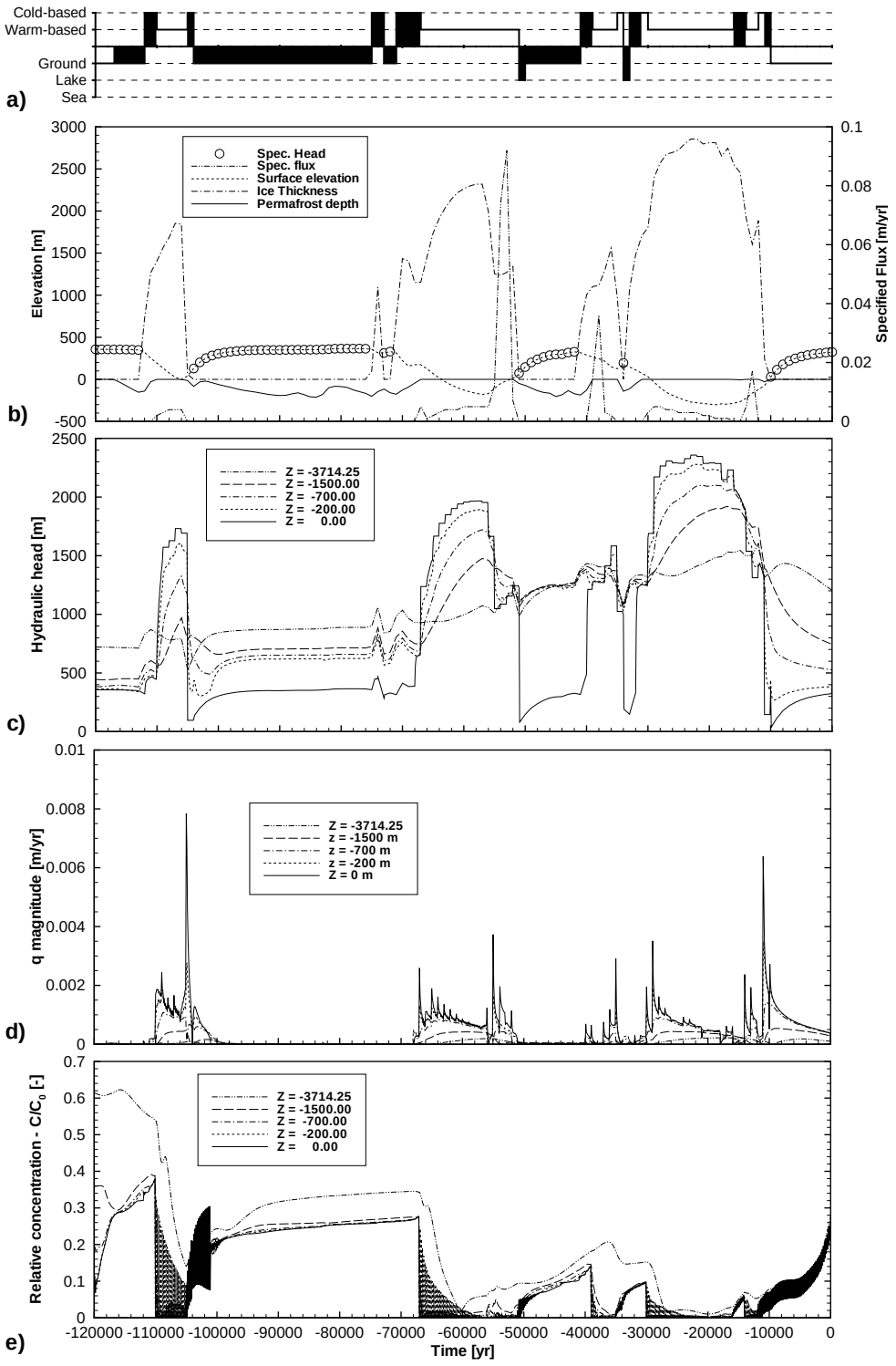

Figure 6.6: Observation point located in Timmins, ON. a) Surface climatic conditions. b) Surface boundary conditions. c) Simulated hydraulic head. d) Simulated Darcy flux magnitude. e) Simulated relative concentration (C/C_{max}).

and a reversal in the hydraulic gradient develops. When the production of subglacial meltwater commences, solute concentrations diminish quickly at depth and reach a low value (Figure 6.7e). The concentration then rises slowly after the retreat of the ice sheet. The magnitude of the groundwater velocity rises as expected when the subglacial meltwater starts to infiltrate and becomes more or less steady for 7 kyr at 1 mm/yr. Then, even if the meltrate increases, the velocity magnitude diminishes because the head on the surface becomes constrained by the ice-sheet-thickness criterion which limits the infiltration into the subsurface. Near the end of the glacial advance, there is a rapid and intense change in the velocity before the permafrost returns on the land surface. Then, it can be seen that the head at depth remains at a high value at the end of the simulation and is far from recovering to its initial value.

Finally, there are some locations, such as Dawson City, YT, that were not covered by the ice sheet. Dawson was affected by permafrost at the last interglacial, much like it is today. Throughout the last glacial cycle, the permafrost penetrated deep, from about 230 m to 405 m, and therefore formed a continuous seal between the atmosphere and the groundwater (Figure 6.8b). The hydraulic head does not change much at depth during the glacial cycle; most of the changes are due to topographic elevation variations related to glacial isostasy in neighbouring regions (Figure 6.8c). Concentrations also do not change significantly except near the end of the cycle, where the concentration at 200 m rises slightly and a minor increase in groundwater flux is noted (Figure 6.8e).

Additional insights pertaining to the impact of the Wisconsinian glaciation on continental groundwater flow can be gained by examination of the simulation results along selected cross sections. Three vertical cross sections were extracted from the three-dimensional model to capture the hydraulic head and TDS concentration response as affected by permafrost evolution and ice-sheet loading at selected time slices

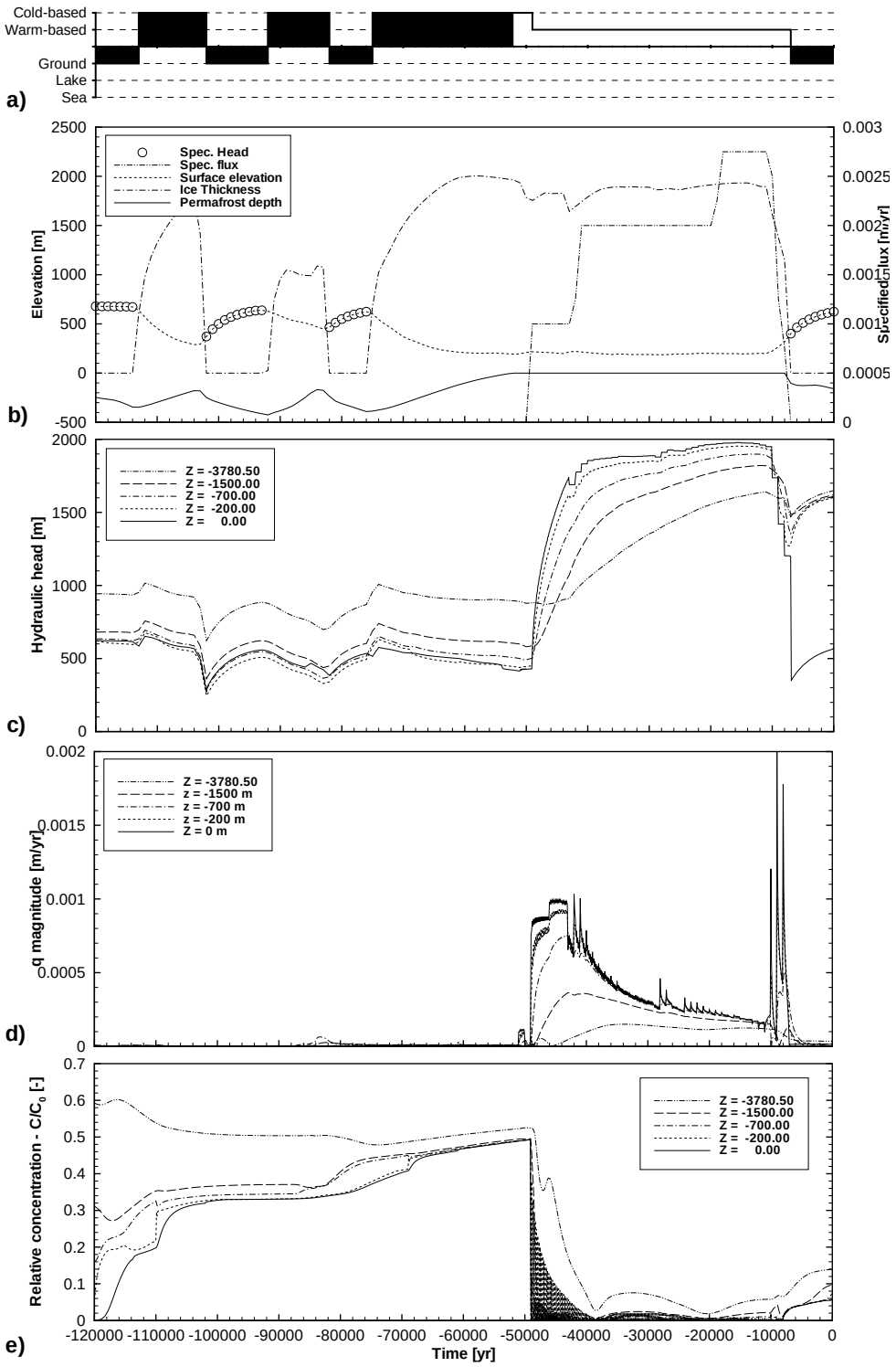

Figure 6.7: Observation point located in Shefferville, PQ. a) Surface climatic conditions. b) Surface boundary conditions. c) Simulated hydraulic head. d) Simulated Darcy flux magnitude. e) Simulated relative concentration (C/C_{max}).

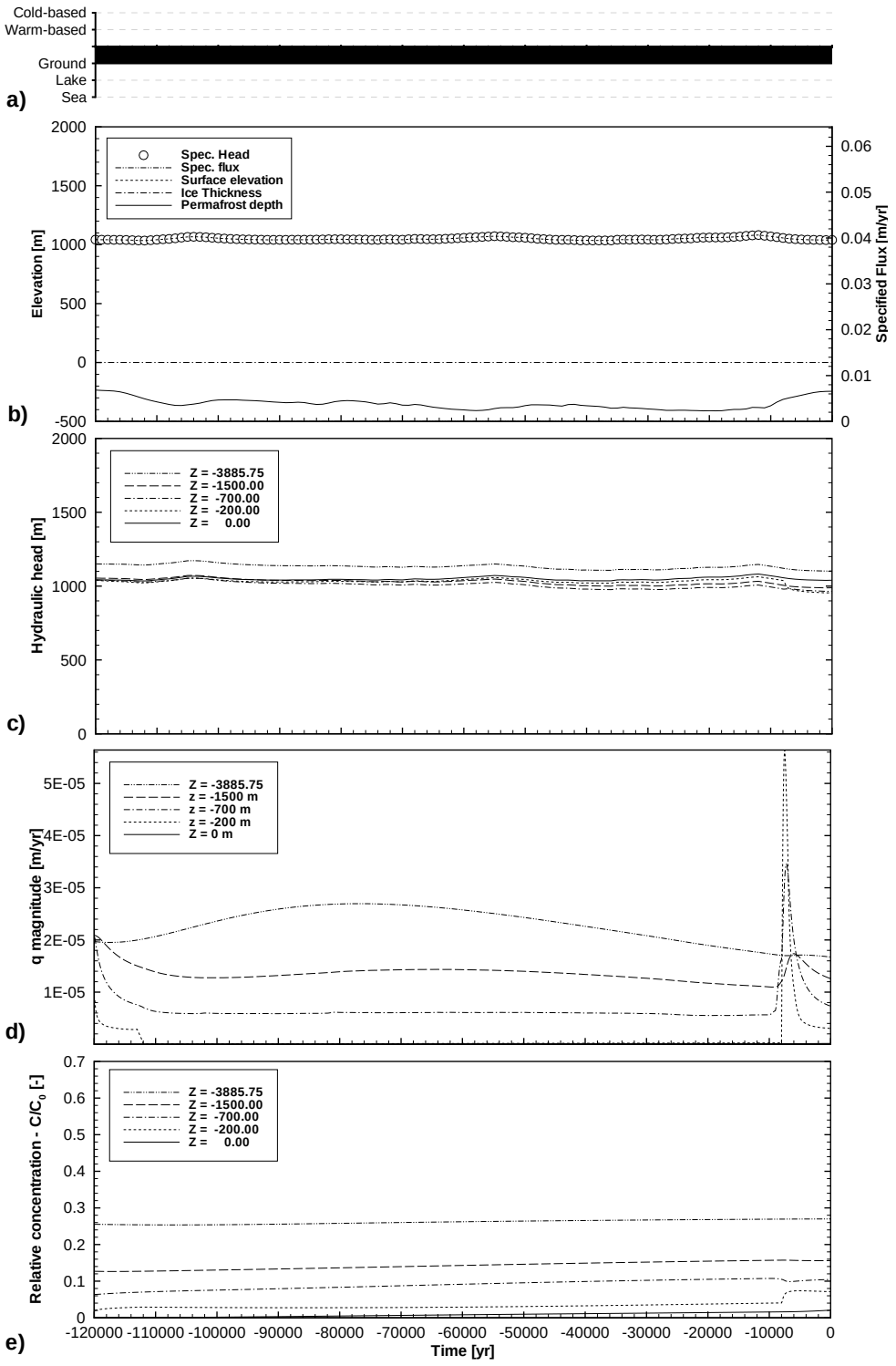

Figure 6.8: Observation point located in Dawson, YT. a) Surface climatic conditions. b) Surface boundary conditions. c) Simulated hydraulic head. d) Simulated Darcy flux magnitude. e) Simulated relative concentration (C/C_{max}).

(Figures 6.10 to 6.18). The locations of the cross sections are shown in Figure 6.2 and the geology along them as represented in the model is shown in Figure 6.9. The cross sections were chosen because they pass close to regions of maximum glacial loading (*i.e.*, ice domes that formed in Labrador and Alberta). For each of the cross sections, a time slice at LIG (-120 kyr) was chosen, followed by a time slice slightly before the LGM (-30 kyr), at LGM (-20 kyr), slightly after LGM (-14 kyr) and finally at present time (0 kyr). This succession of time slices sufficiently captures the impact of the ice sheet on groundwater flow. For illustrative purposes, the ice-sheet thickness and its lateral extent is shown as the grey region on the top of each cross section. Note that the permafrost index provided in the scale shown in Figures 6.12, 6.15 and 6.18 varies from zero to one and represents the degree that the ground ice affects the subsurface permeability. If the subsurface material is frozen, the permafrost index is unity and if there is no permafrost present, the index is zero. A value between zero and one indicates that the geologic material is at an intermediate state of freezing (or thawing) as reflected by the linear interpolation between the frozen and unfrozen permeability values during the 1000-kyr time slices over which the permafrost distribution is updated in the model.

The first cross section, located at $x = 0$ m, is a cross section that is located more or less along an ice flow line (Figures 6.2 and 6.9a). On the other hand, it is not along a groundwater flow line because the bulk of the groundwater movement is from the Rockies, flowing eastward to northeastward. The cross section therefore cuts across the groundwater flow direction. The southern part of the cross section extends to the Rockies of the United States, near Albuquerque, NM. The topographic elevation along the cross section is highest in the St-Juan Mountains in Colorado before gently sloping toward the Arctic Ocean and then the Victoria and the Parry Islands. At LIG, the groundwater flow system is seen to be a subdued replica of the surface

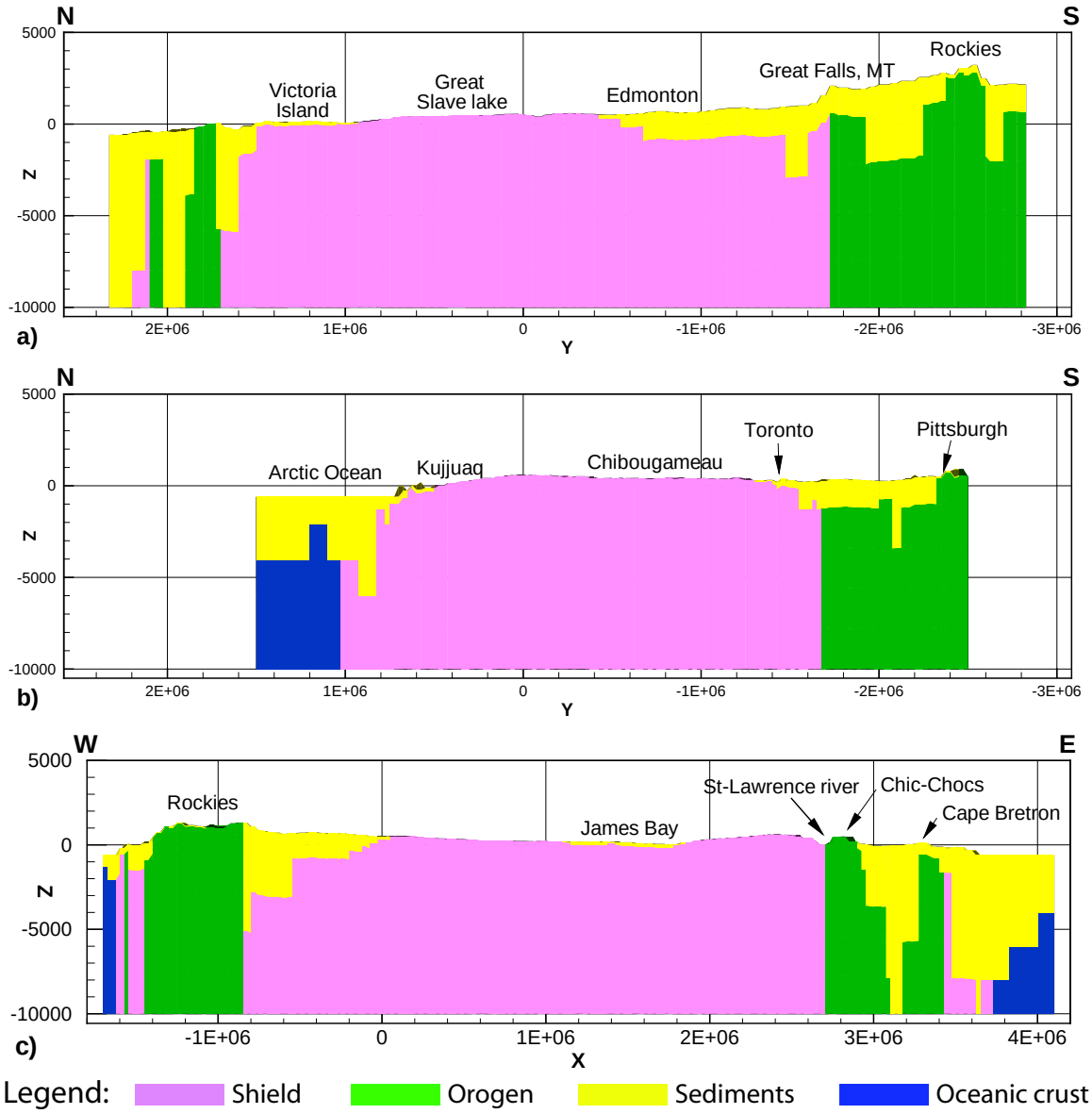

Figure 6.9: Geology of the three cross sections: a) $x = 0$ m; b) $x = 2.14\times10^6$ m and c) $y = -4.63\times10^5$ m. The colors represent each of the facies described in Section 4. Vertical exaggeration: 100×.

elevation (Figure 6.10a) and the solute concentrations with depth are different in the Shield than in the Orogen facies. In the Canadian Shield, the concentrations exhibit a smooth and fairly uniform increase with depth in the center of the cross section while the depth pattern is more skewed in the Orogen facies of the mountains. Note that the change in the concentration profiles are sharp between the different facies (*i.e.*, at $y = 1.7\times10^6$ m on Figure 6.11a). The permafrost zone starts at $y = -5.0\times10^5$ m and thickens to the north to reach a maximum thickness of about 1 km under the Arctic Ocean (Figure 6.12a).

The second cross section, located at $x = 2.14\times10^6$ m, exhibit a much flatter topography than the previous one (Figures 6.2 and 6.9b). Again, the rocks present over most of this cross section are the Shield rocks. The southern part of the cross section is located near Pittsburgh, PA, close to the Appalachian Mountains. The cross section then cuts across Lake Erie, Southwestern Ontario, Northern Ontario and then passes very close to the east of James and Hudson Bay, continuing north to the east of Baffin Island where it ends in the Arctic Ocean. In the northern part of the cross section, the ocean floor, whose elevation is at -600 m, represents about 20% of the section. The initial hydraulic head distribution at LIG exhibits a gravity-driven character with flow occurring from zones of high topography to regions of lower elevation (Figure 6.13a). The regional flow system does not exhibit high hydraulic gradients as seen in the previous cross section due to a lack of high-elevation mountains. The solute concentration pattern on this cross section is similar to that shown in the previous section because of the smooth increase in concentrations with depth in the Canadian Shield (Figure 6.14a). Permafrost affect the near-northern part of the section, although it disappear from the northern extremity of the section, under the Arctic Ocean (Figure 6.15a). The maximum permafrost thickness is also less than that along the previous cross section since it only reaches a depth of 600 m

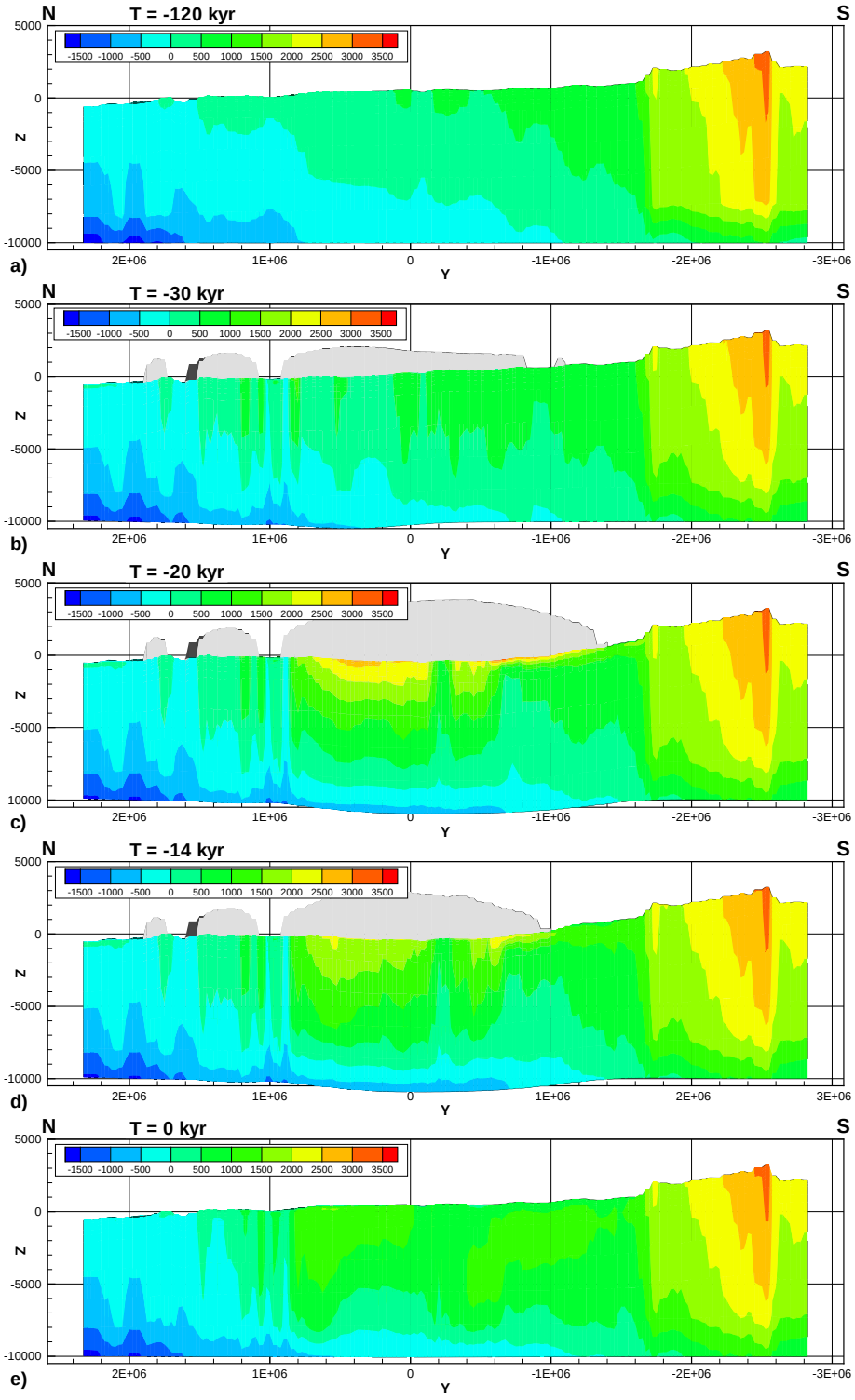

Figure 6.10: Hydraulic head along a cross section located at $x = 0$ m at selected time slices: a) -120 kyr; b) -30 kyr; c) -20 kyr; d) -14 kyr and e) 0 kyr. Vertical exaggeration: 100×.

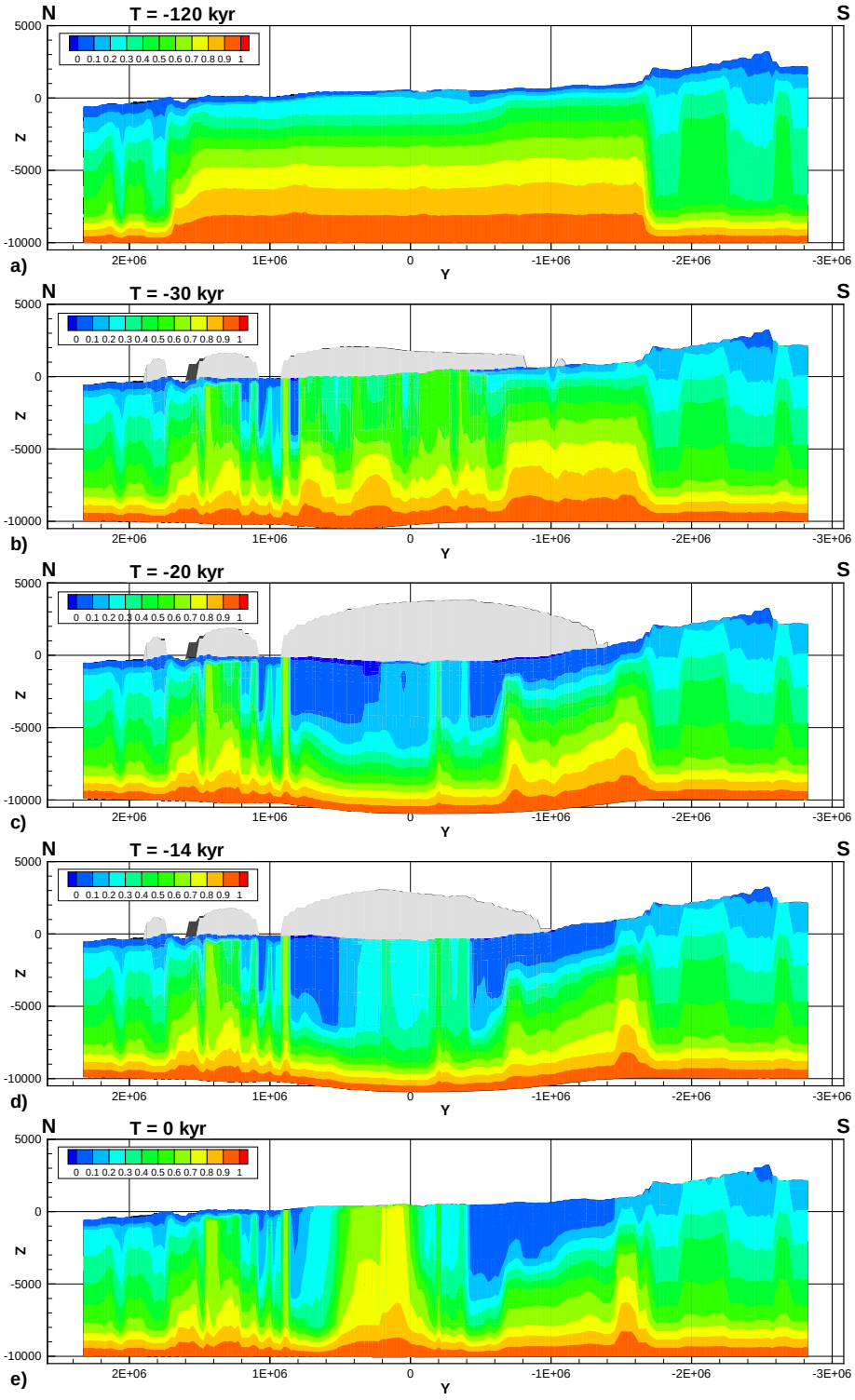

Figure 6.11: Relative concentration (C/C_{max}) along a cross section located at $x = 0$ m at selected time slices: a) -120 kyr; b) -30 kyr; c) -20 kyr; d) -14 kyr and e) 0 kyr. Vertical exaggeration: 100×.

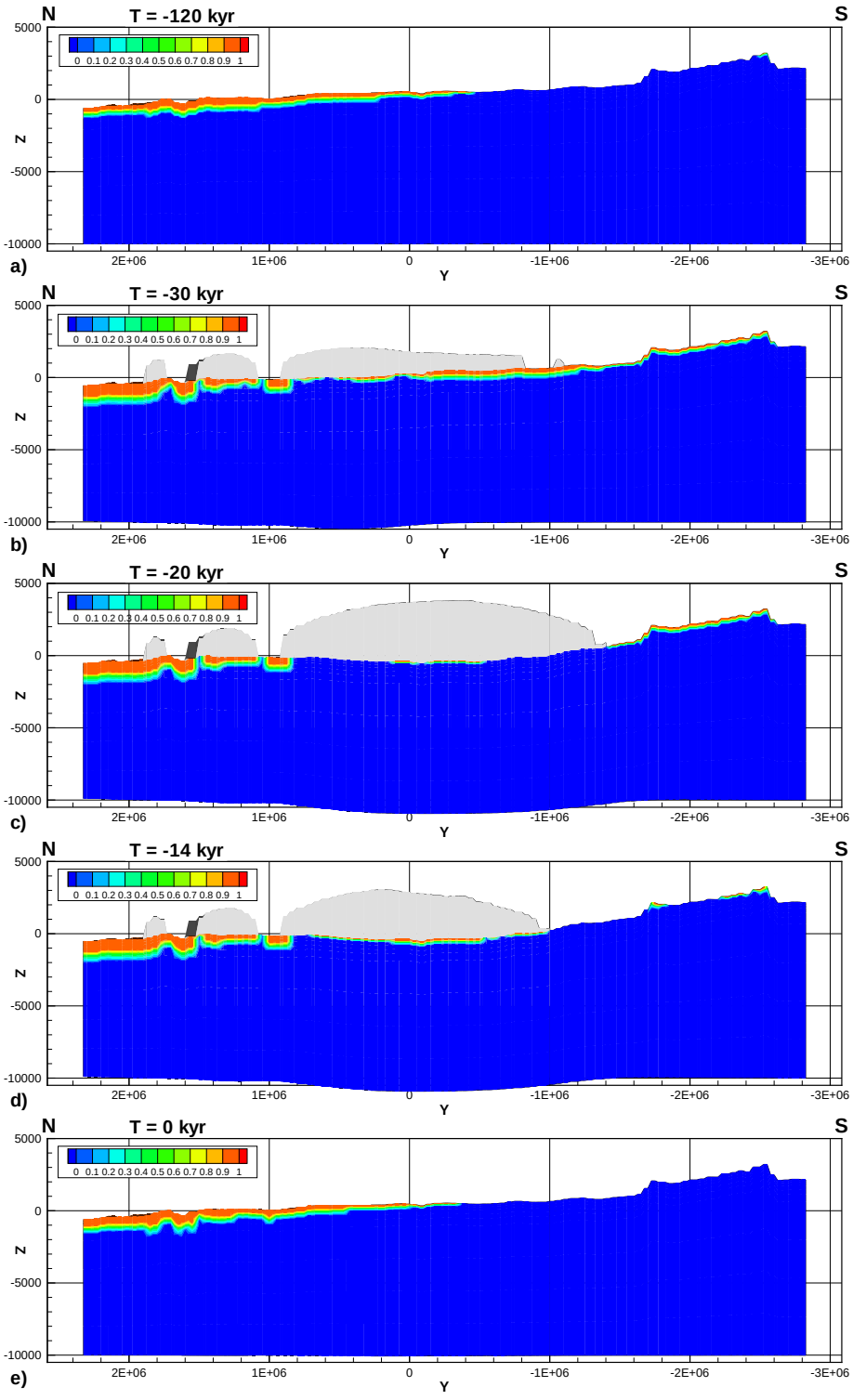

Figure 6.12: Permafrost along a cross section located at $x = 0$ m at selected time slices: a) -120 kyr; b) -30 kyr; c) -20 kyr; d) -14 kyr and e) 0 kyr. Vertical exaggeration: 100×.

to 700 m.

The third cross section is an east-west cross section located at y = -4.63×10^5 m (Figures 6.2 and 6.9c). It crosses British Columbia, Alberta, Saskatchewan and Manitoba about midway, then passes through northern Ontario, just below James Bay in Quebec and cuts through Gaspesia followed by Cape Breton Island and the Atlantic Ocean. The surface elevation is high in the Rockies and then gently slopes downward in the Western Sedimentary Basin and the Canadian Shield until it reaches the lowest elevation point near James Bay at x = 1.6×10^6 m, where a thin sedimentary basin outcrops. The topography then rises again and slopes downward in the St-Lawrence River region, at the interface between the Shield and the Appalachians. Finally, the Chic-Chocs range appears followed by the low-elevation sedimentary rocks that gently slope toward the Atlantic Ocean. The western part of the cross section is nearly coincident with a groundwater flow line in which groundwater flows by westward gravity from the Rockies to the Pacific Ocean and to the east in the Interior Plains (Figure 6.16a). In the eastern part of the section, there is a general movement from the higher elevations of the Shield in Quebec, towards James Bay and the St-Lawrence River, and then from the Chic-Chocs to the St-Lawrence and to the Gulf. The TDS trend with depth is similar to that in the two previous sections (Figure 6.17a) and a thin layer of permafrost affects the provinces of Manitoba, Ontario and Quebec as well as the Rockies and the Chic-Chocs (Figure 6.18a).

From the last interglacial at -120 kyr to the first time slice at -30 kyr, the ice sheet progressively migrated southward as well as the permafrost zone; the ice sheet covers the permafrost, however, as it advances. This situation is shown in Figure 6.12b. It can be seen that below the northern part of the main ice sheet, the permafrost has melted since the LIG and windows of thawed rock are now in contact with the ice sheet. These windows of unfrozen materials allow the subglacial meltwater to

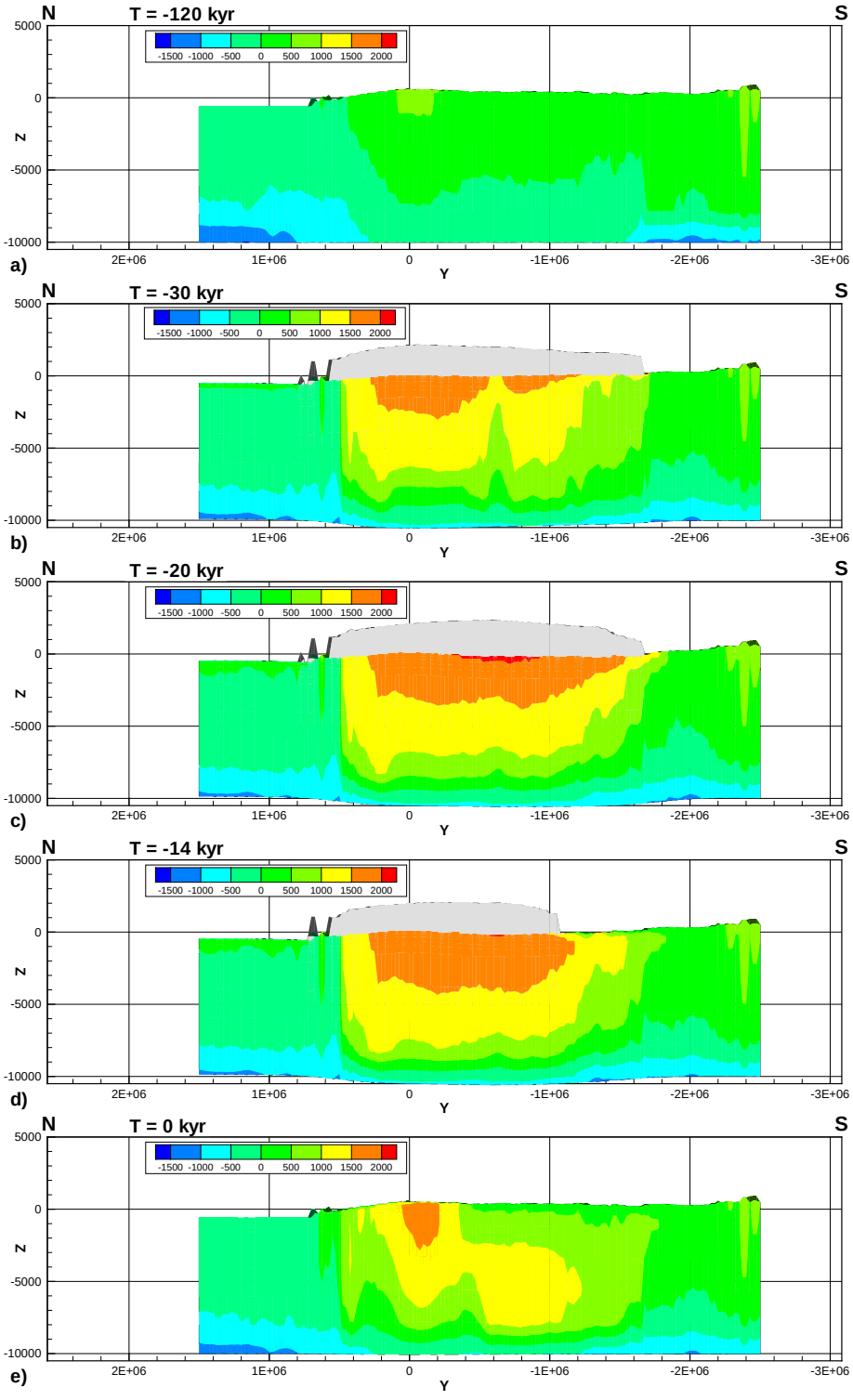

Figure 6.13: Hydraulic head along a cross section located at $x = 2.14\times10^6$ m at selected time slices: a) -120 kyr; b) -30 kyr; c) -20 kyr; d) -14 kyr and e) 0 kyr. Vertical exaggeration: 100×.

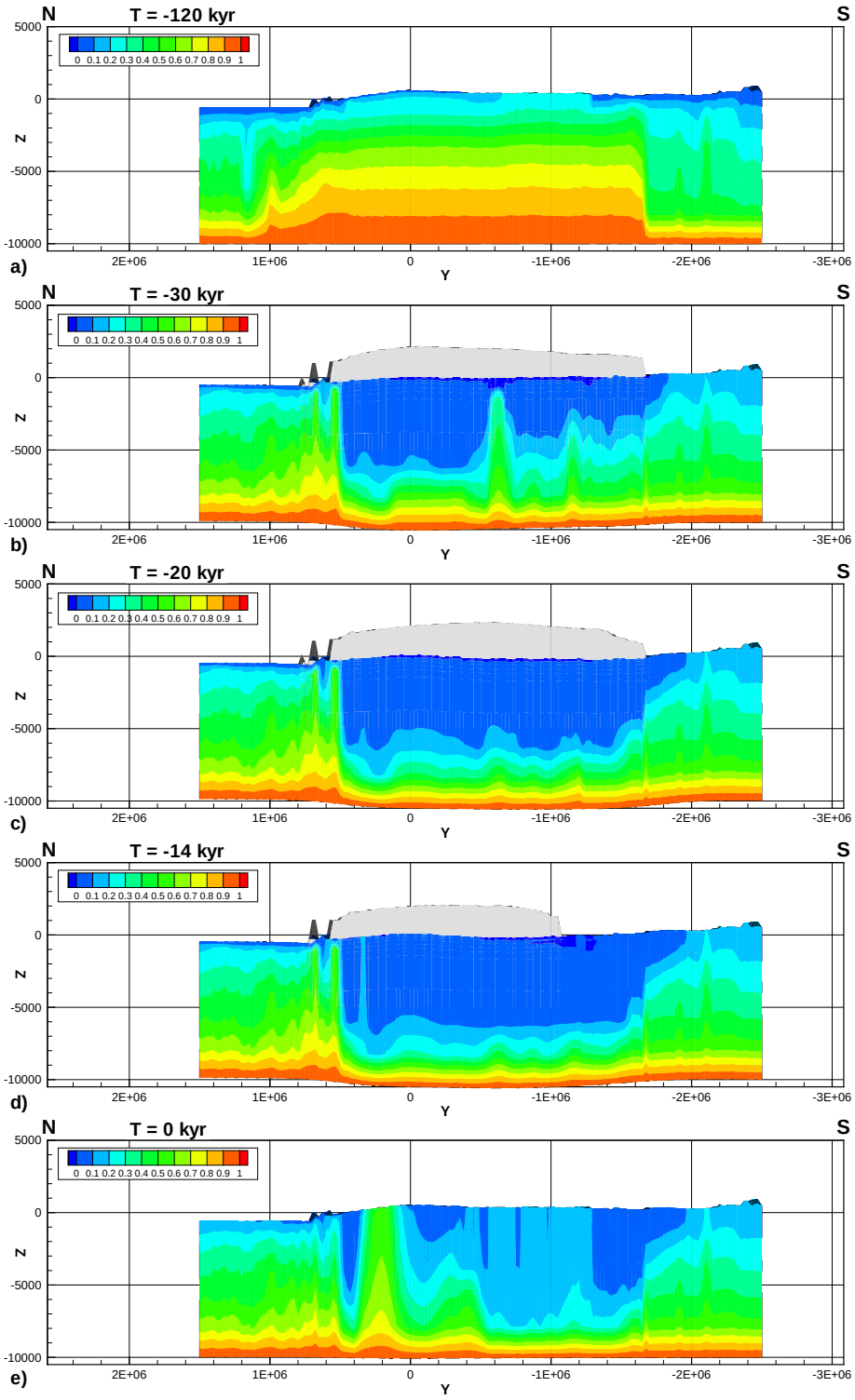

Figure 6.14: Relative concentration (C/C_{max}) along a cross section located at $x = 2.14\times10^6$ m at selected time slices: a) -120 kyr; b) -30 kyr; c) -20 kyr; d) -14 kyr and e) 0 kyr. Vertical exaggeration: 100×.

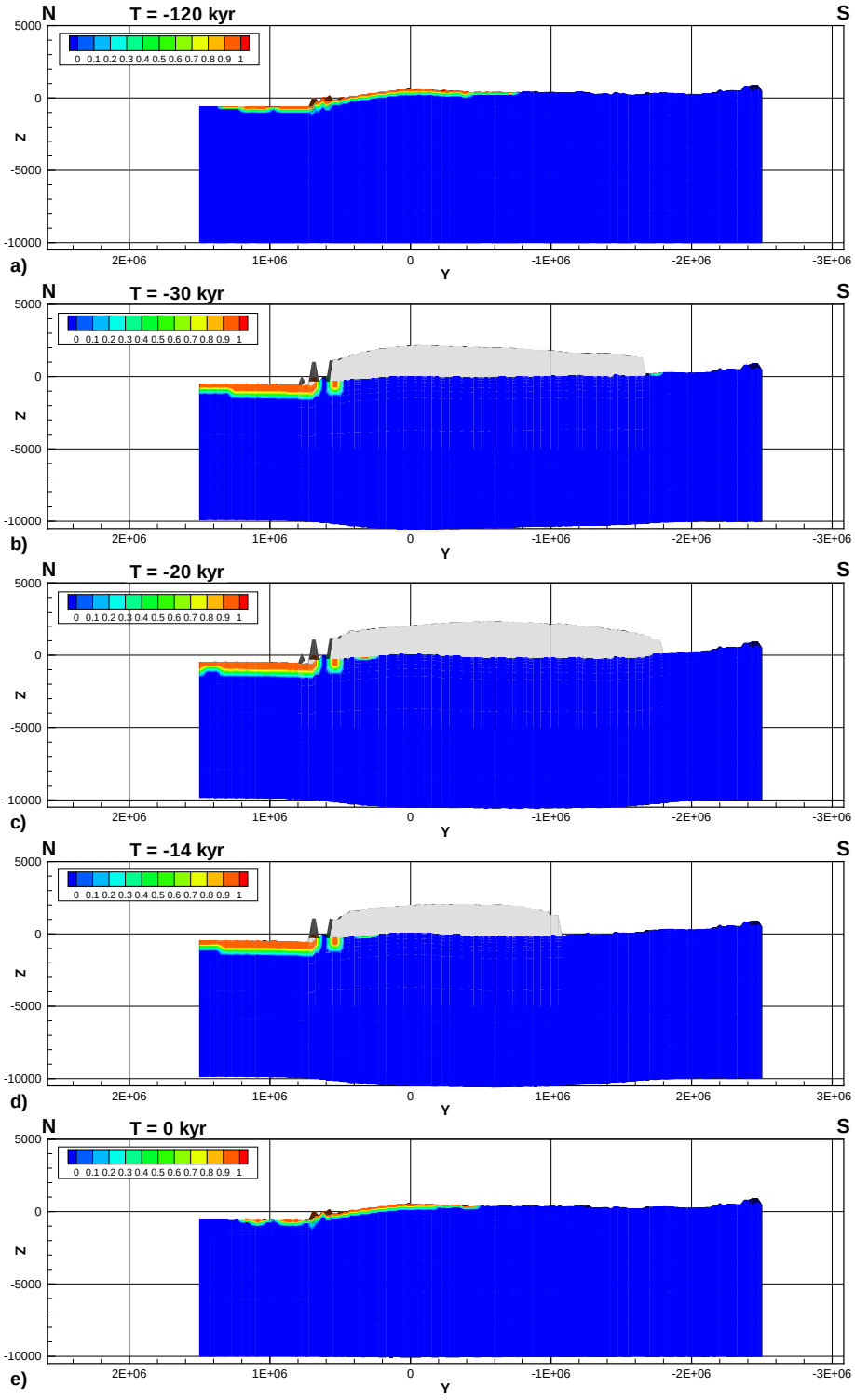

Figure 6.15: Permafrost along a cross section located at $x = 2.14{\times}10^6$ m at selected time slices: a) -120 kyr; b) -30 kyr; c) -20 kyr; d) -14 kyr and e) 0 kyr. Vertical exaggeration: 100×.

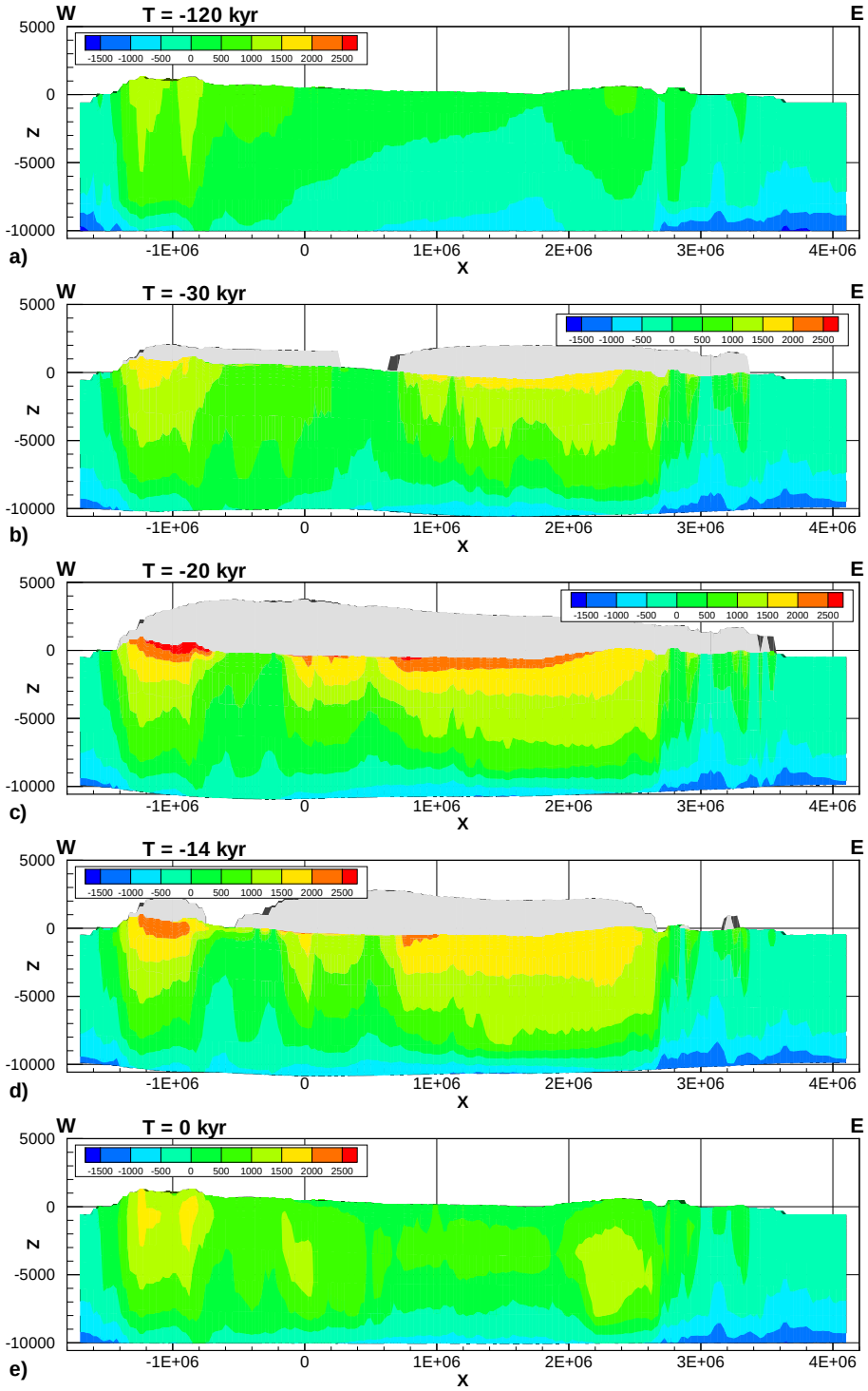

Figure 6.16: Hydraulic head along a cross section located at y = -4.63×10^5 m at selected time slices: a) -120 kyr; b) -30 kyr; c) -20 kyr; d) -14 kyr and e) 0 kyr. Vertical exaggeration: 100×.

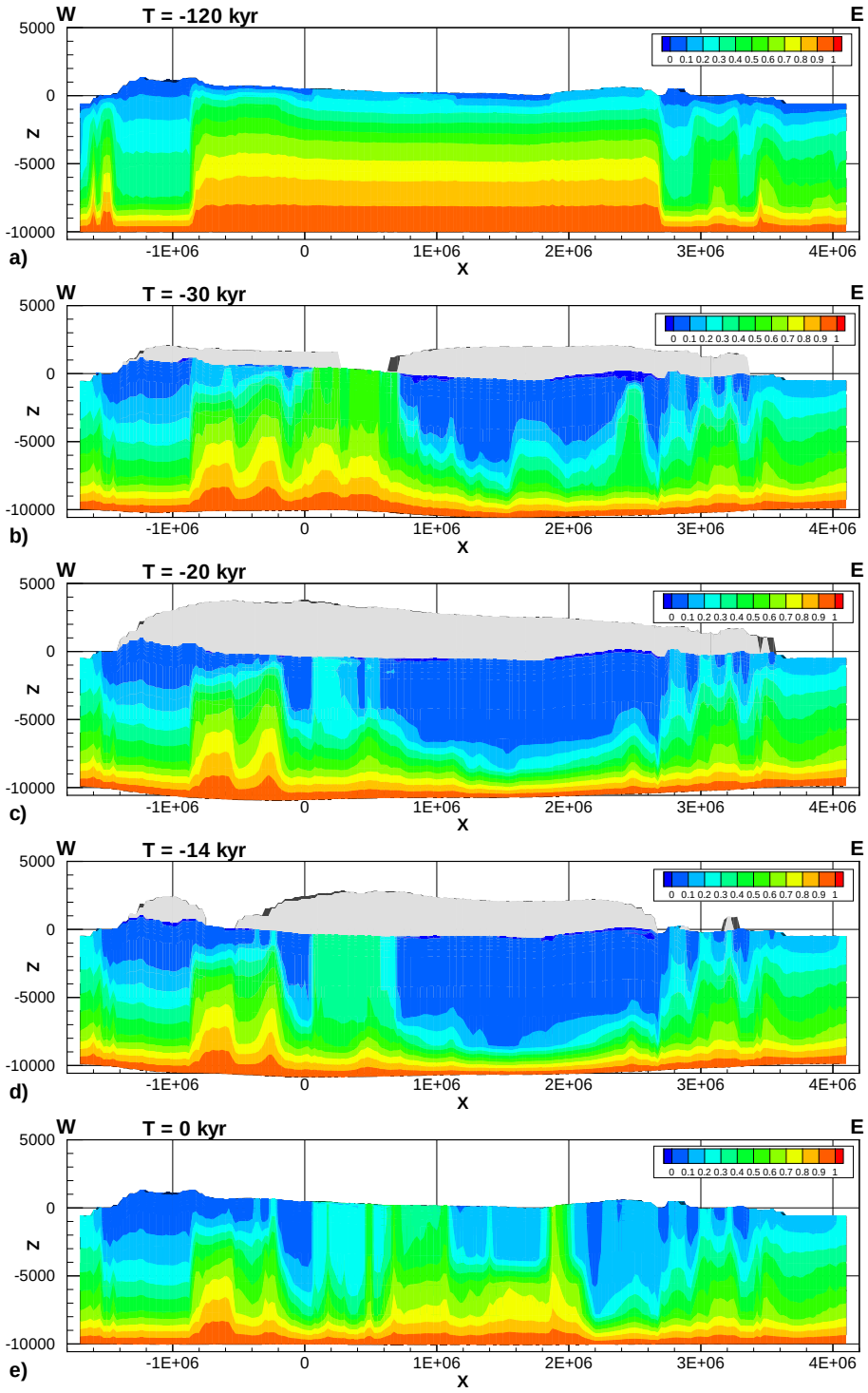

Figure 6.17: Relative concentration (C/C_{max}) along a cross section located at y = -4.63×10^5 m at selected time slices: a) -120 kyr; b) -30 kyr; c) -20 kyr; d) -14 kyr and e) 0 kyr. Vertical exaggeration: 100×.

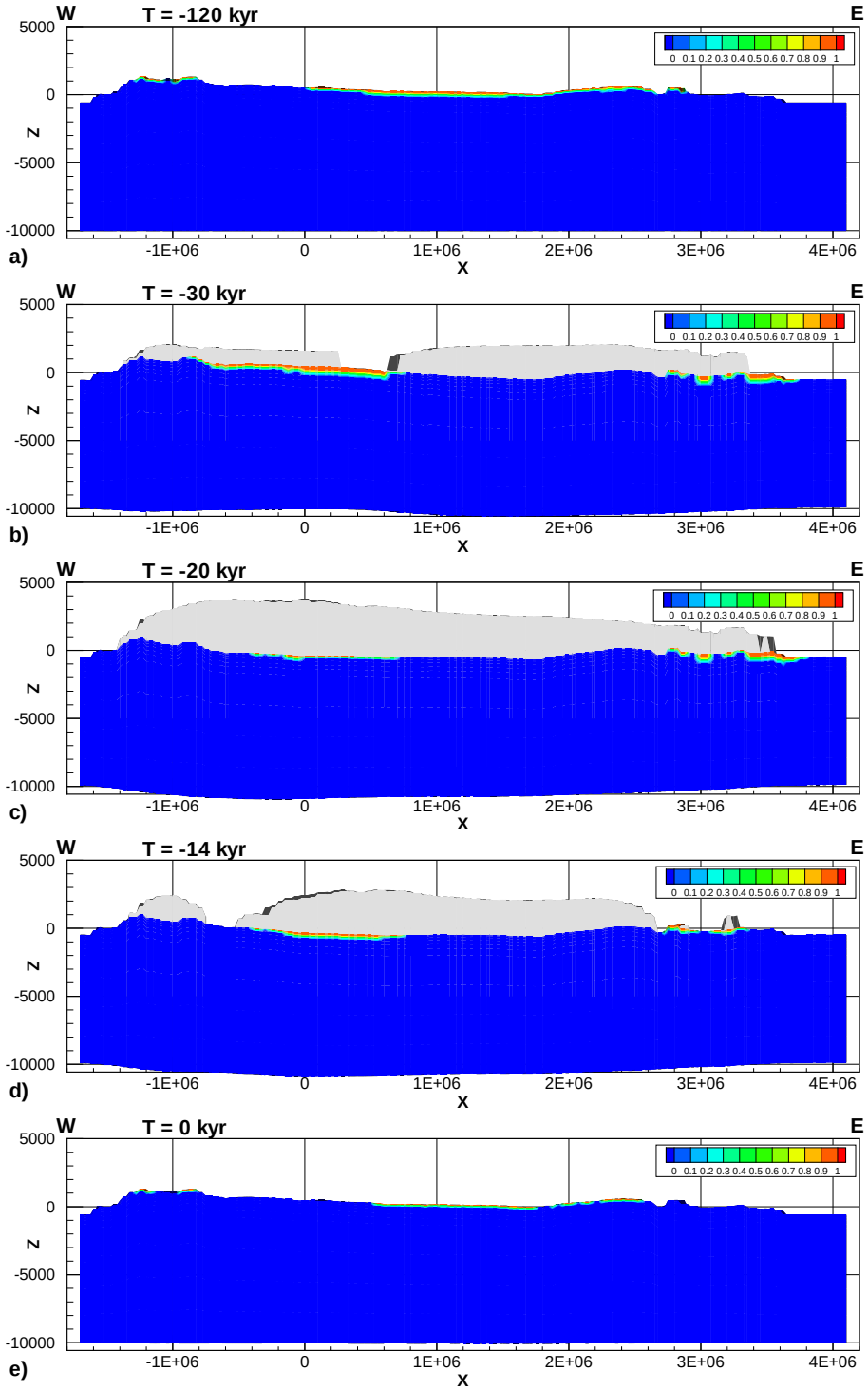

Figure 6.18: Permafrost along a cross section located at y = -4.63×10^5 m at selected time slices: a) -120 kyr; b) -30 kyr; c) -20 kyr; d) -14 kyr and e) 0 kyr. Vertical exaggeration: 100×.

infiltrate into the subsurface and increase the hydraulic head and dilute the TDS (Figures 6.10b and 6.11b). The hydraulic head is also rising everywhere under the ice sheet due to glacial ice loading.

This situation is even more evident upon looking at the second cross section located at $x = 2.14 \times 10^6$ m. The thin layer of permafrost that was affecting the northern part of the cross section at LIG has melted almost completely as the ice sheet covered it at -30 kyr (Figure 6.15b). The hydraulic head increases dramatically as the subglacial meltwater infiltrates into the subsurface (Figure 6.13b); the hydraulic head at a depth of up to 3000 m reaches a value of more than 1500 m under the main ice dome. The meltwater infiltration into the subsurface also has a dramatic impact on the solute distribution at depth as two major regions of TDS dilution exist under the ice sheet (Fig 6.14b).

On the third cross section (east-west) located at $y = -4.63 \times 10^5$ m, the evolution of the permafrost from the LIG to -30 kyr shows that the thin permafrost layer that was present near ground surface has almost completely melted under the eastern part of the ice sheet while it has thickened in the western portion (Fig 6.18b). The subglacial meltwater infiltrates into the subsurface where there is no permafrost and the hydraulic head increases accordingly (Fig 6.16b). The subglacial region where meltwater infiltration occurs undergoes significant solute dilution below the ice sheet (Fig 6.17b).

At -20 kyr, which is close to the last glacial maximum, the subglacial groundwater environment has further evolved and is even less affected by permafrost than before. Most of the subglacial environment is open for subglacial meltwater infiltration and the hydraulic head increases consistently, which can be seen in all three cross sections. Consequently, with the penetration of subglacial meltwater into the subsurface, the solute concentration diminishes. At this point, the groundwater flow patterns that

are depicted on the three cross sections are drastically different than those of the last interglacial. This major difference is clear evidence of the large impact that the ice sheet had on groundwater flow and the brine distribution.

Following LGM, the ice sheet begins to retreat northward. At -14 kyr, the groundwater flow system and solute concentration distribution are still similar to those existing at -20 kyr; however, after about -14 kyr the ice sheet retreated rapidly and surface conditions changed dramatically. After the complete retreat of the ice (0 kyr), it can be seen on each cross section that the high hydraulic heads that developed at depth under the ice sheet have diminished although the values are higher than at LIG. Several over-pressurized zones can be seen at depth as evident in Figure 6.16e, or even near the surface (Figure 6.13e). The reason for the existence of the shallow zones of high pressures is because the permafrost re-appeared on the surface, after the glacial retreat, before the high hydraulic heads could dissipate (Figure 6.15e). The solute concentration patterns at the end of the glacial cycle are also more heterogenous that at LIG.

It can be noted from the cross sections that low hydraulic heads appear at the bottom sides of the model. It would be expected that the heads at these locations be higher, and similar to the heads in the remainder of the cross sections at the same depth. It was found that these abnormally low heads originate from the LIG quasi steady-state simulation that was used to generate the initial conditions for the glacial cycle simulation. The time steps selected for the LIG simulation were much larger (1 kyr) than those used during the glacial cycle simulation (0.1 kyr), because the model required a long time frame to reach quasi steady state (1.2 Myr). Moreover, a fully-explicit formulation was used to update the solute concentrations. These two reasons, which helped to speed the computation time, yielded numerical instabilities in some of the largest elements, which are located at the bottom of the model. During

the glacial cycle, the time steps are smaller and therefore, the numerical oscillations did not occur.

The impact of the presence of these low hydraulic heads at depth on the shallow groundwater flow system and on the exchange fluxes will be minor during the glacial cycle as their position and values remain the same over the duration of the simulation, suggesting that they do not evolve and interact much with the ambient flow system. Moreover, they are located in regions of the model not affected by the ice sheet, where the permeability is very low and the density of the water is high.

6.2 Sensitivity to the Loading Efficiency Parameter

Because no values of the loading efficiency parameter, ζ, are available in the literature for the various rock types at a regional scale, the value used in the base-case scenario ($\zeta = 0.2$) is now varied to capture its influence on the evolution of the groundwater flow system. Two new cases are considered using values equal to 0.0 and 1.0.

Figure 6.19 shows the hydraulic head evolution for all three cases at the observation point located at Edmonton. With regard to the impact of the loading efficiency parameter on the hydraulic head evolution (Figures 6.19a, 6.19b and 6.19c), it can be seen that greatest difference between the cases occurs at large depths. When the loading efficiency parameter is zero, the head perturbation at depth is mainly the result of the change in the surface elevation due to isostasy as can be noted from Figure 6.19b. When the loading efficiency parameter is increased, the hydraulic head at depth becomes larger during ice sheet progression than it does with $\zeta = 0.0$. Near the surface, the head does not change as much, because it is affected to a greater degree by the infiltration of subglacial meltwater. For the case where $\zeta = 1.0$, the

head increases similarly at all depths (Figure 6.19c) such that the vertical hydraulic gradient does not change much with time. This is confirmed by the low Darcy flux values for $\zeta = 1.0$ through time (Figure 6.19d).

The ice-sheet weight is transferred to the fluid with a magnitude related to the loading efficiency parameter. The main driving force for groundwater flow is the meltwater infiltration if the effect of ice loading is neglected. This occurs when $\zeta = 0.0$ and large hydraulic gradients develop between the surface and groundwater zones at depth. When the loading efficiency equals unity, all of the ice weight is transferred directly and equally to the fluid at all depths. In this case, the hydraulic head difference between the surface and at depth is much lower such that meltwater infiltration into the subsurface will be reduced.

6.3 Permafrost Impact on the Groundwater Flow System

In order to capture the importance of permafrost on the evolution of the groundwater flow system during the last glacial cycle, the base-case scenario was modified to neglect permafrost as was previously mentioned in Chapter 5. This case, when compared to the base case, was considered to highlight the role played by the permafrost on surface/subsurface water interaction.

One striking aspect of the simulation results, however, is that the neglect of the permafrost does not seem to significantly modify the flow system during the glacial cycle. This can be seen by comparing Figures 6.20 (no permafrost) and 6.13 (with permafrost). Because the permafrost acts like a barrier to surface/subsurface water interaction, it would have been expected that its neglect would have exposed a much larger area for subglacial meltwater infiltration, and therefore significantly

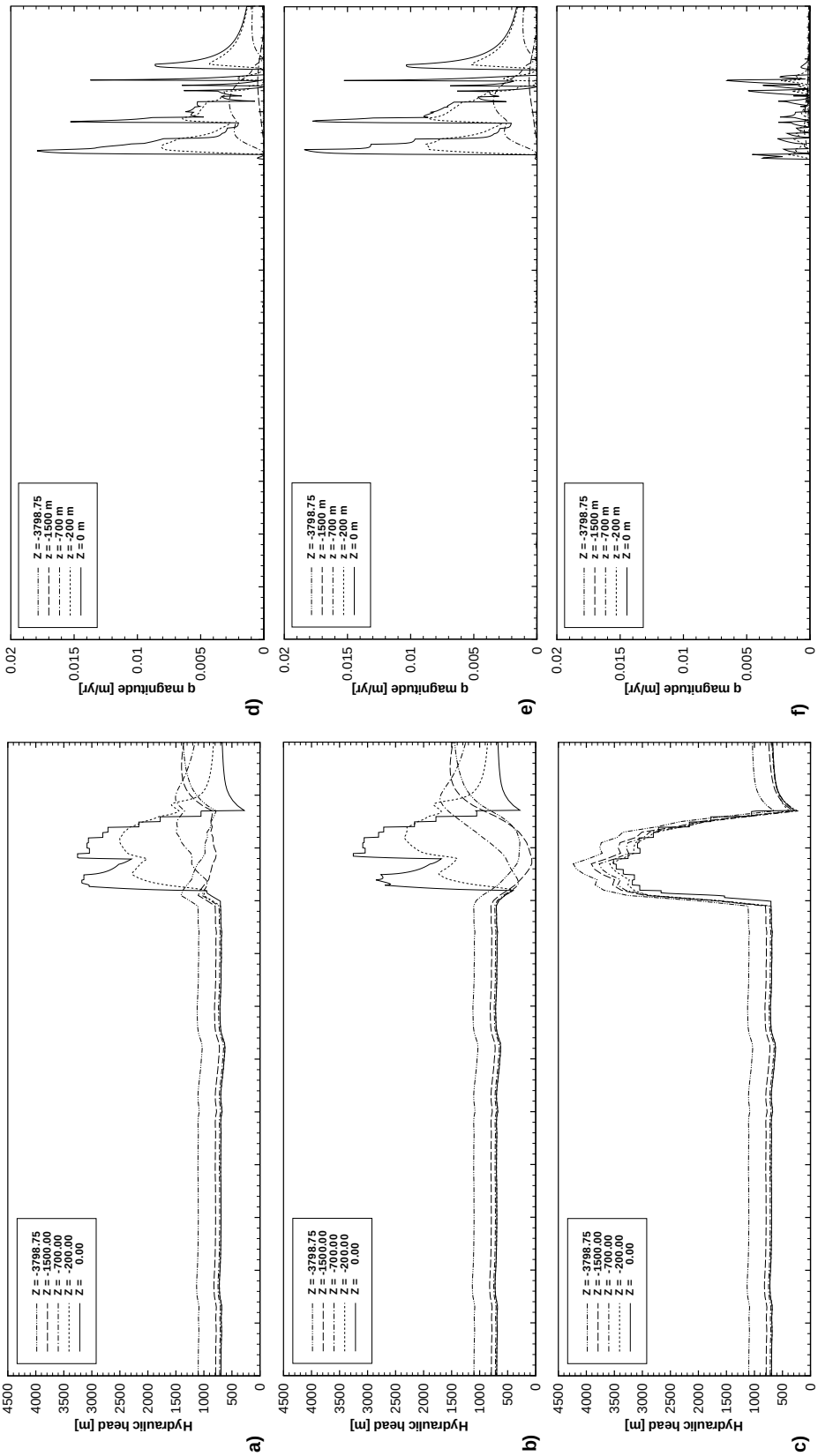

Figure 6.19: Hydraulic head and Darcy flux magnitude for an observation point located at Edmonton, AB, for cases where the loading efficiency parameter changes. a) Hydraulic head versus time for the base case. b) Hydraulic head versus time for $\zeta = 0.0$. c) Hydraulic head versus time for $\zeta = 1.0$. d) Darcy velocity magnitude versus time for the base case. e) Darcy velocity magnitude versus time for $\zeta = 0.0$. f) Darcy velocity magnitude versus time for $\zeta = 1.0$.

increased the infiltration. It was shown in the previous chapter, however, that infiltration does not increase when the permafrost is neglected. Subglacial meltwater is produced mainly under the warm-based region of the ice sheet and rarely in cold-based subglacial zones where permafrost is present. Therefore, even if the permafrost is neglected, there is little or no subglacial meltwater available to infiltrate into the subsurface.

It was shown on Figure 6.20e that, at the end of the simulation period, the permafrost had trapped a high pressure zone at depth because it could not dissipate by vertical flow to the surface where the head is lower. It can be seen by comparing Figure 6.20e (no permafrost) with Figure 6.13e (with permafrost) that, although an over-pressurized zone remains at depth for the no-permafrost case, it has a lower peak and high heads are not trapped near the surface. The occurrence of a trapped high-pressure zone below the permafrost at the end of the glacial cycle highlights the importance of the permafrost to control the recovery of the flow system after a glacial cycle. The presence of taliks, as currently observed at high latitudes, might dissipate the high-pressure zones and their inclusion in a model may be important in order to correctly reproduce observed hydraulic head patterns.

The effect of neglecting the permafrost on the solute concentration distribution in the subglacial and periglacial environments will now be examined. A large part of the Canadian land surface was affected by thick permafrost at LIG that prevented surface/subsurface water interactions. During the glacial cycle, however, several of these locations became frost-free. Figure 6.21 shows the computed solute concentration along the cross section at $x = 2.14\times10^6$ m at present time without permafrost, and can be compared with the base-case results shown in Figure 6.14e to illustrate any changes in the solute concentration distribution. Overall, there is a striking similarity in the concentration patterns between the two cases for present time; however, as

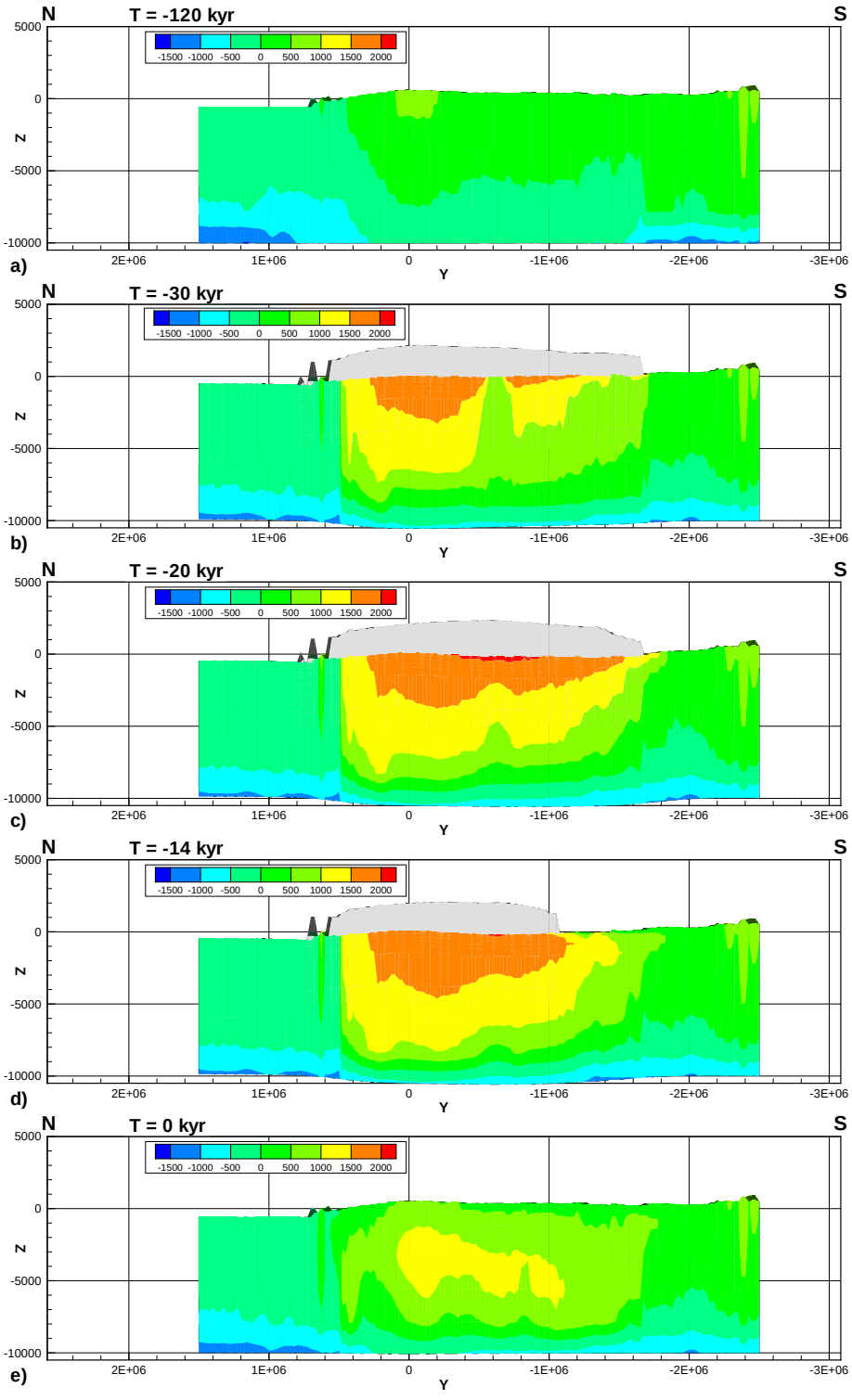

Figure 6.20: Hydraulic head for a case neglecting permafrost along a cross section located at $x = 2.14 \times 10^6$ m at selected time slices: a) -120 kyr; b) -30 kyr; c) -20 kyr; d) -14 kyr and e) 0 kyr. Vertical exaggeration: 100×.

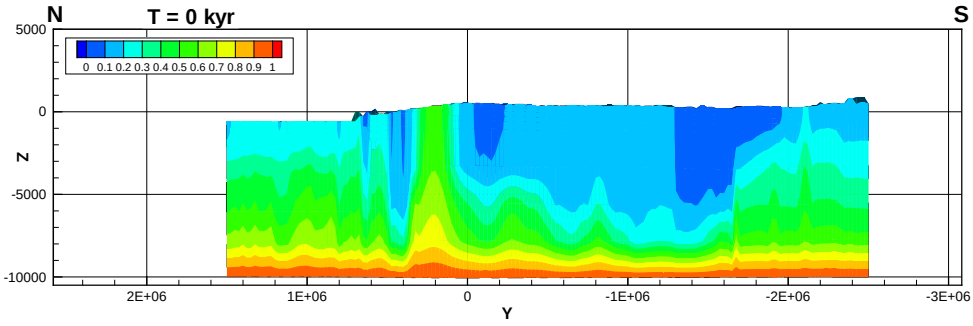

Figure 6.21: Solute concentrations for a case neglecting permafrost along a cross section located at $x = 2.14\times10^6$ m at present time (0 kyr). Vertical exaggeration: 100×.

discussed in Section 6.1, the inclusion of salt rejection during permafrost formation, a process not represented in the model, would likely produce significant differences between cases with and without permafrost.

6.4 Summary

In this chapter, a coupled, fully-transient glacial-cycle and groundwater flow model accounting for density-dependant solute transport was used to address the impact of the Wisconsinian glaciation on continental groundwater flow. The simulated TDS concentrations were compared to currently available TDS observations. Although the general trend of the increase in concentration values at depth is captured, the model fails to reproduce the shallow depth variation of TDS concentrations. It is believed that inclusion of the phenomenon of salt expulsion from freezing water in the model during permafrost penetration would ameliorate this discrepancy.

During the last glacial cycle, the ice sheet advanced and retreated several times to form three local glacial maxima. Each of these glacial advances had a different impact on groundwater flow because of their different intensities and durations. Their relative impact on flow system behaviour follows the same sequence as their timing,

with the first being the least important and the last one being the most significant. The last glacial advance was of the longest duration and produced the thickest ice sheet.

The impact of the ice sheet on groundwater flow was shown to be dramatic. Hydraulic head values below the ice sheet increased by as much as 3,000 m down to a depth of 1.5 km into the subsurface. At present time, large over-pressurized zones should still be observed at depth because very long time frames are required to dissipate the large pressures at large depths. The increase in the hydraulic head is attributed to the infiltration of subglacial meltwater into the rocks and because of the surface loading induced by the ice sheet. During a glacial cycle, vertical hydraulic gradients can reverse depending on the location relative to the ice sheet margin, and the magnitude of the Darcy flux can vary in time by as much as two orders of magnitude at depths of 700 m and greater. The distribution of the TDS concentrations were highly modified and large lenses of reduced concentration appeared at some locations. This is because pulses of low-TDS subglacial meltwater infiltrated to depths greater than a kilometer in some areas.

The ice sheet weight is transferred to the fluid with a magnitude related to the loading efficiency parameter. By varying the value of the loading efficiency parameter, it was shown that the hydraulic head difference between the surface and at depth becomes smaller as the loading efficiency parameter increases. The hydraulic head at depth becomes much higher with a large value of the parameter, whereas, near the surface, the changes in head is influenced to a greater degree by the flow boundary conditions imposed at the surface (*e.g.*, the rate of meltwater infiltration).

Significant differences were noted between the meltwater infiltration rates occurring in sedimentary basins than in the Canadian Shield. For the sedimentary rocks, the subglacial environment produces hydraulic heads that are often lower than the

ice-sheet equivalent freshwater head compared to the case of the Shield rocks. The differences in infiltration rates between the two types of rocks mainly occur during ice-sheet buildup, but vanish during ice-sheet retreat. Overall, this conclusion suggests that subglacial runoff water was more abundant over the Shield rocks than over the sedimentary rocks.

The neglect of permafrost in the model does not appear to significantly modify the flow system during the glacial cycle, at least, in subglacial zones. This is because subglacial regions affected by permafrost do not produce meltwater, such that, when the permafrost is ignored, no change in subglacial infiltration occurs. On the other hand, the permafrost has a large impact on the rate of dissipation of high hydraulic heads that build at depth as a consequence of subglacial infiltration and ice loading; the permafrost forms a cap on the surface which inhibits the pressure dissipation process. The occurrence of a trapped pressure zone below the permafrost after a glacial cycle highlights the importance of the permafrost distribution on the recovery of the flow system. The presence of taliks, as currently observed at high latitudes, could enhance the rate of dissipation of these high pressure zones in the model.

Based on the hydraulic head and TDS concentration results after the last glacial cycle, it was shown that the flow system did not fully revert to its initial LIG condition, and that it is still recovering from the LGM perturbation. This suggest that the current groundwater flow system cannot be interpreted solely on the basis of present-day boundary conditions and it is likely that several thousands of years of additional equilibration time will be necessary for the system to reach a new quasi-steady state. This further implies that use of the steady-state assumption to simulate a time-slice of the impact of glaciation on large-scale groundwater flow is inappropriate.

Chapter 7

Groundwater Age Distribution

"Our ignorance is not so vast as our failure to use what we know."

M. King Hubbert

Groundwater age is defined as the time elapsed since the water infiltrated in a recharge zone. Groundwater age is a measure of the residence time of water in the subsurface and can be used to track the infiltration history of an aquifer. Groundwater age can be measured using environmental isotopes and be used as a benchmark for model validation. As a final contribution to the thesis, groundwater age distributions will be computed for the last interglacial and its evolution through the last glacial cycle as a consequence of subglacial infiltration.

7.1 The Concept of Groundwater Age

Cornaton [2004] presents a detailed review of the concept of groundwater age and the following introduction is inspired by his review. Water enters into the ground through an infiltration process and it becomes groundwater when it leaves the surface to enter the subsurface. Each water molecule enters the subsurface at different times. A

zero age is usually assigned to molecules that enter the system at the inlet limits. Groundwater age is therefore defined as the time elapsed since the water infiltrated in a recharge zone.

Water circulates in the subsurface and, depending on the spatial structure of the geologic materials and the boundary conditions, it can follow different flow paths. Some flow paths may be short and shallow, but others may produce deep circulation patterns in the subsurface that will require a long period of time before discharging to the surface. The length of the flow path and the time elapsed since the water entered the subsurface will also affect the water chemistry. Modelling groundwater age is equivalent to simulating the transport of conservative substances in groundwater. It is also analogous to tracking particles in a flow system by advective and dispersive processes.

Because age is a property that is transported in groundwater by advection and dispersion, mixing caused by the heterogeneity of the physical flow parameters (*i.e.*, hydraulic conductivity) and by the process of molecular diffusion will induce a heterogeneous distribution of ages. Groundwater age should therefore be viewed in a probabilistic framework rather than as a single value at each point in space and time.

7.2 The Computation of Mean Groundwater Age

Cornaton and Perrochet [2006] showed that the statistical distribution of the random variable groundwater "age" can be modelled using a formulation based on advective-dispersive transport of a conservative tracer, using appropriate boundary conditions. The age probability density function is obtained for a finite reservoir, Ω, by solving

the boundary value problem:

$$\frac{\partial \phi g_A}{\partial t} = -\nabla \cdot \mathbf{q} g_A + \nabla \cdot \mathbf{D} \nabla g_A + q_I \delta(t) - q_O g_A \tag{7.1}$$

in which:

$$g_A(\mathbf{x}, 0) = g_A(\mathbf{x}, \infty) = 0 \quad \text{in } \Omega, \tag{7.2}$$

$$\mathbf{J}_A(\mathbf{x}, t) \cdot n = (\mathbf{q} \cdot n)\, \delta(t) \quad \text{on } \Gamma_- \tag{7.3}$$

where $g_A(x,t)$ is the transported age pdf, $\mathbf{D}$ is the macrodispersion tensor, $\mathbf{J}_A(x,t)$ is the total age mass flux vector, $\mathbf{x} = (x, y, z)$ is the vector of Cartesian coordinates, n is a normal outward unit vector, and $\delta(t)$ is the Dirac delta function which ensures an impulse flux on Γ_-. Γ_- represents the inlet boundaries and Γ_+ refers to the outlet boundaries. The terms q_I and q_O represent fluid sources and sinks, respectively, such as the internal production or extraction of groundwater. The total age mass flux vector $\mathbf{J}_A(x,t)$ is defined by the sum of the advective and dispersive fluxes:

$$\mathbf{J}_A(\mathbf{x}, t) = \mathbf{q} g_A(\mathbf{x}, t) - \mathbf{D} \nabla g_A(\mathbf{x}, t) \tag{7.4}$$

The mean value $\langle A \rangle$ of the probability density function g_A is defined by its first temporal moment:

$$\langle A \rangle = \int_{-\infty}^{+\infty} u g_A(\mathbf{x}, u)\, du \tag{7.5}$$

where u is the age value. The first moment form of Eqn. 7.1 is the mean age transport equation in which the mean age is defined as the average over a water sample containing water molecules having a range of individual ages. It is given by:

$$-\nabla \cdot \mathbf{q} \langle A \rangle + \nabla \cdot \mathbf{D} \nabla \langle A \rangle - q_O \langle A \rangle + \phi = 0 \quad \text{in } \Omega \tag{7.6}$$

The mean groundwater age can be computed by prescribing a "concentration" input that is proportional to the water flux at the inflow boundaries. Eqn. 7.6 can be solved by assigning $\langle A \rangle = 0$ on the inlet limits. Mean age is continuously generated during groundwater flow, since porosity acts as a source term. This source term indicates that groundwater is aging at the rate of one unit per unit time, on average. Cornaton and Perrochet [2006] show that mean age computations using Eqn. 7.6 are well-suited for simulating isotopic age dates. The implementation of mean age calculations is straightforward in a numerical model that already solves the advection-dispersion equation because only a source term that equals the porosity needs to be included [Voss and Provost, 2001; Cornaton and Perrochet, 2006], as well as the use of proper boundary conditions ($\langle A \rangle = 0$ at Γ_-).

For information purposes, another useful variable seldom used in practice is the mean groundwater life expectancy, defined as the average time required for a particle of water to reach an outlet. The computation of mean life expectancy is performed in a similar fashion to that for the mean age, but the flow field is reversed. The summation of the life expectancy and the groundwater age yields the mean transit time, which is the time required for a particle that enters the subsurface to reach an outlet.

7.3 Demonstration

In order to illustrate the groundwater mean age concept, a simple numerical example was constructed. Figure 7.1a shows a cross section along a sandy aquifer that is 100 m long and has a thickness of 50 m on which a linear head function is applied over the surface. The sides and bottom of the model are no-flow boundaries. The properties of the sandy aquifer are given in Table 7.1 and the free-solution diffusion coefficient

Table 7.1: Hydraulic properties of the sandy aquifer.

Variable	Value
Hydraulic conductivity, K_{ij}, [m/d]	6.426
Porosity, ϕ, [-]	0.375
Longitudinal dispersivity, α_L, [m]	1.0
Transverse dispersivity, α_T, [m]	0.1

was set to zero. The steady-state flow field is displayed in Figure 7.1a. Groundwater recharges on the upper right portion of the aquifer where the hydraulic heads are high and discharges to the upper left where the heads are lower. The flow paths are short and shallow in the upper middle portion of the aquifer and are much longer and deeper when originating from upland recharge zone. It should be expected that the mean groundwater age distribution will follow this trend in flow path lengths.

For the steady-state computation of mean groundwater age, a third-type (Cauchy) boundary condition equal to zero is applied on the top face of the model. The third-type boundary condition ensures that the infiltrating water has an age of zero. The mean age solution is shown in Figure 7.1b. It can be seen that the groundwater is younger in the upgradient recharge portion of the aquifer and becomes older towards the outlet. The oldest groundwater is found on the lower left corner, with an age about 300 days.

For the life expectancy solution, the flow field was reversed and the solution is given in Figure 7.1c. The mean life expectancy is in this case a mirror image of the mean age because the flow field is symmetric and because the solutions are complementary. Finally, Figure 7.1d shows the mean transit time of water in the aquifer.

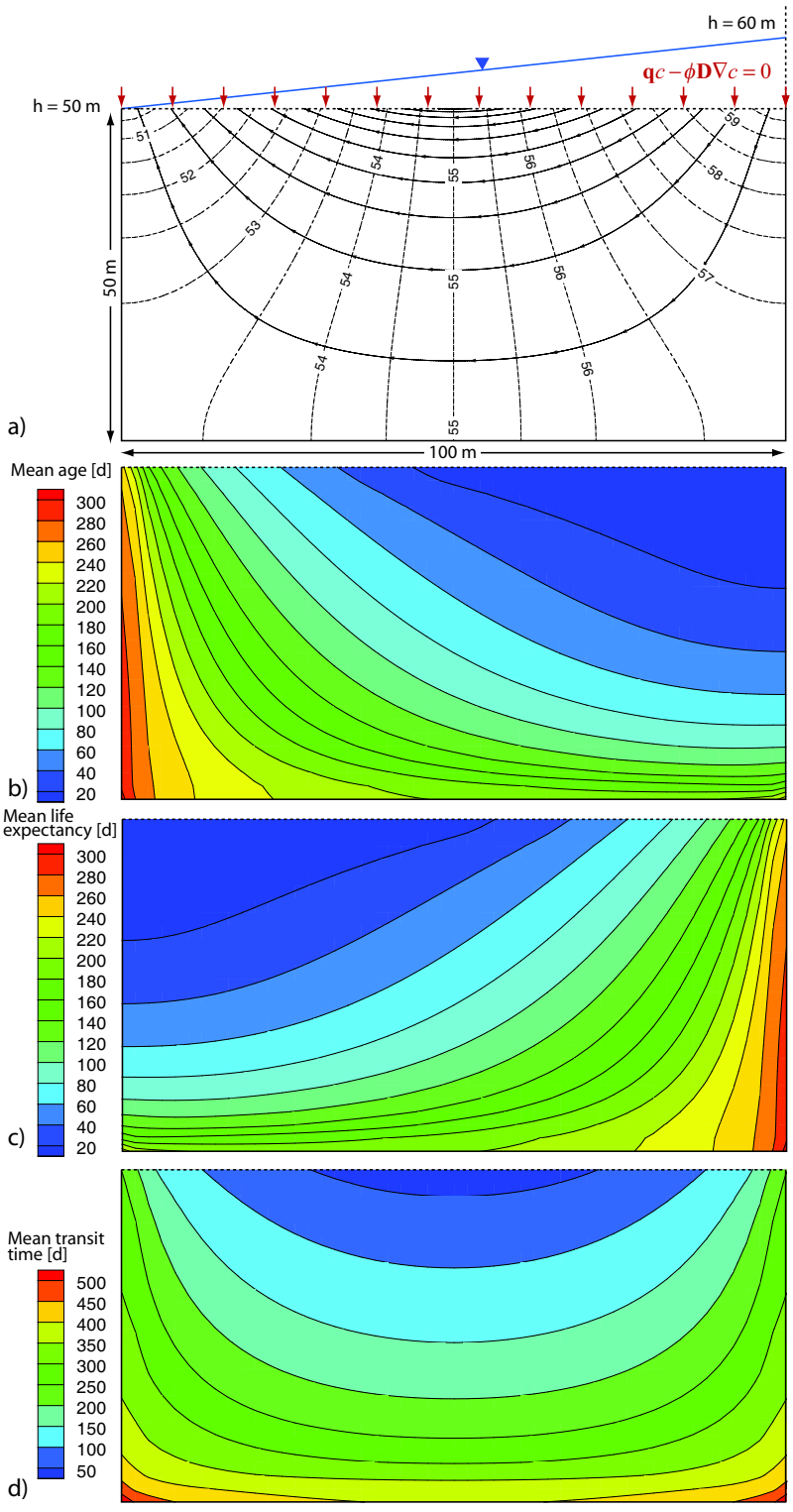

Figure 7.1: Steady-state solution for a) Hydraulic head (dashed lines) and streamlines along with boundary conditions, b) Mean age, c) Mean life expectancy and d) Mean transit time.

7.4 Mean Groundwater Age Distribution at Last Interglacial

Once again, in order to perform the age calculation during the last glacial cycle, initial conditions are needed for the age distribution at LIG. In order to obtain the mean groundwater age distribution at LIG, the flow field obtained for the LIG is as described in Section 4.3 and a steady-state age transport simulation was performed. The age transport boundary condition consist of a specified zero age at inflow nodes and a zero-order source term equal to the porosity for each of the rock facies was used. The calculated mean groundwater age pattern over the top surface of the model at LIG is given in Figure 7.2a and along select cross sections in Figure 7.2b.

The only clear pattern that appears at this scale is that the mean groundwater age at LIG is younger near the surface and older with depth. The mean groundwater ages span a very large range in values, ranging from zero to 42 Myr. A value of 42 Myr occurs at great depth where there is little groundwater flow. Inspection of the results along the cross sections (Figure 7.2b) reveals that the youngest water occupies a relatively thin veneer near the surface. Because of the large density of the groundwater at depth, where there is little flow, a large mass of essentially stagnant groundwater exists in the bottom portion of the model.

The surface distribution of the mean groundwater age shows that most of the shallow water has a young age, which suggest that water has just entered the system. A few locations, mainly along the coast of the province of Québec, Baffin Island and the north shore of Nunavut, show older water. They represent groundwater discharge regions and the age at the outlet is a mixture of deep old water and shallow, younger water.

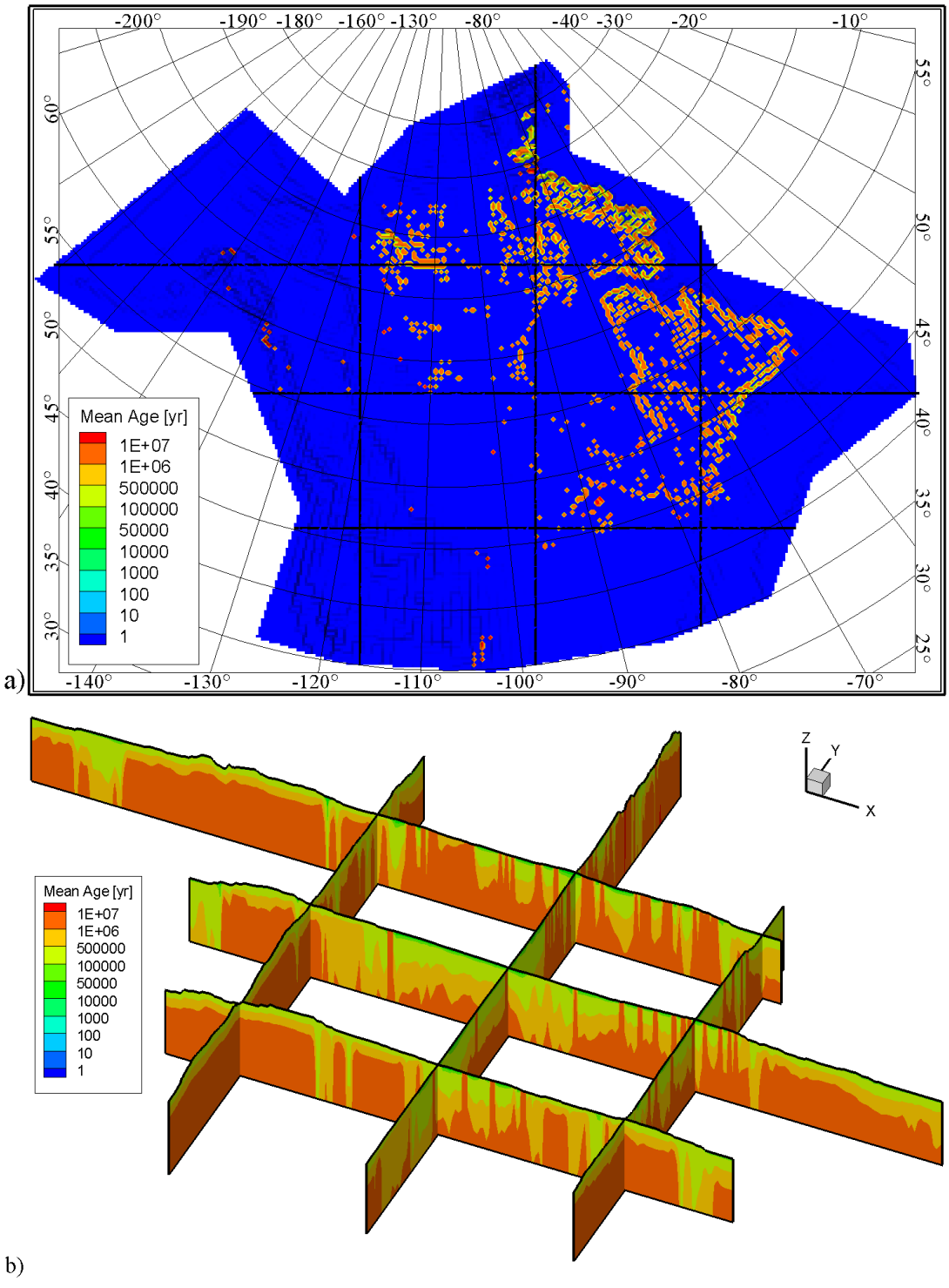

Figure 7.2: Mean groundwater age distribution a) over the model's surface at LIG and b) along selected cross sections. Vertical exaggeration in b) is 60×.

7.5 Mean Groundwater Age Evolution During the Wisconsinian Glaciation

The mean groundwater age was computed during the glacial cycle for the base case described in Chapter 4. The age boundary conditions are a specified zero age at inflow nodes, both in the subglacial and periglacial environments (Table 4.5). Figure 7.3 shows the evolution of the mean groundwater age at the same observation points selected in Chapter 6. It can be seen that the shape of the curves are similar to those of the TDS curves, with the difference being that the age curves are gently rising constantly. The times at which the mean age decreases is related to the infiltration of meltwater into the subsurface. The mean age values increase significantly with depth and can exceed 1.0 Myr below a depth of about 3800 m (Figure 7.3b). It can be seen that, at the end of the glacial cycle, the mean groundwater age at locations affected by the ice sheet (Figures 7.3a to 7.3d) is quite young while it remains old for the location not affected by the ice sheet (Figures 7.3e).

Figures 7.4 to 7.6 show the mean groundwater age distribution along the three cross sections and at the same time slices as those presented in Chapter 6. It can be seen that the initial mean age (at t = -120 kyr) is very old at depth and becomes younger near the surface, where transit times are shorter. When the ice sheet grows, at -30 kyr, large volumes of the subglacial meltwater mix with the old groundwater such that the mean groundwater age becomes younger. The mixing below the ice sheet occurs at great depths, and locations where the mean groundwater age was originally older than about 1 Myr now has a value between 10 kyr and 100 kyr. A thin veneer of young meltwater is clearly evident below the ice sheet at and following LGM. Mean groundwater ages at locations not affected by the ice sheet are not impacted as shown for the observation point located at Dawson City (Figure 7.3e). At the end of the

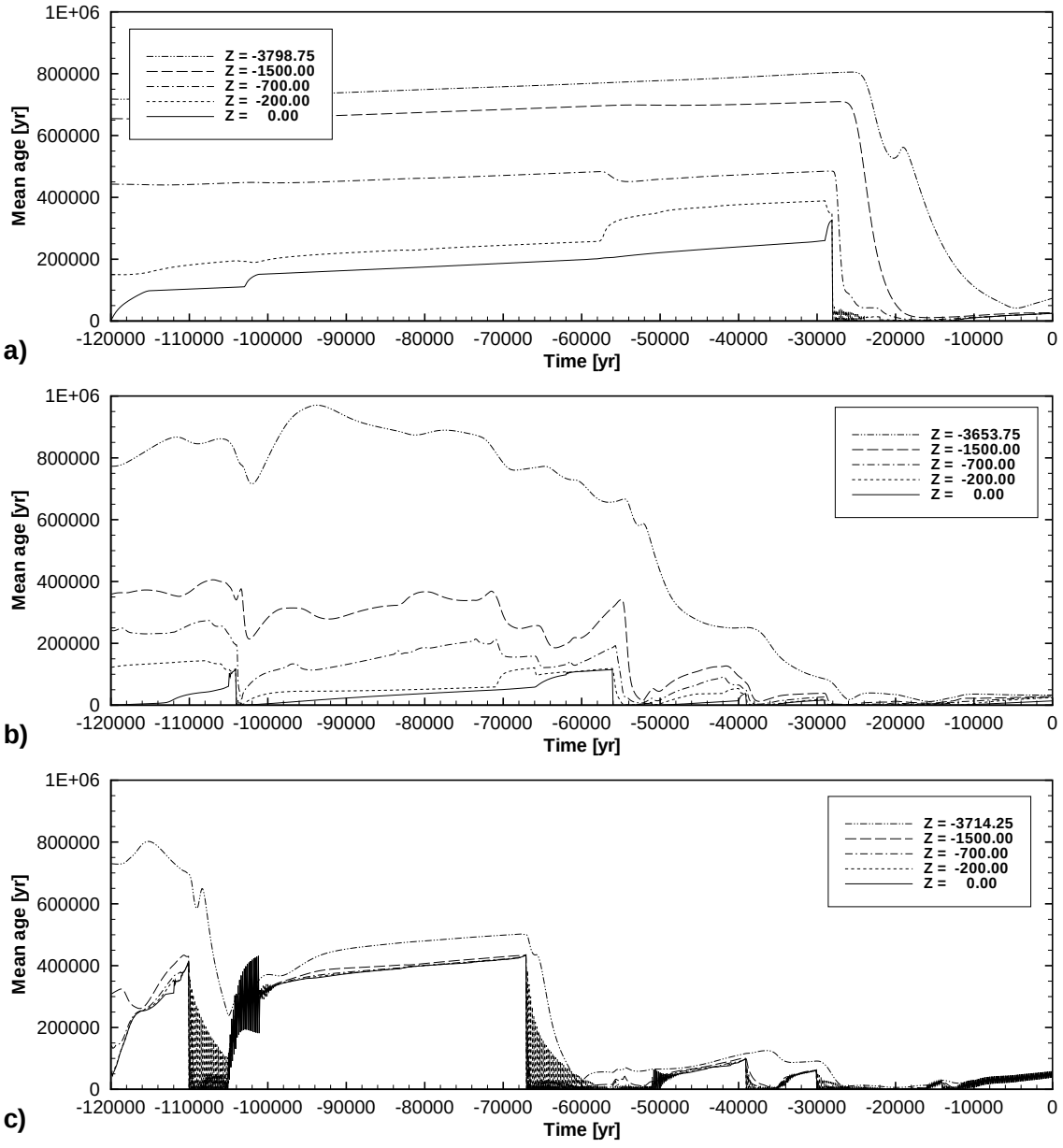

Figure 7.3: Mean age evolution at observation points for different depths. a) Edmonton (AB); b) Great Bear lake (NWT); c) Timmins (ON).

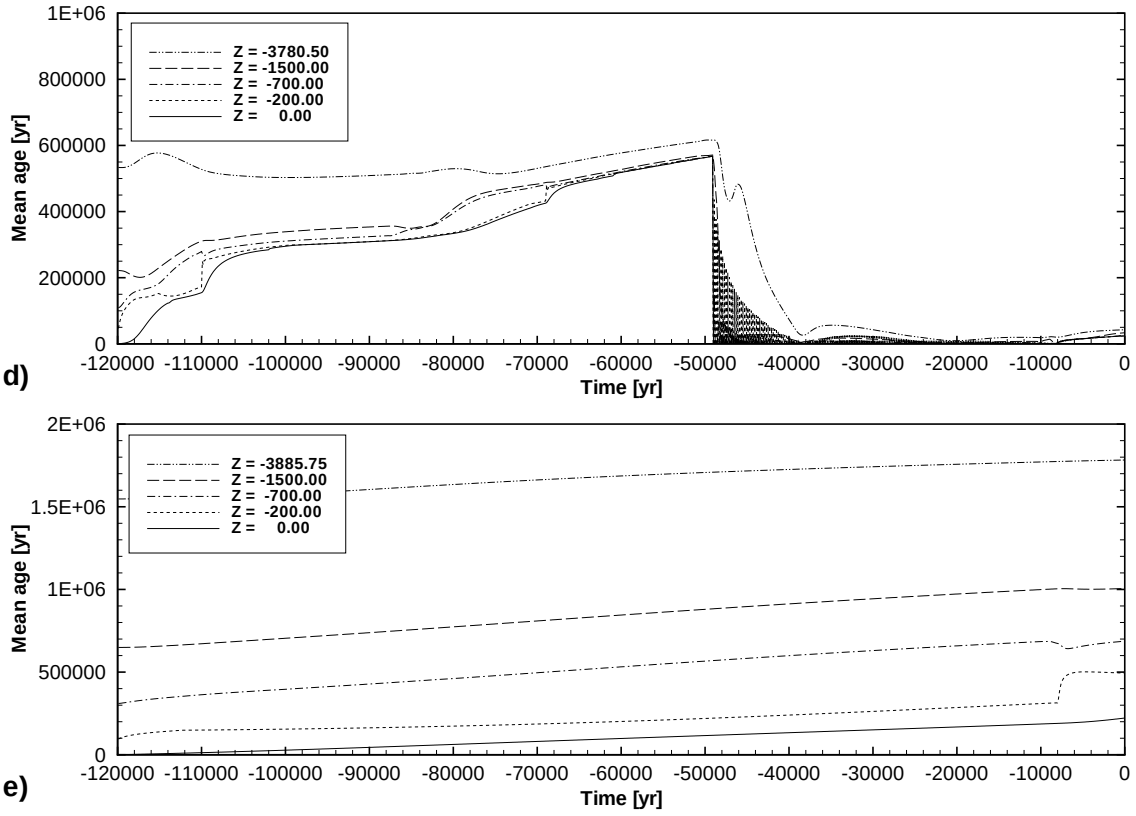

Figure 7.3: Mean age evolution at observation points for different depths (con't). d) Shefferville, (PQ); e) Dawson City (YT).

simulation period, it can be seen that mean groundwater ages below regions that were affected by the ice sheet advance and retreat are much younger than they were at LIG.

7.6 Summary

In this chapter, the concept of groundwater age was applied to compute mean groundwater ages across the Canadian landscape at LIG and throughout the last glacial cycle. It was found that at LIG, mean groundwater ages are younger near the surface and become much older with depth. The mean groundwater ages span over a large range in values, between zero and 42 Myr. Exceedingly old groundwater is found at large depths where there is little groundwater flow because of low permeabilities and because of the presence of very dense brines.

During the glacial cycle, old, deep groundwater below the ice sheet mixes with the young subglacial meltwater that infiltrates into the subsurface and the resulting mean groundwater age becomes younger. The mixing below the ice sheet occurs to great depths and locations where the mean groundwater age was originally older than 1 Myr reaches mean age values between 10 kyr and 100 kyr. Mean groundwater ages at locations not affected by the ice sheet are not impacted. At the end of the simulation period, it was found that the mean groundwater age in regions affected by the ice sheet advance and retreat is much younger than it was at LIG.

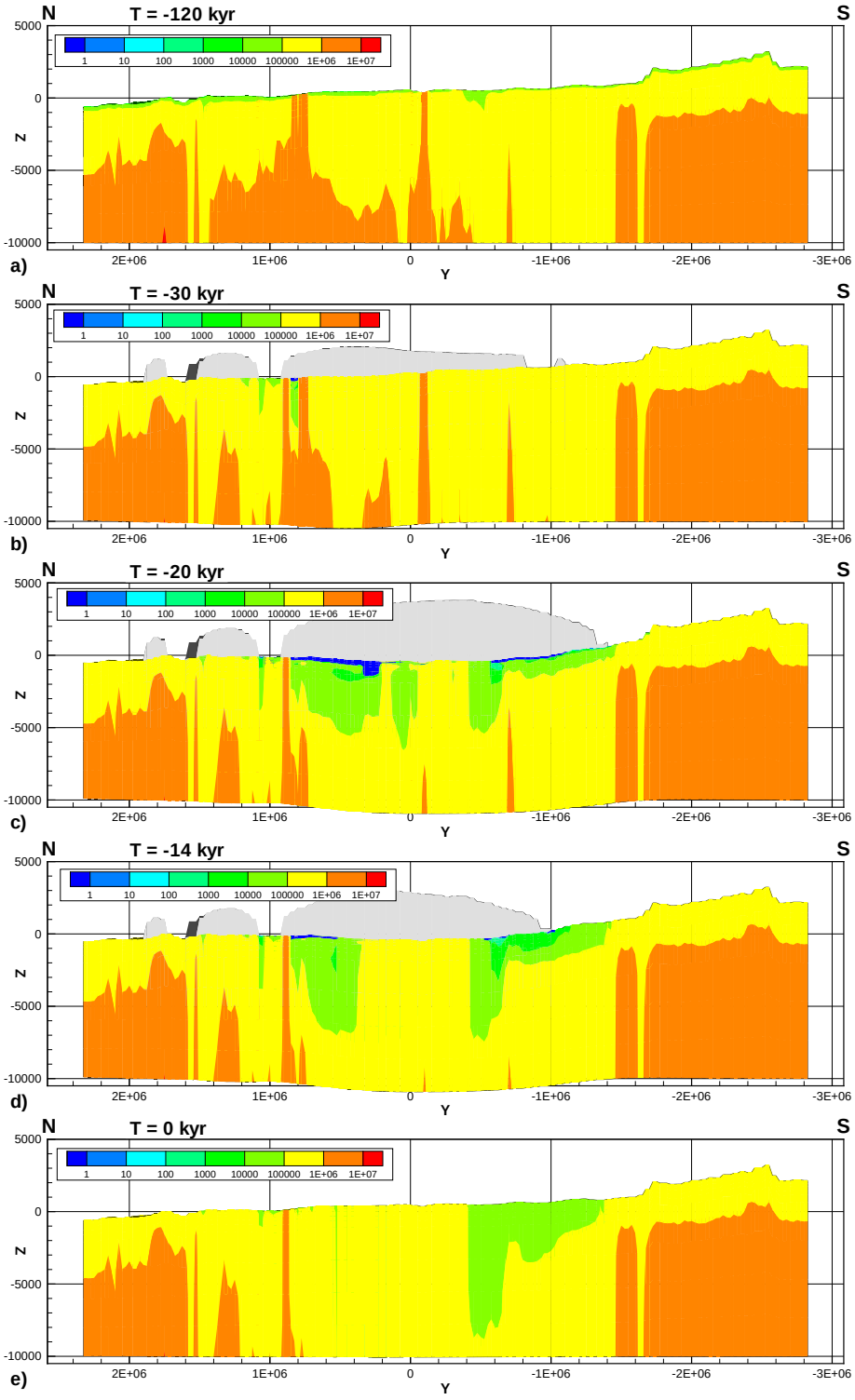

Figure 7.4: Mean groundwater age along a cross section located at $x = 0.0$ m at selected time slices: a) -120 kyr; b) -30 kyr; c) -20 kyr; d) -14 kyr and e) 0 kyr. Vertical exaggeration: 100×.

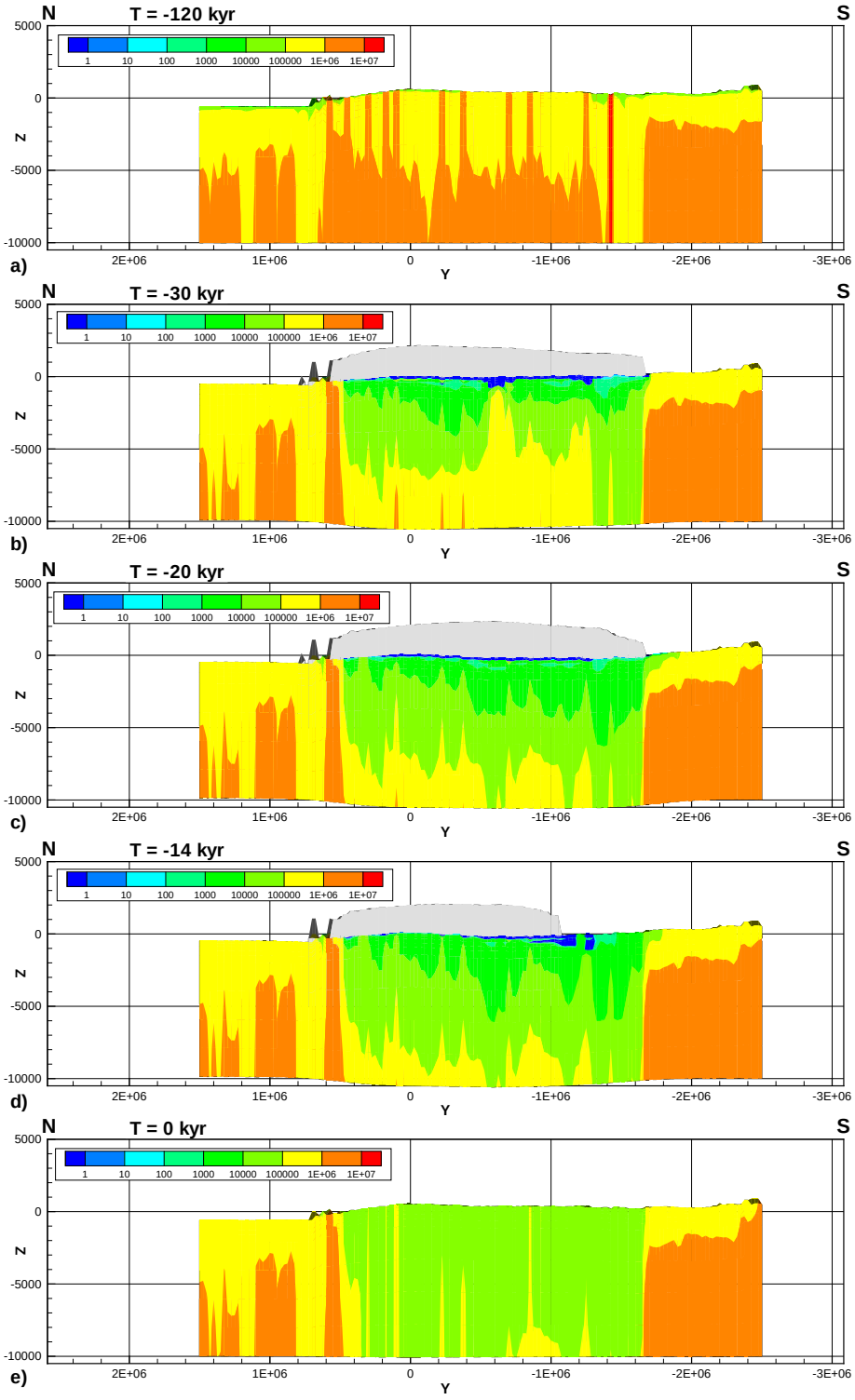

Figure 7.5: Mean groundwater age along a cross section located at $x = 2.14\times10^6$ m at selected time slices: a) -120 kyr; b) -30 kyr; c) -20 kyr; d) -14 kyr and e) 0 kyr. Vertical exaggeration: 100×.

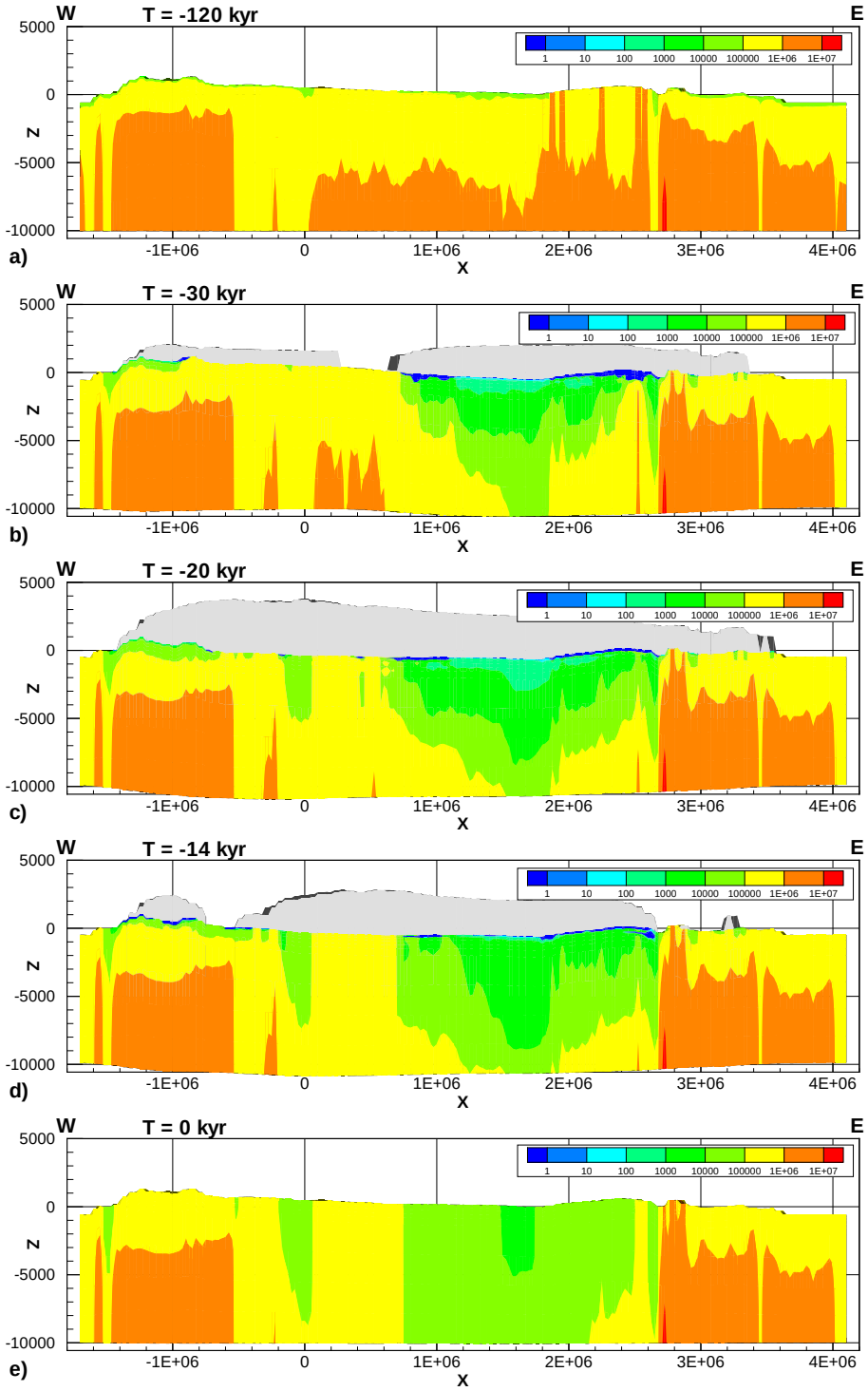

Figure 7.6: Mean groundwater age along a cross section located at y = -4.63×10^5 m at selected time slices: a) -120 kyr; b) -30 kyr; c) -20 kyr; d) -14 kyr and e) 0 kyr. Vertical exaggeration: 100×.

Chapter 8

Conclusion and Perspectives

"Science is everything we understand well enough to explain to a computer. Art is everything else."

Donald Knuth

A numerical model designated to simulate transient groundwater flow over the Canadian landscape during the Wisconsinian glaciation was developed to elucidate the impact of continental glaciation on surface/subsurface water interactions, groundwater flow dynamics, geochemical patterns and mean groundwater age distributions. During continental glaciations, the friction at the ice-bed interface as well as the upward geothermal gradient generates subglacial meltwater. Part of the meltwater will flow at the ice-bed interface as subglacial runoff, but part of it will infiltrate into the subsurface under the ambient ice-sheet pressure. Several key processes must be captured in a continental-scale 3D numerical model of groundwater flow to understand surface/subsurface interactions during a glacial period. These include subglacial infiltration, density-dependent (*i.e.*, high-salinity) groundwater flow, permafrost evolution, isostasy, sea-level changes, ice-sheet loading and surface water routing. These processes were included in the numerical model **HydroGeoSphere** which was asyn-

chronously coupled to the University of Toronto Glacial Systems Model [Tarasov and Peltier, 2005a]. Relevant data derived from the GSM at 1 kyr intervals were used to drive the groundwater model .

Subglacial flow boundary conditions used in previous studies to estimate the infiltration rate of subglacial meltwater are believed to be inadequate and often lead to unrealistic results. In this model, a specified infiltration flux equal to the computed subglacial meltwater rate is applied to the subsurface only as long as the hydraulic head at the glacier's bed is lower than ice-thickness equivalent freshwater head; otherwise the difference between the equivalent ice-sheet head at any surface node in the computational grid and the groundwater head at the same location is used to control the subsurface infiltration process; the remainder of any meltwater that is produced is treated as direct overland runoff. The reasoning behind this treatment is that if the subsurface hydraulic head becomes higher than the head equivalent to the ice sheet weight, the ice sheet would float and become unstable. This special mixed boundary condition allows the calculation of the ratio of the subglacial meltwater that infiltrates to the total meltwater that is produced.

During the last glacial cycle, the ice sheet advanced and retreated three times to form local glacial maxima. Each of these glacial advances had a different impact on the groundwater flow system because of their different intensities and durations. Their relative importance more or less coincides with the sequence of their timing, the first being the least important and the last being the most important. The last glacial advance was of the longest duration and yielded the thickest ice sheet.

In the subglacial environment, meltwater infiltration into the subsurface dominates when the ice sheet is growing. Conversely, groundwater exfiltrates during ice sheet regression. Because of the high pressures at the bed of the ice sheet, meltwater is forced downward into the subsurface during ice sheet advance and, when the ice

sheet is regressing, the pressure in the subsurface becomes higher than the basal meltwater pressure such that groundwater exfiltrates. This behaviour is a consequence of the interaction between the subglacial boundary conditions and the hydromechanical properties of the rocks. This behaviour was also highlighted using a simple numerical experiment involving a 1D column. A sensitivity analysis of the subglacial infiltration to the loading efficiency parameter was performed and showed that the infiltration rate into the subsurface diminishes with an increase of the loading efficiency parameter.

During the glacial period, the average subglacial infiltration rate into the subsurface was determined to vary between 0 and 6 mm/yr with an average of 2.5 mm/yr, which is at least three orders of magnitudes higher than that occurring in the periglacial environment and two orders of magnitude higher than during the interglacial period. The periglacial environment has an infiltration rate lower than the interglacial infiltration value, which is about 0.03 mm/yr. The average ratio of the subglacial infiltration rate to the ratio of subglacial meltwater production varies between 15% to 100%, with an average of 43%. This indicates that a large fraction of the meltwater actually entered the subsurface.

In the periglacial environment, it was shown that the infiltration and exfiltration flux oscillates between 0 and 0.06 mm/yr, with averages of 0.003 and 0.007 mm/yr, respectively. This is much lower than that occuring in the subglacial environment. Most of the periglacial exchange flux is dominated by exfiltration during ice sheet regression.

There is an important difference between the meltwater infiltration rate in sedimentary basins compared to that in the Canadian Shield. The subglacial infiltration rate is larger for the sedimentary rocks because of their higher hydraulic conductivity values. This has implications in the subglacial environment because the hydraulic

heads at the surface of the sedimentary rocks are often lower than the ice-sheet-equivalent freshwater head while, for the case of the Shield rocks, the constraint that the basal heads below the ice sheet cannot exceed the equivalent head of the ice-sheet thickness is frequently reached. This suggests that lateral runoff beneath the ice is more abundant over the Shield rocks than over the sedimentary rocks because a large portion of the meltwater cannot infiltrate into the Shield rocks due to their low permeability.

The impact of the ice sheet on groundwater flow patterns is dramatic. Hydraulic heads below the ice sheet increase by as much as several kilometers to depths of about 1.5 km into the subsurface. At present time, it is predicted that large over-pressurized zones should exist at depth because of the large time needed to allow dissipation to their original values. Much of the increase in the hydraulic head is related to the infiltration of subglacial meltwater into the rocks; another smaller component is due to the hydromechanical loading induced by the ice sheet. During the advance and retreat of the ice, vertical hydraulic gradients can reverse. The magnitude of the Darcy flux varied in time by about two orders of magnitude at depths of -700 m to -1500 m. The distribution of the TDS concentrations became highly modified and large lenses of diminished concentration zones appeared where infiltrating pulses of subglacial meltwater caused dilution of the TDS to depths of several kilometers in some areas.

Permafrost has the effect of restraining large areas of the subglacial environment from surface/subsurface water interaction. For example, the presence of permafrost can lead to the occurrence of trapped pressure zones below the permafrost. On the other hand, the presence of taliks, as currently observed at high latitudes but not incorporated in the model due to its large scale, could aid in dissipation of the high pressure zones noted in the model results.

Based on the simulated hydraulic head and solute concentration distributions after the last glacial cycle, it was shown that the system did not recover to its initial LIG state because of the last glacial perturbation. This suggests that the current groundwater flow system cannot be solely interpreted using present-day boundary conditions. Several thousand additional years of recovery may be necessary for the system to reach a new equilibrium. This also points out that the steady-state assumption sometimes used in order to simulate the impact of glaciation on regional-scale groundwater flow patterns is inappropriate.

As a final contribution, the mean groundwater age across the Canadian landscape at LIG and throughout the last glacial cycle was computed. Groundwater age is defined as the time elapsed since the water infiltrated in a recharge zone. It was found that at LIG, mean groundwater ages span over a large range in values, from zero to 42 My. The exceptionally old groundwater occurs at great depth where there is little permeability and where very high salinity exists. The distribution of the mean groundwater age over the landscape at LIG indicates that most of the shallow water has a relatively young age, except for a few locations along the coast of Québec, portions of Baffin Island and the north shore of Nunavut which have very old near-surface waters. During the glacial period, old groundwater below the ice sheet mixes with young subglacial meltwater that infiltrates into the ground and the resulting mean groundwater age becomes younger. The mixing below the ice sheet occurs to great depth in some locations causing mean groundwater ages that originally exceeded 1 Myr to reach age values between 10 kyr and 100 kyr. At the end of the simulation period, it was found that mean groundwater ages at locations affected by the ice sheet advance and retreat became much younger than they were at LIG.

8.1 Limitations

Although several key factors related to the impact of glaciation on continental groundwater flow were highlighted, the scale and complexity of the model brings to bear some limitations that should be recognized. First, the geological model used to assign the subsurface hydraulic properties is quite simple and does not include local and regional heterogeneities. For example, the sedimentary basins, which include both high- and low-permeability stratas could not be discretized due in part to the relatively small size of the individual formations compared to the size of the entire model, but also because of the paucity of high-resolution 3D stratigraphic data covering the entire continent. Basic regional flow trends are, however, felt to be captured by the model. Other aspects not included in the flow model include major faults and hydraulic anisotropy.

Permafrost formation creates several consequences that are not represented in the numerical model because of their complexity. Salt rejection upon the freezing of water is one of the processes thought to be important. Starinsky and Katz [2003], for example, even hypothesized that this phenomenon is responsible for the formation of the Shield brines, although their hypothesis remains contentious. The migration of dissolved salts downward with the advance of the permafrost front would increase the water density at depth. During the thawing of the permafrost zone, low TDS water would exist at shallow depths at least until upward migration of the TDS occurs via diffusion and any upward advection that develops.

The relative permeability of permafrost to ice content is another area that could benefit from additional laboratory and field measurements. Porewater expulsion due to volume expansion during the freezing is yet another process that is not well documented in the literature. The inclusion of these phenomena into a numerical model

is a formidable task especially if it is desired to account for the consequences in the context of a regional- or continental-scale model.

Another uncertain aspect in the model concerns the initial condition in the subsurface. Because there are no exhaustive paleo-hydrogeological data available at the continental scale, the model was run until a steady state was achieved using the LIG boundary conditions in order to obtain the initial conditions for the transient glacial-cycle simulations. This methodology yields reasonable results for the TDS profiles across the Shield and the Michigan basin, but other benchmark measurements such as ^{14}C ages would greatly improve confidence in the model.

There is also a serious lack of national databases and digital datasets pertaining to groundwater flow parameters and water quality indicators that can be used to refine the current model. There are several descriptive national overviews, but no serious surveys of groundwater conditions across Canada exist. There is also a serious lack of data in the sparsely-populated regions of Canada, which also comprise the largest regions. Extensive reviews of the groundwater regions of Canada is an urgent need.

The several additions included in the numerical model **HydroGeoSphere**, as well as the methodology described in this thesis, could be easily transposed into detailed studies of the impact of glaciation on specific regional-scale hydrogeologic basins. Nevertheless, at the scale of the current study, major trends and processes pertaining to groundwater flow system evolution during a glaciation across the Canadian landscape were delineated and these improve our current knowledge.

Finally, the originality of this work mainly lies with the advancements made in two areas. Firstly, it is, to the author's knowledge, the first study of the impact of glaciation on groundwater flow that is both transient and three dimensional, and incorporates subglacial infiltration, density-dependent groundwater flow, permafrost evolution, land surface elevation changes due to isostasy, ice sheet hydromechanical

loading and unloading, sea-level change and groundwater age calculations in a single unified numerical model. Secondly, it is also the first study, to the author's knowledge, that addresses groundwater flow at a continental-scale encompassing the Canadian landscape. The novel character of these two aspects of the thesis make it a major contribution to the fields of hydrogeology and paleohydrogeology. It is also perhaps a starting point to assess the potential impacts of anthropogenically-induced future climate change on Canada's groundwater resources.

Bibliography

Ates, Y., Bruneau, D., and Ridgway, W. R. (1997). Continental glaciation and its possible impact on a used-fuel disposal vault in the Canadian Shield. Technical Report AECL-10140, COG-94-37-I, Atomic Energy of Canada Limited, Whiteshell Laboratories, Pinawa, Manitoba, Canada.

Bassin, C., Laske, G., and Masters, G. (2000). The current limits of resolution for surface wave tomography in North America. *EOS Trans. AGU*, **81**(48), 897. Fall Meet. Suppl.

Bear, J. (1972). *Dynamics of fluids in porous media*. American elsevier, New York, NY.

Berger, A. and Loutre, M.-F. (2004). À quand la prochaine glaciation? [For when the next glaciation?]. *Les Dossiers de la Recherche*, **17**, 18–22.

Boulton, G. S. and de Marsily, G. (1997). Hydrogeological aspects of glaciation. In L. King-Clayton, N. Chapman, L. O. Ericsson, and F. Kautsky, editors, *Glaciation and Hydrogeology*, SKI Report 97:13, pages 33–44. Stockholm, Sweden.

Boulton, G. S. and Payne, A. (1993). Simulation of the European ice sheet through the last glacial cycle and prediction of future glaciations. Technical Report TR-93-14, SKB, Stockholm, Sweden.

Boulton, G. S., Slot, T., Blessing, K., Glasbergen, P., leijnse, T., and van Gijssel, K. (1993). Deep circulation of groundwater in overpressured subglacial aquifers and it's geological consequences. *Quaternary Science Reviews*, **12**, 739–745.

Boulton, G. S., Caban, P. B., and van Gijssel, K. (1995). Groundwater flow beneath ice sheets: Part I - Large scale patterns. *Quaternary Science Reviews*, **14**, 545–562.

Boulton, G. S., Caban, P. B., van Gissel, K., Leijnse, A., Punkari, M., and van Weert, F. H. A. (1996). The impact of glaciation on the groundwater regime of Northwest Europe. *Global and Planetary Change*, **12**(1–4), 397–413.

Boulton, G. S., Zaptsepin, S., and Maillot, B. (2001). Analysis of groundwater flow beneath ice sheets. Technical Report TR-01-06, SKB, Stockholm, Sweden.

Breemer, C. H., Clark, P. U., and Haggerty, R. (2002). Modeling the subglacial hydrology of the late Pleistocene Lake Michigan Lobe, Laurentide Ice Sheet. *GSA Bulletin*, **114**(6), 665–674.

Burt, T. P. and Williams, P. J. (1976). Hydraulic conductivity in frozen soils. *Earth Surface Processes*, **1**(4), 349–360.

Carslaw, H. S. and Jaeger, J. C. (1959). *Conduction of Heat in Solids*. Oxford University Press, New York, second edition.

Chan, T. and Stanchell, F. W. (2005). Subsurface hydro-mechanical (HM) impacts of glaciation: Sensitivity to transient analysis, HM coupling, fracture zone connectivity and model dimensionality. *International Journal of Rock Mechanics and Mining Sciences*, **42**(5-6), 828–849.

Chan, T., Christiansson, R., Boulton, G. S., Ericsson, L. O., Hartikainen, J., Jensen, M. R., Ivars, D. M., Stanchell, F. W., Vistrand, P., and Wallroth, T. (2005). DE-

COVALEX III BMT3/BENCHPAR WP4, the thermo-hydro-mechanical responses to a glacial cycle and their potential implications for deep geological disposal of nuclear fuel waste in a fractured crystalline rock mass. *International Journal of Rock Mechanics and Mining Sciences*, **42**(5-6), 805–827.

Clark, I. D., Douglas, M., Raven, K., and Bottomley, D. (2000). Recharge and preservation of Laurentide glacial melt water in the Canadian Shield. *Ground Water*, **38**(5), 735–742.

Clark, P. U. and Walder, J. S. (1994). Subglacial drainage, eskers, and deforming beds beneath the Laurentide and Eurasian ice sheets. *GSA Bulletin*, **106**(2), 304–314.

Clarke, G. K. C. (2005). Subglacial processes. *Annual Review of Earth and Planetary Sciences*, **33**, 247–276.

Cornaton, F. (2004). *Deterministic models of groundwater age, life expectancy and transit time distributions in advective-dispersive systems.* Ph.D. thesis, University of Neuchâtel, Switzerland.

Cornaton, F. and Perrochet, P. (2006). Groundwater age, life expectancy and transit time distributions in advectivedispersive systems: 1. Generalized reservoir theory. *Advances in Water resources*, **29**(9), 1267–1291.

Crutzen, P. J. and Stoermer, E. F. (2000). The "Anthropocene". *IGBP Newsletter*, (41), 17–18.

Cutler, P. M., MacAyeal, D. R., Mickelson, D., Parizek, B. R., and Colgan, P. M. (2000). A numerical investigation of ice-lobe–permafrost interaction around the southern Laurentide ice sheet. *Journal of glaciology*, **46**(153), 311–325.

de Hoog, F. R., Knight, J. R., and Stokes, A. N. (1982). An improved method for numerical inversion of Laplace transforms. *Society for Industrial and Applied Mathematics*, **3**(3), 357–366.

Dollar, P., Frape, S. K., and McNutt, R. H. (1991). Geochemistry of formation waters, southwestern Ontario, Canada and southern Michigan, U.S.A.: Implications for origin and evolution. Open file report 5743, Ontario Geological Survey. 72 p.

Douglas, M., Clark, I. D., Raven, K., and Bottomley, D. (2000). Groundwater mixing dynamics at a Canadian Shield mine. *Journal of Hydrology*, **235**(1-2), 88–103.

Douglas, R. J. W. (1971). Introduction. In R. J. W. Douglas, editor, *Geology and economic minerals of Canada*. Dep. Energy, Mines and Resources, Ottawa, Canada.

Duplessy, J.-C. and Morel, P. (1990). *Gros temps sur la planète [Heavy weather on Earth]*. Editions Odile Jacob, France.

Farvolden, R. N., Pfannkuch, O., Pearson, R., and Fritz, P. (1988). Region 12, Precambrian Shield. In W. Back, J. S. Rosenhein, and P. R. Seaber, editors, *Hydrogeology*, pages 101–114. The Geology of North America, O-2, Boulder, Colorado.

Fisher, A. T. (1998). Permeability within basaltic oceanic crust. *Reviews of Geophysics*, **32**(2), 142–182.

Forsberg, C. F. (1996). Possible consequences of glacially induced groundwater flow. *Global and Planetary change*, **12**(1–4), 387–396.

Foxworthy, B. L., Hanneman, D. L., Coffin, D. L., and Halstead, E. C. (1988). Region 1, Western mountain Ranges. In W. Back, J. S. Rosenhein, and P. R. Seaber, editors, *Hydrogeology*, pages 25–35. The Geology of North America, O-2, Boulder, Colorado.

Frape, S. K. and Fritz, P. (1987). Geochemical trends for groundwaters from the Canadian Shield. In P. Fritz and S. K. Frape, editors, *Saline water and gases in crystalline rocks*, pages 19–38. Geological Association of Canada Special paper 33.

Freeze, A. and Cherry, J. A. (1979). *Groundwater*. Prentice Hall.

Freeze, R. A. and Witherspoon, P. A. (1967). Theoretical analysis of regional groundwater flow, II - Effect of water-table configuration and subsurface permeability variations. *Water Resources Research*, **3**(2), 623–634.

Frind, E. O. (1982). Simulation of long-term transient density-dependant transport in groundwater. *Advances in water Resources*, **5**(2), 73–88.

Frost, L. H. (1997). Underground Research Laboratory shaft excavation drawdown experiment: Estimate of hydraulic parameter values for moderately fractured rock. Technical Report TR-751, COG-96-282-I, Atomic Energy of Canada Limited, Whiteshell Laboratories, Pinawa, Manitoba, Canada.

Frost, L. H. and Everitt, R. A. (1997). Excavation damage zone tracer experiment in the floor of the room 415 test tunnel. Technical Report AECL-11640, COG-96-321-I, Atomic Energy of Canada Limited, Whiteshell Laboratories, Pinawa, Manitoba, Canada.

Garven, G. (1989). A hydrogeologic model for the formation of the giant oil sands deposits of the Westerns Canada sedimentary basin. *American Journal of Science*, **289**, 105–166.

Garven, G. (1995). Continental-scale groundwater flow and geologic processes. *Annu. Rev. Earth Planet. Sci.*, **23**, 89–117.

Garven, G. and Freeze, R. A. (1984a). Theoretical analysis of the role of groundwater flow in the genesis of stratabound ore deposits: I. mathematical model. *American Journal of Science*, **284**, 1085–1124.

Garven, G. and Freeze, R. A. (1984b). Theoretical analysis of the role of groundwater flow in the genesis of stratabound ore deposits: II. quantitative results. *American Journal of Science*, **284**, 1085–1124.

Gascoyne, M. (2000). A review of published literature on the effects of permafrost on the hydrogeochemistry of bedrock. Posiva 2000-9, Posiva Oy, Helsinki, Finland.

Gascoyne, M. and Sheppard, M. I. (1993). Evidence of terrestrial discharge of deep groundwater on the Canadian Shield from Helium in soil gases. *Environmental Science & Technology*, **27**(12), 2420–2426.

Gibbard, P. L., Smith, A. G., Zalasiewicz, J. A., Barry, T. L., Cantrill, D., Coe, A. L., Cope, J. C. W., Gale, A. S., Gregory, F. J., Powell, J. H., Rawson, P. F., Stone, P., and Waters, C. N. (2005). What status for the Quaternary? *Boreas*, **34**(1), 1–6.

Globensky, Y. (1987). Géologie des Basses-Terres du Saint-Laurent. Technical Report MM 85-02, Ministre de l'Énergie et des Ressources, Québec, Quebec, Canada.

Graf, T. (2005). *Modeling Coupled Thermohaline Flow and Reactive Solute Transport in Discretely-Fractured Porous Media*. Ph.D. thesis, Université Laval, Québec, Canada.

Grasby, S., Osadetz, K., Betcher, R., and Render, F. (2000). Reversal of the regional-scale flow system of the Williston basin in response to Pleistocene glaciation. *Geology*, **28**(7), 635–638.

Grasby, S. E. and Chen, Z. (2005). Subglacial recharge into the western Canada sedimentary basin - impact of Pleistocene glaciation on basin hydrodynamics. *GSA Bulletin*, **117**(3/4), 500–514.

Hays, J. D., Imbrie, J., and Shackleton, N. J. (1976). Variations in the Earth's orbit: pacemaker of the ice ages. *Science*, **194**, 1121–1132.

Heath, R. C. (1988). Hydrogeological setting of regions. In W. Back, J. S. Rosenhein, and P. R. Seaber, editors, *Hydrogeology*, pages 15–35. The Geology of North America, O-2, Boulder, Colorado.

Heathcote, J. A. and Michie, U. M. (2004). Estimating hydrogeological conditions over the last 120 ka: an example from the Sellafield area, UK. *Journal of the Geological Society*, **161**, 995–1008.

Hooke, R. L. and Jennings, C. E. (2006). On the formation of the tunnel valleys of the southern Laurentide ice sheet. *Quaternary Science Reviews*, **25**(11-12), 1364–1372.

Huenges, E., Erzinger, J., Kück, J., Engeser, B., and Kessels, W. (1997). The permeable crust: Geohydraulic properties down to 9101 m depth. *Journal of Geophysical Research*, **102**(B8), 18 255–18 265.

Hughes, T. J. (1998). *Ice Sheets*. Oxford University Press, Oxford. 343 pp.

Ingebritsen, S. E. and Manning, C. E. (1999). Geological implications of a permeability-depth curve for the continental crust. *Geology*, **27**(12), 1107–1110.

Ingebritsen, S. E. and Sanford, W. E. (1998). *Groundwater in geologic processes*. Cambridge University Press.

International Permafrost Association Standing Committee on Data Information and Communication, comp. (2003). Circumpolar active-layer permafrost system, ver-

sion 2.0. edited by M. Parsons and T. Zhang. Boulder, CO: National Snow and Ice Data Center/World Data Center for Glaciology. CD-ROM.

Jaquet, O. and Siegel, P. (2003). Groundwater flow and transport modelling during a glaciation period. Technical Report TR-03-04, SKB, Stockholm, Sweden.

Jaquet, O. and Siegel, P. (2006). Regional groundwater flow model for a glaciation scenario. Simpevarp subarea – version 1.2. Technical Report TR-06-100, SKB, Stockholm, Sweden.

Kamb, B. (1987). Glacier surge mechanism based on linked cavity configuration of the basal water conduit system. *Journal of Geophysical Research*, **92**(B9), 9083–9100.

King-Clayton, L. M., Chapman, N. A., Kautsky, F., Svensson, N.-O., de Marsily, G., and Ledoux, E. (1995). The central scenario for SITE-94: A climate change scenario. SKI Report 95:42, Swedish Nuclear Power Inspectorate, Stockholm, Sweden.

Kleinberg, R. L. and Griffin, D. D. (2005). NMR measurements of permafrost: unfrozen water assay, pore-scale distribution of ice, and hydraulic permeability of sediments. *Cold Regions Science and Technology*, **42**(1), 63–77.

Kuchling, K., Chorley, D., and Zawadski, W. (2000). Hydrogeological modeling of mining operations at the Diavik Diamonds project. In *Proceedings of the 6th International Symposium on Environmental Issues and Waste Management in Energy and Mineral Production*, May 30-June 2, Calgary, Alberta, Canada.

Lliboutry, L. (1968). General theory of subglacial cavitation and sliding of temperate glaciers. *Journal of Glaciology*, **7**(49), 21–58.

Manning, C. E. and Ingebritsen, S. E. (1999). Permeability of the continental crust:

implications of geothermal data and metamorphic systems. *Reviews of Geophysics*, **37**(1), 127–150.

McEwen, T. and de Marsily, G. (1991). The potential significance of premafrost to the behaviour of a deep radioactive waste repository. SKI Report 91:8, Swedish Nuclear Power Inspectorate, Stockholm, Sweden.

McIntosh, J. C. and Walter, L. M. (2005). Volumetrically significant recharge of Pleistocene glacial meltwaters into epicratonic basins: Constraints imposed by solute mass balances. *Chemical Geology*, **222**(3-4), 292–309.

McIntosh, J. C., Walter, L. M., and Martini, A. M. (2002). Pleistocene recharge to midcontinent basins: Effects on salinity structure and microbial gas generation. *Geochimica et Cosmochimica Acta*, **66**(10), 1681–1700.

McIntosh, J. C., Garven, G., and Hanor, J. S. (2005). Modeling variable-density fluid flow and solute transport in glaciated sedimentary basins. *Eos Trans. AGU*, **86**(52). Fall Meet. Suppl., Abstract H11D-1310.

Mooney, W. D., Laske, G., and Masters, G. (1998). Crust 5.1: A global crustal model at $5^\circ \times 5^\circ$. *J. Geophys. Res.*, **103**(B1), 727–747.

Nastev, M., Savard, M. M., Lapcevic, P., Lefebvre, R., and Martel, R. (2004). Hydraulic properties and scale effects investigation in regional rock aquifers, southwestern Quebec, Canada. *Hydrogeology Journal*, **12**(3), 257–269.

Neuzil, C. E. (1995). Abnormal pressures as hydrodynamic phenomena. *American Journal of Science*, **295**, 742–786.

Neuzil, C. E. (2003). Hydromechanical coupling in geological processes. *Hydrogeology Journal*, **11**(1), 41–83.

Nye, J. F. (1973). Water at the bed of an ice sheet. *IAHS Publication*, **95**, 189–194.

Paterson, W. S. B. (1994). *The physics of glaciers*. Pergamon Press, Oxford, 3rd edition. 480 pp.

Peltier, W. R. (2002). A design basis glacier scenario. Technical Report 06819-REP-01200-10069-R00, Ontario Power Generation, Toronto, Canada.

Person, M., Dugan, B., Swenson, J. B., Urbano, L., Stott, C., Taylor, J., and Willett, M. (2003). Pleistocene hydrogeology of the Atlantic continental shelf, New England. *GSA Bulletin*, **115**(11), 1324–1343.

Peteet, D. (2006). Enigmatic Laurentide Ice Sheet deglaciation. *EOS*, **87**(15), 151.

Philip, J. R. (1991). Soils, natural science, and models. *Soil Science*, **151**(1), 91–98.

Piotrowski, J. A. (1997a). Subglacial groundwater flow during the last glaciation in northwestern Germany. *Sedimentary Geology*, **111**, 217–224.

Piotrowski, J. A. (1997b). Subglacial hydrology in north-western Germany during the last glaciation: groundwater flow, tunnel, valleys and hydrological cycles. *Quaternary Science Reviews*, **16**, 169–185.

Piotrowski, J. A. and Kraus, A. (1997). Response of sediment to ice sheet loading in northwestern Germany: effective stresses and glacier bed stability. *Journal of Glaciology*, **43**(145), 495–502.

Provost, A. M., Voss, C. I., and Neuzil, C. E. (1998). Glaciation and regional groundwater flow in the Fennoscandian shield; Site 94. SKI Report 96:11, Swedish Nuclear Power Inspectorate, Stockholm, Sweden.

Randall, A. D., Francis, R. M., Frimpter, M. H., and Emery, J. M. (1988). Region 19, Northeastern Appalachians. In W. Back, J. S. Rosenhein, and P. R. Seaber, editors, *Hydrogeology*, pages 177–187. The Geology of North America, 0-2, Boulder, Colorado.

Raven, K. G. (1986). Hydraulic characterization of a small groundwater flow system in fractured monzonitic gneiss. Technical report, National Hydrology Research Institute Paper No. 30, Inland Waters Directorate Series No. 149, Environment Canada, Ottawa, Canada.

Raven, K. G. and Gale, J. E. (1986). A study of the surface and subsurface conditions at selected underground mines and excavations. Technical Report TR-177, Atomic Energy of Canada Limited, Pinawa, Manitoba, Canada.

Raven, K. G., Bottomley, D. J., Sweezey, R. A., Smedley, J. A., and Ruttan, T. J. (1987). Hydrogeological characterization of the East Bull Lake research area. Technical report, National Hydrology Research Institute Paper No. 31, Inland Waters Directorate Series No. 160, Environment Canada, Ottawa, Canada.

Rice, J. R. and Cleary, M. P. (1976). Some basic stress diffusion solutions for fluid-saturated elastic porous media with compressible constituents. *Reviews of Geophysics*, **14**(2), 227–241.

Ross, M., Parent, M., and Lefebvre, R. (2005). 3D geologic framework models for regional hydrogeology and land-use management: a case study from a Quaternary basin of southwestern Quebec, Canada. *Hydrogeology Journal*, **13**(5-6), 690–707.

Röthlisberger, H. (1972). Water pressure in intra- and subglacial channels. *Journal of Glaciology*, **11**, 177–203.

Rouleau, A., Guha, J., Archambault, G., and Benlahcen, A. (2003). An overview of the hydrogeology of the Precambrian basement in Quebec and related mining problems. In J. Krásny, Z. Hrkal, and J. Bruthans, editors, *Proceedings of the International Conference on Groundwater in Fractured Rocks, Prague, Czech Republic, 15-19 September 2003: extended abstracts*, number 7 in IHP-VI series on groundwater, pages 379–380. Unesco document.

Sheppard, M. I., Thibault, D. H., Milton, G. M., Reid, J. A. K., Smith, P. A., and Steve, K. (1995a). Characterization of a suspected terrestrial deep groundwater discharge area on the Canadian Precambrian shield. *Journal of Contaminant Hydrology*, **18**(1), 59–84.

Sheppard, M. I., Amiro, B. D., Davis, P. A., and Zach, D. R. (1995b). Continental glaciation and nuclear fuel waste disposal: Canada's approach and assessment of the impact on nuclide transport through the biosphere. *Ecological modelling*, **78**(3), 249–265.

Shoemaker, E. M. (1986). Subglacial hydrology for an ice sheet resting on a deformable aquifer. *Journal of Glaciology*, **32**(110), 20–30.

Siegel, D. I. (1989). Geochemistry of the Cambrian-Ordovician aquifer system in the Northern Midwest, United States. U. S. Geological Survey Professional Paper 1405-D, USGS, Denver, Colorado.

Siegel, D. I. (1991). Evidence for dilution of deep, confined ground water by vertical recharge of isotopically heavy Pleistocene water. *Geology*, **19**(5), 433–436.

Siegel, D. I. and Mandle, R. J. (1983). Isotopic evidence for glacial meltwater recharge to the Cambrian-Ordovician aquifer, North-Central United States. *Quaternary Research*, **22**(3), 328–335.

Smith, S. L. and Burgess, M. M. (2002). A digital database of permafrost thickness in Canada. Open file 4173, Geological Survey of Canada, Ottawa, Canada.

Snyder, J. P. (1987). Map projections–A working manual. U. S. Geological Survey Professional Paper 1395, USGS, Denver, Colorado.

Spencer, R. J. (1987). Origin of Ca–Cl brines in Devonian formations, western Canada sedimentary basin. *Applied Geochemistry*, **2**(2), 373–384.

Starinsky, A. and Katz, A. (2003). The formation of natural cryogenic brines. *Geochemica et Cosmochimica Acta*, **67**(8), 1475–1484.

Stevenson, D. R., Brown, A., Davison, C. C., Gascoyne, M., McGregor, R. G., Ophori, D. U., Scheier, N. W., Stanchell, F., Thorne, G. A., and Tomsons, D. K. (1996). A revised conceptual hydrogeologic model of a crystalline rock environment, Whiteshell research area, southeastern Manitoba, Canada. Technical Report AECL 11331, COG-95-271, Atomic Energy of Canada Limited, Whiteshell Laboratories, Pinawa, Manitoba.

Stober, I. and Bucher, K. (2004). Fluid sinks within the earth's crust. *Geofluids*, **4**(2), 143–151.

Stober, I. and Bucher, K. (2005). The upper continental crust, an aquifer and its fluid: hydaulic and chemical data from 4 km depth in fractured crystalline basement rocks at the KTB test site. *Geofluids*, **5**(1), 8–19.

Stockwell, C. H., Mcglynn, J. C., Emslie, R. F., Sanford, B. V., Norris, A. W., Donaldson, J. A., Fahrig, W. F., and Currie, K. L. (1971). Geology of the Canadian Shield. In R. J. W. Douglas, editor, *Geology and economic minerals of Canada*, pages 44–150. Dep. Energy, Mines and Resources, Ottawa, Canada.

Svensson, U. (1999). Subglacial groundwater flow at Äspö as governed by basal melting and ice tunnels. Technical Report TR-99-38, SKB, Stockholm, Sweden.

Talbot, C. J. (1999). Ice ages and nuclear waste isolation. *Engineering Geology*, **52**(3–4), 177–192.

Tarasov, L. and Peltier, W. R. (1999). Impact of thermomechanical ice sheet coupling on a model of the 100 kyr ice age cycle. *Journal Of Geophysical Research-Atmospheres*, **104**(D8), 9517–9545.

Tarasov, L. and Peltier, W. R. (2004). A geophysically constrained large ensemble analysis of the deglacial history of the North American ice-sheet complex. *Quaternary Science Reviews*, **23**(3-4), 359–388.

Tarasov, L. and Peltier, W. R. (2005a). Arctic freshwater forcing of the Younger Dryas cold reversal. *Nature*, **435**(7042), 662–665.

Tarasov, L. and Peltier, W. R. (2005b). The co-evolution of continental ice cover and permafrost extent over the last glacial-interglacial cycle in North America. *Eos Trans. AGU*, **86**(52). Fall Meet. Suppl., Abstract C22A-08.

Teller, J. T. (1987). Proglacial lakes and the southern margin of the Laurentide Ice Sheet. In W. F. Ruddiman and H. E. Wright, editors, *North America and adjacent oceans during the last deglaciation*, pages 39–67. The Geology of North America, K-3, GSA, Boulder, Colorado.

Theis, C. V. (1935). The relation between the lowering of the piezometric surface and the rate and duration of discharge of a well using groundwater storage. *Transactions of the American Geophysical Union*, **16**, 519–524.

Therrien, R. and Sudicky, E. A. (1996). Three-dimensional analysis of variably-saturated flow and solute transport in discretely-fractured porous media. *Journal of Contaminant Hydrology*, **23**(1-2), 1–44.

Therrien, R., McLaren, R., Sudicky, E. A., and Panday, S. (2006). *HydroGeoSphere, A Three-dimensional Numerical Model Describing Fully-integrated Subsurface and Surface Flow and Solute Transport*. Groundwater Simulations Group.

Thorne, G. (2004). Hydrological processes in Precambrian Shield catchments of south-eastern Manitoba. *Eos Trans. AGU*, **85**(17). Jt. Assem. Suppl., Abstract H53E-02.

Thorsteinsson, R. and Tozer, E. T. (1971). Geology of the Actic Archipelago. In R. J. W. Douglas, editor, *Geology and economic minerals of Canada*, pages 549–590. Dep. Energy, Mines and Resources, Ottawa, Canada.

Tóth, J. (1962). A theory of ground-water motion in small drainage basins in central Alberta, Canada. *Journal of Geophysical Research*, **67**(11), 4375–4387.

Tóth, J. (1963). A theoretical analysis of groundwater flow in small drainage basins. *Journal of Geophysical Research*, **68**(10), 4795–4812.

van der Kamp, G. and Gale, J. E. (1983). Theory of earth tide and barometric effects in porous formations with compressible grains. *Water Resources Research*, **19**(2), 538–544.

van Weert, F. H. A., van Gijssel, K., Leijnse, A., and Boulton, G. S. (1997). The effects of Pleistocene glaciations on the geohydrological system of Northwest Europe. *Journal of Hydrology*, **195**(1–4), 137–159.

Vidstrand, P. (2003). Surface and subsurface conditions in permafrost areas - a literature review. Technical Report TR-03-06, SKB, Stockholm, Sweden.

Voss, C. I. and Provost, A. M. (2001). Recharge-area nuclear waste repository in southeastern Sweden – Demonstration of hydrogeologic siting concepts and techniques. SKI Report 01:44, Swedish Nuclear Power Inspectorate, Stockholm, Sweden.

Walder, J. S. and Fowler, A. (1994). Channelized subglacial drainage over a deformable bed. *Journal of glaciology*, **40**(134), 3–15.

Wang, H. F. (2000). *Theory of linear poroelasticity with applications to geomechanics and hydrogeology*. Princeton University Press, Princeton, NJ.

Weaver, T. R., Frape, S. K., and Cherry, J. A. (1995). Recent cross-formational fluid flow and mixing in the shallow Michigan Basin. *GSA Bulletin*, **107**(6), 697–707.

Wheeler, J. O., Hoffman, P. F., Cardand, K. D., Davidson, A., Sanford, B. V., Okulitch, A. V., and Roest, W. R. (1997). Geological map of Canada, Map D1860A, Geological Survey of Canada, Ottawa, Canada.

Appendix A

Nomenclature

The print mode for mathematical symbols is applied as follows:

- Scalar variables are in normal italic letters
- Vector variables are in normal bold letters
- Matrix variables are either in capital bold letters or in normal or capital italic letters with the indices i, j

Greek symbols

α	= 1 - K/K_s [-]
α_L	Longitudinal dispersivity [L]
α_T	Transverse dispersivity [L]
$\langle A \rangle$	Mean age [T]
β_f	Fluid compressibility [L T^2 M^{-1}]
β_{pm}	Aquifer compressibility [L T^2 M^{-1}]

δ_{ij} Kroenecker delta, equal to zero when $i \neq j$ and equal to one when $i = j$ [-]

$\delta(t)$ Time-dirac Delta function [T^{-1}]

ϵ General designation of strain [-]

ϵ_{ij} Second-order strain tensor, positive for contraction; $i = j$ indicates contractional/extensional component; $ij = xx, yy$ indicates horizontal strain, $ij = zz$ indicates vertical strain; $i \neq j$ indicates shear component [-]

γ Maximum relative density [-]

Γ_{1st} First order source term [M T^{-1} L^{-3}]

Γ_{-} Inlet boundary [-]

Γ_{+} Outlet boundary [-]

λ $= 2\alpha\left(1-2\nu\right)/3\left(1-\nu\right)$ [-]

Ω Aquifer domain [-]

ϕ Porosity [-]

ρ Fluid density [M L^{-3}]

ρ_0 Reference freshwater density [M L^{-3}]

ρ_b Bulk density [M L^{-3}]

ρ_{ice} Ice relative density [-]

ρ_{max} Maximum density [M L^{-3}]

ρ_r Relative density [-]

ρ_s Matrix density [M L^{-3}]

ρ_w Water density [M L^{-3}]

σ_{ij} Second-order stress tensor, positive for compression; $i = j$ indicates normal stress; $ij = xx, yy$ indicates horizontal stress,

$ij = zz$ indicates vertical stress; $i \neq j$ indicates shear stress [M T^{-2} L^{-1}]

σ'_{ij} Second-order effective stress tensor [M T^{-2} L^{-1}]

σ_{kk} $= \sigma_{xx} + \sigma_{yy} + \sigma_{zz}$ Sum of normal stresses, volumetric stress or octahedral stress [M T^{-2} L^{-1}]

σ'_{kk} $= \sigma'_{xx} + \sigma'_{yy} + \sigma'_{zz}$ [M T^{-2} L^{-1}]

σ_{zz} Vertical stress [M T^{-2} L^{-1}]

τ Tortuosity [-]

μ Viscosity [M L^{-1} T^{-1}]

μ_0 Reference freshwater viscosity [M L^{-1} T^{-1}]

ν Poisson's ratio [-]

ζ One dimensional loading efficiency [-]

Letters

B Three dimensional loading efficiency (Skempton's coefficient) [-]

c Solute concentration [M L^{-3}]

c_{max} Maximum solute concentration [M L^{-3}]

C Courant number [-]

D_{ij} Hydrodynamic dispersion tensor [L^2 T^{-1}]

D^* Diffusion coefficient [L^2 T^{-1}]

g Gravitational acceleration [L T^{-2}]

g_A Age probability density function [T^{-1}]

G Shear modulus of porous medium [M T^{-2} L^{-1}]

h Hydraulic head [L]

h^* Freshwater head [L]

h_{ice} Ice surface elevation [L]

h_s Surface elevation [L]

k_{ij} Permeability tensor [L^2]

J Strength of fluid source [M T^{-1} L^{-3}]

$\mathbf{J}_A$ Total age mass flux vector [L T^{-2}]

m Mass of pore fluid per volume of porous medium [M L^{-3}]

k_0 Permeability to water of liquid-water-saturated soil [L^2]

k_{rw} Relative permeability to water of partially frozen soil [L^2]

K Drained bulk modulus of porous media [M T^{-2} L^{-1}]

K' Drained confined (vertical) bulk modulus of porous media [M T^{-2} L^{-1}]

K_d Distribution coefficient [L^{-3} M]

K_f Bulk modulus of pore fluid [M T^{-2} L^{-1}]

K_{mt} Mass transfer rate [T^{-1}]

K_s Bulk modulus of solids in porous media [M T^{-2} L^{-1}]

K_{ij} Hydraulic conductivity tensor [L T^{-1}]

n Normal outward unit vector [-]

p Pressure [M T^{-2} L^{-1}]

q_i Darcy flux [L T^{-1}]

q_I Fluid source term [T^{-1}]

q_O Fluid sink term [T^{-1}]

P Peclet number [-]

R Retardation factor [-]

S_s One dimensional specific storage [L^{-1}]

S_{s3} Three dimensional specific storage [L^{-1}]

S_w	Fraction of pore volume filled with liquid water [-]
t	Time [T]
T	Temperature [°C]
u, v, w	Distance in x, y, and z directions [L]
u	Groundwater age value [T]
v	Average linear groundwater velocity [L T^{-1}]
V	Volume [L^3]
$\bar{v}$	Magnitude of the groundwater velocity vector [L T^{-1}]
x, y, z	Distance in coordinate direction [L]
$\mathbf{x}$	Vector of Cartesian coordinates (x, y, z) [L]
z	Elevation over a reference level [L]

Differential operators

∂	Partial differential operator
∇	Gradient operator $\left(\nabla f = \frac{\partial f}{\partial x}\mathbf{i} + \frac{\partial f}{\partial y}\mathbf{j} + \frac{\partial f}{\partial z}\mathbf{k}\right)$
$\nabla\cdot$	Divergence operator $\left(\nabla \cdot \mathbf{v} = \frac{\partial v_1}{\partial x} + \frac{\partial v_2}{\partial y} + \frac{\partial v_3}{\partial z}\right)$
∇^2	Laplacian operator $\left(\nabla^2\mathbf{v} = \nabla \cdot \nabla\mathbf{v} = \frac{\partial v_1}{\partial x^2} + \frac{\partial v_2}{\partial y^2} + \frac{\partial v_3}{\partial z^2}\right)$

Appendix B

Map Projection

Conic projections are used for mapping mid-latitude regions, such as Canada and the United States. The result is less overall shape distortion of land and water areas than cylindrical or azimuthal projections. The Albers conic projection is an equal-area projection which displays areas over the entire map so that they retain the same proportional relationship to the areas on the Earth they represent. This projection results in shapes and angles being more distorted than conformal projections but is the only one that is suitable for modelling where mass balance is critical. There is no distortion along the two standard parallels. The Albers equal-area conic projection was first presented by Heinrich Christian Albers in 1805. The parallels are unequally spaced arc of concentric circles, more closely spaced at the north and south edges of the map. The meridians are equally spaced radii of the same circles, intersecting parallels at right angle.

The Albers equal-area conic projection can be constructed with only one standard parallel, but is nearly always used with two, as it display less distortion. The formulas to obtain rectangular coordinates x, y using a sphere as the ellipsoid reference datum, given the radius of the Earth, R, the standard parallels ϕ_1, ϕ_2, the latitude and

longitude for the origin of the rectangular coordinates ϕ_0, λ_0 and the longitude and latitude of the map coordinates, ϕ, λ are [Snyder, 1987]:

$$x = \rho \sin\theta \tag{B.1}$$

$$y = \rho_0 - \rho\cos\theta \tag{B.2}$$

where

$$\rho = R(C - 2n\sin\phi)^{1/2}/n \tag{B.3}$$

$$\rho_0 = R(C - 2n\sin\phi_0)^{1/2}/n \tag{B.4}$$

$$\theta = n(\lambda - \lambda_0) \tag{B.5}$$

$$C = \cos^2\phi_1 + 2n\sin\phi_1 \tag{B.6}$$

$$n = (\sin\phi_1 + \sin\phi_2)/2 \tag{B.7}$$

The Y axis lies along the central meridian λ_0, y increasing northernly. The X axis intersects perpendicularly at ϕ_0, x increasing easterly. For projections in the Northern Hemisphere, n and ρ are positive. If $(\lambda - \lambda_0)$ exceeds the range $\pm 180°$, $360°$ should be added or subtracted to place it within the range.

For the inverse formulas for the sphere, given $R, \phi_1, \phi_2, \phi_0, \lambda_0, x$ and y, the longitude and latitude are given by

$$\phi = \arcsin\left[C - (\rho n/R)^2\right]/(2n) \tag{B.8}$$

$$\lambda = \lambda_0 + \theta/n \tag{B.9}$$

where

$$\rho = [x^2 + (\rho_0 - y)^2]^{1/2} \tag{B.10}$$

$$\rho_0 = R(C - 2n \sin \phi_0)^{1/2}/n \tag{B.11}$$

$$\theta = \arctan[x/(\rho_0 - y)] \tag{B.12}$$

$$C = \cos^2 \phi_1 + 2n \sin \phi_1 \tag{B.13}$$

$$n = (\sin \phi_1 + \sin \phi_2)/2 \tag{B.14}$$

Index